INFORMATION TO USERS

This manuscript has been reproduced from the microfilm master. UMI films the text directly from the original or copy submitted. Thus, some thesis and dissertation copies are in typewriter face, while others may be from any type of computer printer.

The quality of this reproduction is dependent upon the quality of the copy submitted. Broken or indistinct print, colored or poor quality illustrations and photographs, print bleedthrough, substandard margins, and improper alignment can adversely affect reproduction.

In the unlikely event that the author did not send UMI a complete manuscript and there are missing pages, these will be noted. Also, if unauthorized copyright material had to be removed, a note will indicate the deletion.

Oversize materials (e.g., maps, drawings, charts) are reproduced by sectioning the original, beginning at the upper left-hand corner and continuing from left to right in equal sections with small overlaps. Each original is also photographed in one exposure and is included in reduced form at the back of the book.

Photographs included in the original manuscript have been reproduced xerographically in this copy. Higher quality 6" x 9" black and white photographic prints are available for any photographs or illustrations appearing in this copy for an additional charge. Contact UMI directly to order.

U·M·I

University Microfilms International
A Bell & Howell Information Company
300 North Zeeb Road, Ann Arbor, MI 48106-1346 USA
313 761-4700 800 521-0600

Order Number 9306235

On the generation and dispersion of Yanai waves with a spectral Chebyshev-collocation reduced-gravity ocean model

Kelly, Brian Gerard Joseph, Ph.D.

The Florida State University, 1992

U·M·I
300 N. Zeeb Rd.
Ann Arbor, MI 48106

THE FLORIDA STATE UNIVERSITY

COLLEGE OF ARTS AND SCIENCES

ON THE GENERATION AND DISPERSION OF YANAI WAVES
WITH
A SPECTRAL CHEBYSHEV-COLLOCATION
REDUCED-GRAVITY OCEAN MODEL

By

BRIAN GERARD JOSEPH KELLY

A Dissertation submitted to the
Program in Geophysical Fluid Dynamics
in partial fulfillment of the
requirements for the degree of
Doctor of Philosophy

Degree Awarded:

Fall Semester, 1992

The members of the Committee approve the dissertation of Brian Kelly defended on November 4, 1992.

James J. O'Brien

James J. O'Brien
Professor directing Dissertation

Jon Ahlquist

Jon Ahlquist
Outside Committee member

William Dewar
Committee Member

Christopher Hunter
Committee Member

David Kopriva
Committee Member

Dedication

In honour of the Sacred Heart of Jesus, the Immaculate Heart of Mary and in loving memory of my parents, Thaddeus and Philomena.

Acknowledgements

This research was supported by the Office of Naval Research with a Secretary of the Navy grant ONR 1485J1240, by the National Oceanographic and Atmospheric Administration, grant NA 84AA - D - 00049, by the Physical Oceanography Section of the National Science Foundation, grant OCE - 8811316 and by the Ocean Processes Branch of the National Aeronautics and Space Administration, grant NAGW - 985. Additional support has been provided by the Geophysical Fluid Dynamics Institute of the Florida State University, which I greatly appreciate. The Florida State University Computing Center provided CPU time on its Cray YMP supercomputer.

I wish to express my sincere gratitude to my major professor, Dr. James J. O'Brien, for all his advice, support and patience during the course of this work. Thanks to him especially for making it possible for me to come to the United States and to study here at F.S.U.. I thank also Drs. Jon Ahlquist, William Dewar, Christopher Hunter and David Kopriva for their input to this project and for serving on my doctoral committee. This dissertation was typed using the LaTeX document preparation system and I appreciate the assistance of Dr. Ahlquist in providing a set of macros to facilitate the type setting.

I feel very fortunate, for many reasons, to have been a member of the Mesoscale Air-Sea Interaction Group under the leadership of Dr. O'Brien. I appreciate all the technical support provided by Alan Davis and James Stricherz and the secretarial support provided by Ruth Pryor, Rita Kuÿper and Patty Boutelle. I have benefitted from the interaction with all the students of MASIG and in particular from the many fruitful discussions and conversations with Jiayan Yang and Lisan Yu.

This study could not have been completed without the strong spiritual and emotional support provided by numerous friends and family. I especially thank my dear friend Lenora DeCarlo and all the former and present members of Our Lady, Rosa Mystica Prayer Group whose prayers and sacrifices I have benefitted from.

It is with great love that I acknowledge the support of my brother John, my sisters Brigid and Angela, and most especially to my parents Thaddeus and Philomena who have prayed continually for me and on numerous occasions replenished my confidence and who, sadly, departed from this life before this work was completed.

Finally, I thank You, Almighty God, for granting me so many blessings and graces each day of my life which have enabled me to complete this work.

Contents

Dedication iii

Acknowledgements iv

List of Tables viii

List of Figures ix

Abstract xiii

1 Introduction 1
- 1.1 Spectral Methods In Geophysical Modelling 2
  - 1.1.1 Spectral Methods In Ocean Modelling 4
  - 1.1.2 Irregular Domains 5
  - 1.1.3 Boundary Treatments 6
- 1.2 The Present Study 6

2 Overview of Spectral Methods 8
- 2.1 Method Of Weighted Residuals 8
- 2.2 Spectral Accuracy 14
  - 2.2.1 Smooth, Periodic Functions 14
  - 2.2.2 Smooth, Non-Periodic Functions 15
  - 2.2.3 Sturm-Liouville Theory 15
  - 2.2.4 Jacobi Polynomials 18
  - 2.2.5 Chebyshev Polynomials 19
  - 2.2.6 Gauss-Lobatto Integration 22
- 2.3 Differentiation 24

3 The Model 27
- 3.1 Model Equations 28
- 3.2 Numerical Formulation 30
- 3.3 Boundary Conditions 31

3.4 Numerical Grid Generation 37
    3.4.1 Two-Dimensional Coordinate Transformation 38
    3.4.2 Mapping Procedure 40
3.5 Time Differencing Scheme 43

4 Previous Studies on Yanai Waves 46
4.1 Introduction 46
4.2 Historical Background 47
    4.2.1 Observations 47
    4.2.2 Numerical Experiments 54

5 On A Generating Mechanism for Yanai Waves 58
5.1 Linear Equatorial Free Waves 59
5.2 Choice of Model Parameters 64
5.3 Numerical Experiments 71
5.4 Fourier Analysis 94
5.5 Wavelet Analysis 98

6 Summary and Conclusions 103

Bibliography 106

Vita 115

List of Tables

1 List of various model parameters used in the model. These are the values used in all of the experiments performed unless otherwise specified. 66

List of Figures

1 The first five Chebyshev polynomials on the interval $-1 \leq x \leq 1$. 21
2 Schema for a 1-1/2 layer "reduced-gravity" model. 29
3 The western portion of the physical domain showing the bicharacteristics, directed perpendicularly towards the boundary from the interior region, used to compute the height field at boundary points: (a) At a point on the western boundary one bicharacteristic is used with angle θ measured in the sense shown. (b) At the northwest corner the two bicharacteristics normal to the northern boundary (θ_N) and western boundary (θ_W) are used. 36
4 The mapping function $\underline{x}$ maps the square computational domain into the irregular physical domain bounded by four specifiable curves: Γ_1, Γ_2, Γ_3, and Γ_4. 39
5 (a) Physical domain showing a section of the Indian ocean from 10°S to 25°N, excluding the Gulf of Aden. (b) The square computational domain illustrating a Gauss-Lobatto grid. 42
6 Dispersion diagram for linear equatorial free waves. 63
7 The non-dimensional u, v and ϕ latitudinal profiles for the Yanai wave. Each unit of length on the horizontal axis is equivalent to 1 Rossby deformation radius. 65
8 Dispersion curves for Yanai and Rossby waves.The horizontal lines indicate the locations of periods for 10, 20, 26, 30 and 40 days. 67
9 (a): The dispersion curve for the Yanai waves with wavelength plotted vs. the period in days. The 25-day period wave has a wavelength of 945 km approximately. (b): The group velocity as a function of the period for Yanai waves. Note that the group velocity doubles (from 25 to 50 $cm\,s^{-1}$ approximately) when the period changes from 30 to 20 days. 69
10 (a): Contours of the v field for the 26-day period Yanai wave over the same domain size as used in the numerical experiments. (Contours are non-dimensional and dashed contours indicate negative values). (b): As in (a), but for the u and h fields. 70
11 The wind stress profile used in subsequent numerical experiments. Here the "x'– direction" refers to the direction normal to the western boundary and y' is along this boundary. ($\rho = 1000\ kg\,m^{-3}$) 73

12 The damping function used to absorb the waves approaching the eastern boundary. Effectively there is an open boundary on this side of the domain. 74

13 Spectral model simulation on the Indian Ocean domain from 10°S to 10°N. The wind stress is everywhere parallel to the coast extending a distance of 1000 km from it and switched on immediately at $t = 0$. The figure shows three snap-shots of the meridional velocity field at days 20, 48 and 76. A packet of Yanai waves is generated propagating energy eastwards from the western boundary. Note the increase in wavelength from west to east. . . . 76

14 Indian Ocean model simulation using the monthly climatological winds of Hellerman and Rosenstein (from Kindle and Thompson (1989)). The figure is a sequence of snap-shots of meridional velocity contours for days 230, 258 and 286 of the 8^{th} year of integration, showing a packet of Yanai waves propagating from the west. A similar increase in wavelength occurs in going from west to east, as in our model solution. 77

15 (a): The height field anomaly after 299 days with a purely meridional wind patch oscillating with period 10 days at the western boundary. The wind patch size is 1000 km and the theoretical wavelength is $37,688$ km. The wave is too long for the domain and is absorbed by the sponge layer. (Contours are in metres, with solid contours indicating positive values and dashed contours indicating negative values). (b): As in (a) except that the forcing period is 13 days. The theoretical wavelength is $3,505$ km and the simulation is in good agreement with this. 80

16 (a):A synthetic wave packet of Yanai waves generated by superposing 20 frequencies of the (non-dimensional) analytical height solution. Each individual wave is enveloped by a Gaussian amplitude function with a standard deviation equal to $\frac{1}{8}^{th}$ of the wavelength and moving with the group velocity of that wave. (Contours are non-dimensional). (b): Model solution on a rectangular domain after 100 days. The wind patch size is 1000 km. ($\tau_x \equiv 0$). Note the similarity in wavelength selection with (a). (Contours are in metres). 82

17 (a): Analytical wave packet as in the previous figure. (b): The anti-symmetric component of the model height field anomaly after 100 days. The physical domain has a sloping western boundary at 45°. The wind stress is directed northwards everywhere parallel to the coast and has a patch size of 1000 km. Note the similarity in wavelengths present with those in (a) (and hence with those of the model solution on the rectangular domain) indicating that the sloping boundary has no effect on this selection. (Contours are in metres). . 85

18 (a): Model solution of the standard test experiment after 100 days as in the previous figure. (b): As in (a) except that the wind patch size has been increased to 2000 km. No appreciable change in the wavelengths selected is noticed as can be seen in the similarity of the wave pattern of (a). (Contours are in metres). 86

19 (a): Height field anomaly after 100 days with a wind patch size of 1000 km as in figure (16b). (b): Same as in (a) except that the wind patch size has been reduced below the Rossby deformation radius to 280 km. Although the waves are weaker and more distorted than in (a), the wavelength selection has not been affected except that more of the short waves are visible near the forcing region. Inertia-gravity waves appear near the boundaries which interfere with the longer wavelengths because of their small amplitudes, causing them to be distorted. (Contours are in metres). 87

20 (a): Model v field on a rectangular domain after 50 days. The wind stress is parallel to the western boundary with a patch size of 1000 km. (Contours are in $m\,s^{-1}$). (b): As in (a) except that the western boundary is sloping at 30°to the eastern direction. The wind stress is everywhere parallel to the coast. Note the distortion of the long waves in this case caused by the boundary slope. 89

21 (a): Anti-symmetric height field anomaly of the standard test experiment as in figure (18a). (Contours are in $m\,s^{-1}$). (b): As in (a) except that the slope of the western boundary has been increased to 60°. The wavelengths excited are virtually identical in both cases. The longest wave group has been absorbed by the sponge layer more in (a) because of the shorter distance between the forcing region and the eastern boundary (due to the shallower slope of the western boundary). 90

22 (a): Anti-symmetric height field anomaly of the standard test experiment as in figure (18a). (Contours are in $m\,s^{-1}$). (b): Same as (a) except that the slope of the western boundary has been decreased to 30°. Again the wavelengths selected are the same apart from the increased distortion and the greater absorption of the leading wave group by the sponge layer. . . . 91

23 (a):Contours of the model height field anomaly after 100 days. The (meridional) wind forcing is adjacent to the western boundary and has a patch size of 1000 km. (Contours are in metres). (b): As in (a) except that the wind has been shifted eastwards to a distance 4000 km from the western boundary. The leading wave group has been almost completely damped by the sponge layer but nevertheless the remaining wavelengths are similar to (a). There is an anti-symmetric Rossby wave packet emanating from the eastern side of the forcing region propagating westwards. 93

24 (a): The de-meaned time series of the height field anomaly located at a position 5,201 km from the western boundary, 167 km north of the equator. The model run is the same as that of figure (16b). The record is at every $\frac{1}{2}$ day for 300 days. Note the appearance of the 25-day waves after the initial burst of high frequency oscillations. (b): The power spectrum of the time series in (a) taken from days 150 to 300, showing a high peak centred on 25 days. 95

25 (a): The de-meaned time series of the height field anomaly from the same model run as in figure (18a). The wind stress is parallel to the western boundary sloping at 45°. Since $\tau_x \neq 0$ there are Kelvin waves present in addition to the Yanai waves. The 25-day waves appear again after about 150 days when the Kelvin wave peak and high frequency Yanai waves have passed. (b): The power spectrum of the time series in (a) taken from days 150 to 300 showing a high peak centred on 25 days. 96

26 (a): *Top*: A west-east section of the anti-symmetric component of the height field anomaly (from the standard test experiment) at 177 *km* north of the equator after 20 days. (Values are in metres). *Bottom*: The wavelet transform of the profile above. Note the appearance of the "tongue" on the top-left corner of the plot, which corresponds to high contour values. (The contour values can be considered as an "energy" but are not labeled since they do not have a quantitative measure). (b): As in (a) after 60 days. Note the growth of the "tongue". 100

27 (a): The anti-symmetric height field and wavelet transform after 100 days. (b): As in (a) at time 140 days. The "tongue" is starting to narrow and rise after having extended almost to the bottom-left part of the domain. This is an indication of the waves beginning to select a narrow wavelength range. . 101

28 (a): The anti-symmetric height field and wavelet transform after 160 days. (b): As in (a) after 200 days. The "tongue" has continued to narrow and become more horizontal with a central wavelength around 945 *km*, which corresponds to a period of 25 days. 102

Abstract

A spectral Chebyshev-collocation method is devised for the 1-1/2 layer nonlinear reduced-gravity equations. Following a general description of spectral methods with their application to meteorological and oceanographic problems the implementation of the numerical technique is described. A bicharacteristic scheme is applied to solve the equations at the boundaries incorporating the boundary conditions. This treatment enables stable time integrations (spectral methods in general are very sensitive to boundary errors). A simple transfinite grid generation method is used to construct grids over irregular (non-rectangular) simply-connected domains.

The model is used in a study of the dynamics of Yanai (or mixed Rossby-gravity) wave packets. These are of interest because of the observations of equatorial instability waves (which have the characteristics of Yanai waves) and their role in the momentum and heat budgets in the tropics. A series of experiments is performed to investigate the generation of the waves by simple cross-equatorial wind stress forcings in various configurations and the influence of a western boundary on them. They may be generated in the interior ocean as well as from a western boundary. The observations from all the oceans indicate that the

waves have a preferential period and wavelength of around 26 days and 1000 km respectively. This is seen in the model results too and a plausible explanation is provided as being due to the dispersive properties of Yanai waves.

Chapter 1

Introduction

Since the beginning of research in numerical modelling of geophysical flows, finite difference techniques have been widely used and continue to be developed. With the advent of high-speed digital computers, scientists and mathematicians have collaborated in earnest, seeking accurate and efficient ways to compute numerically the flow fields for the atmosphere and the oceans. For the nonlinear shallow water equations, Arakawa (1966) [1] devised a numerical technique which preserves three constraints (namely, the conservation of energy, enstrophy, and mean vorticity) of the governing differential equations, in finite difference form. This is an elegant approach for dealing with the nonlinear instability or aliasing error. Arakawa showed that it is possible to construct schemes that are not only free of the nonlinear computational instability, but also free of the spurious inflow of energy to the short waves which cause this instability, instead of artificially suppressing their amplitudes. Grammeltvedt (1969) [19] gives a survey of finite difference schemes, some of which are still being used in meteorology and oceanography today.

There are, of course, other popular numerical techniques to solve partial differential equations. Spectral methods belong to one such class of techniques, and although they are not so widely used as finite difference methods in oceanography, they do provide a very powerful tool for solving certain types of problems. Finite difference methods are "local" methods, in the sense that the computed solution at a grid point depends only on the local spatial solution at the current and a few recent time levels. They may suffer from poor phase speed representations of the waves being modelled. Spectral techniques, on the other hand, are "global" methods and can generally give improved phase speeds.

1.1 Spectral Methods In Geophysical Modelling

A spectral method was introduced into meteorological modelling by Silberman (1954) [53] using the non-divergent barotropic vorticity equation. In spherical geometry, he expanded the solution as a sum of surface spherical harmonics using Legendre polynomials. Other authors followed suit with this method, including Platzman (1960) [50], Baer and Platzman (1961) [2]. As pointed out by Platzman (1960) [50], one of the principal advantages of this spectral technique over finite difference schemes is that it prevents nonlinear computational instability, because there is no spurious energy cascade to the shorter wavelengths. However, such a model was not considered to be competitive with other methods at high resolution. The scheme is inefficient due to the large number of computations per time step needed for the nonlinear terms in the equations. The number of these computations grew as $O(N^2)$ (in the one-dimensional case), where N is the number of harmonics retained. Most finite difference methods require O(N) computations (N here being the number of grid points).

Eliasen *et al.* (1970) [13] and Orszag (1970) [44], working independently, introduced the so-called "transform method", which brought about a renewal of interest in spectral methods for meteorological modelling. The concept is to carry out multiplications involving nonlinear terms in physical space and transform back to spectral space again for the linear dynamics. This reduces the operation count from O(N^2) to O($N\log_2(N)$) making the spectral method competitive in efficiency with standard finite difference techniques at high resolution. Naturally, the success of this scheme was dependent upon the already available fast transform methods, such as, for example, the Fast Fourier Transform (Cooley and Tukey, (1965) [10]) in the case where trigonometric functions are used as basis functions. With an increase in resolution without much of a loss in efficiency, another important aspect of the spectral method came into play, namely its rate of convergence. This is often referred to as "spectral accuracy". It means that the truncation error decays faster than any polynomial in ($1/N$), where N is the number of basis functions used in the truncated series expansion for the solution. Finite difference methods have an algebraic rate of convergence, so that, for example, a second order accurate scheme has an error which decays as O($1/N^2$), N being the number of grid points used. In other words, for a given accuracy, the spectral method requires much fewer basis functions than grid points needed for the finite difference scheme. Thus, at high resolution, there is a substantial saving in computer storage space with the former. For problems in meteorology and oceanography, this can be a very significant advantage.

1.1.1 Spectral Methods In Ocean Modelling

Bretherton and Karweit (1975) [4] introduced a 6-layer quasi-geostrophic model for mid-ocean mesoscale modelling over a limited area domain. They assumed that the non-divergent part of the velocity field was doubly periodic and used a Fourier spectral method to solve the Poisson equation resulting at each time step. Such a model has become popular with ocean modellers for the study of the dynamical properties of the mesoscale eddy field under simulated mid-ocean conditions. Rhines (1975) [52] used this method , as did Haidvogel and Held (1980) [22] and Haidvogel (1983) [21].

It is also possible to attain "spectral accuracy" with a model where the domain is not doubly periodic. If the physical domain has solid wall boundaries, for example, then either Chebyshev or Legendre polynomials may be chosen as basis functions to yield this accuracy. A further discussion on this topic will be given later. For limited area modelling in oceanography several authors have described spectral models using Chebyshev polynomials (*e.g.* Haidvogel *et al.* (1980) [23], Jensen and Kopriva (1988) [29]). Fulton and Schubert (1987b) [15] described different limited area, nonlinear shallow water models with Chebyshev basis functions. They have implemented models with both open and solid wall boundary conditions. Mixed basis functions can also be used, *e.g.* with channel models. In a study of the circulation driven by oscillatory winds, Haidvogel and Rhines (1983) [20] used a Chebyshev and a sine series expansion. As a general rule (see Boyd (1989, p. 2) [3]) it is best to use Chebyshev polynomials for spatial dimensions which are not periodic, and to use Fourier series for spatial dimensions which are periodic.

1.1.2 Irregular Domains

One of the major difficulties in using a spectral method is that the computational domain must be a square. If the physical domain (e.g. an ocean basin) has irregular boundaries, then a mapping must be employed to transform the physical domain into a square. There are many problems associated with such mappings. If the domain is not simply connected (as in the case of an ocean basin with islands), then several different mappings may have to be used, one for each simply connected segment of the domain. All these parts have to be "patched" together in some manner, allowing a two-way interaction between each pair of neighbouring segments. There may still be problems associated with the mappings even if the physical domain is simply connected. The boundary could be so irregular that the grid generated after the mapping is not one-to-one (*i.e.* grid lines are intersecting). If this occurs, domain "patching" may still have to be used. Some domain mapping techniques have been used by ocean modellers, although typically in rather simplified situations. In a study of flow over irregular coastal topography, Broutman and Grimshaw (1989) [5] used a simple conformal mapping to transform the square computational domain into more interesting shapes. Haidvogel *et al.* (1991) [24] have designed a semi-spectral primitive equation ocean model with Chebyshev polynomials for the vertical discretization and finite differences in the horizontal. Using a coordinate transformation to generate an orthogonal curvilinear horizontal grid, their model can allow for "moderately" irregular basin geometries. An illustration of domain decomposition methods used in the spectral solution of hyperbolic equations is given by Kopriva (1989) [33]. He showed using as examples some simple equations in both one and two space dimensions that spectral accuracy can be obtained by using "patched" (*i.e.* where two subdomains intersect along an interface) and "overset" (*i.e.* where subdomains overlap) Chebyshev grids.

1.1.3 Boundary Treatments

When employing a spectral method for solving hyperbolic equations, care must be taken to treat the boundary conditions correctly. As pointed out by Gottlieb and Orszag (1977, p. 155) [17], the mathematical features of spectral methods follow very closely the differential equations being solved. Just as it is important that the analytical solution gives the correct characteristics at the boundaries, so also is it necessary that some attempt be made to compute these characteristics numerically. In this regard, spectral methods are much more sensitive to errors at the boundaries than are finite difference methods in general. Nevertheless, they are free of problems encountered with finite differences when higher order methods are used. They do not require extra "ghost" points outside of the computational domain, nor do they require extra "boundary conditions" (ones other than those of the differential equations), which occurs with finite difference methods of higher order than the governing differential equations.

1.2 The Present Study

The purpose of this investigation is twofold: 1) To design and implement a Chebyshev-collocation ocean model using the 1-1/2 layer, nonlinear reduced-gravity equations on an irregular domain; 2) To apply the model in an investigation of the dynamical properties of equatorial Yanai (or mixed Rossby-gravity) waves.

Jensen and Kopriva (1988) [29] examined a similar spectral model, using the linear reduced-gravity equations on a rectangular domain. Their results show that, for the same accuracy, the spectral method requires only 15% of the storage needed by a standard finite difference model, while the computer time differs by less than 20%. This is a striking illustration of a point made by Canuto *et al.* (1988, p. 7) [7] that "in most practical applications the benefit of the spectral method is not the extraordinary accuracy available for large N (number of modes), but rather the small size of N necessary for a moderately accurate solution". We use an algebraic grid generating method to construct grids over irregular shaped domains, and a bicharacteristic scheme to compute all the boundary values.

In this study we illustrate the power of the spectral method in solving many types of oceanographic modelling problems. The specific problem we study here is on certain dynamical properties of equatorial Yanai wave packets. These instability waves have occupied the interest of oceanographers for almost the past twenty years due to their role in the momentum and heat balance in the equatorial regions and most especially because of the curious way in which these waves always seem to select a preferential wavelength and period of around 1000 km and 25 days. We illustrate how the waves can be generated by simple cross-equatorial wind stress forcings and present a plausible explanation as to why this particular wavelength and period appears.

Chapter 2

Overview of Spectral Methods

In this chapter, we give a brief introduction to spectral methods. We concentrate on the Chebyshev-collocation method.

We present the mathematical framework for the numerical formulation of spectral models. Spectral schemes belong to a class of numerical techniques known as the "method of weighted residuals". It is from this point of view that we present the mathematical framework .

2.1 Method Of Weighted Residuals

Let us consider the following representation for a model problem:

$$\mathcal{L}[u] = 0 \tag{1}$$

together with, as yet unspecified, boundary and initial conditions. The symbol, $\mathcal{L}$, is a differential operator, which may be linear or nonlinear. The solution, $u = u(\underline{x}, t)$, we may think of either as a vector or as a scalar function, with $\underline{x}$ being a position vector. We approximate the solution u as:

$$u \approx u^N(\underline{x}, t) = \sum_{k=0}^{N} a_k(t)\phi_k(\underline{x}) \tag{2}$$

where $\phi_k(\underline{x})$ are specifically chosen 'basis' or 'trial' functions, and $a_k(t)$ are coefficients we must compute. We define the residual function, $r^N(\underline{x}, t)$ according to:

$$\mathcal{L}[u^N] = r^N \tag{3}$$

In general $r^N(\underline{x}, t) \not\equiv 0$. We introduce a new set of functions, $\{\psi_k(\underline{x}, t)\}_{k=0}^{\infty}$ called 'weight' or 'test' functions. The fundamental idea behind the method of weighted residuals is that the residual function, r^N, is required to be orthogonal to the space spanned by the finite set of test functions $Y^N = \{\psi_k\}_{k=0}^{N}$. Thus we choose the coefficients $a_k(t)$ so that $r^N \perp Y^N$, and therefore, by the Projection Theorem (Stakgold, (1979 p. 266) [56]) the "best approximation" to r^N from Y^N is the zero vector. It is in this sense that the residual function is brought as close to zero as possible.

To be more precise, we regard the solution $u \in \mathcal{H}$, where $\mathcal{H}$ is a Hilbert space. The set $\{\phi_k\}_{k=0}^{\infty}$ forms a basis for $\mathcal{H}$, and so the finite dimensional space, X^N, defined by the span of the set of functions $\{\phi_k\}_{k=0}^{N}$ is a subspace of $\mathcal{H}$. Let $< \cdot, \cdot >$ denote the inner product for $\mathcal{H}$. The requirement that r^N be orthogonal to Y^N implies:

$$< r^N, v >= 0 \qquad \forall \; v \in Y^N \tag{4}$$

This gives us a set of conditions to compute the coefficients $a_k(t)$. We shall illustrate the above by means of some simple examples.

EXAMPLE 1: Consider the one-dimensional nonlinear advection equation:

$$\frac{\partial u}{\partial t} + u\frac{\partial u}{\partial x} = 0, \qquad x \in (0, 2\pi) \tag{5}$$

with initial condition: $u(x, 0) = u_0(x)$

and periodic boundary condition: $u(0, t) = u(2\pi, t)$.

We select as our space of trial functions the space of all trigonometric polynomials, and for our subspace X^N the set $\{e^{ikx}\}_{k=-N/2}^{k=N/2-1}$. Thus we have:

$$u^N(x, t) = \sum_{k=-N/2}^{N/2-1} \hat{u}_k(t)e^{ikx} \tag{6}$$

where the coefficients $\hat{u}_k(t)$ are to be determined by an orthogonality condition similar to (4) above. We select as the test functions the space of trigonometric polynomials also, so that $X^N = Y^N = \{e^{ikx}\}_{k=-N/2}^{k=N/2-1}$. Using the usual inner product for this Hilbert space , i.e.

$$< u, v >= \int_0^{2\pi} u(x)\bar{v}(x)dx \tag{7}$$

(where $\bar{v}(x)$ is the complex conjugate of $v(x)$) we obtain from equation (4):

$$< r^N, e^{ikx} >= \int_0^{2\pi} (\frac{\partial u^N}{\partial t} + u^N\frac{\partial u^N}{\partial x})e^{-ikx}dx = 0 \qquad k = -N/2, \ldots, N/2 - 1 \tag{8}$$

Substituting the expression for u^N given by (6) into (8) and using the orthogonality properties of trigonometric polynomials yields:

$$\frac{\partial \hat{u}_k}{\partial t} + (\widehat{u^N\frac{\partial u^N}{\partial x}})_k = 0 \qquad k = -N/2, \ldots, N/2 - 1 \tag{9}$$

where

$$(\widehat{u^N\frac{\partial u^N}{\partial x}})_k = \frac{1}{2\pi}\int_0^{2\pi} u^N\frac{\partial u^N}{\partial x}e^{-ikx}dx \tag{10}$$

Equations (9) are a system of ODEs, which can be discretized in time, and then solved for the unknown coefficients $\hat{u}_k$. The nonlinear term in equation (10) is of the form:

$$(\widehat{u^N w^N})_k = \frac{1}{2\pi}\int_0^{2\pi} u^N w^N e^{-ikx}dx \tag{11}$$

where u^N,w^N have expansions similar to equation (6) above. When u^N,w^N are expanded in this form, again using the orthogonality properties of the trigonometric polynomials, we obtain:

$$(\widehat{uw})_k = \sum_{p+q=k} \hat{u}_p \hat{w}_q \tag{12}$$

This is a convolution, and requires $O(N^2)$ operations. Eliasen *et al.* (1970) [13] and Orszag (1970) [44], using the "Transform Method", showed that it is more efficient to perform the multiplication $u\frac{\partial u}{\partial x}$ in physical space, rather than compute a convolution sum in spectral space, thereby reducing the operation count to $O(N \log_2 N)$. (See Canuto *et al.*, (1988) [7].) □

The choice of test functions determines the type of spectral method. There are three basic types:

- *The Galerkin Method*: The set of test functions is identical to the set of trial functions. *i.e.*, $\psi_k = \phi_k \quad \forall k$.
- *The Collocation Method*: The set of test functions consists of Dirac delta functions. *i.e.* $\psi_k = \delta(x - x_k)$, where the set $\{x_k\}_{k=0}^N$ are the "collocation points".

- *The Tau Method*: The set of test functions are given by:

$$\psi_k = \begin{cases} \phi_k & k = 0, 1, \ldots, N-l \\ \chi_k & k = N-l+1, \ldots, N \end{cases}$$

where the ϕ_k do not satisfy any boundary condition and the χ_k are determined so that the solution u^N satisfies l boundary conditions.

Our example 1 above is an illustration of the Fourier-Galerkin method, because we chose Fourier trial functions. This is the spectral scheme most often used in oceanographic problems. We note here also that the trial functions with the Galerkin method must already satisfy the boundary conditions. For a comparison of these three methods applied to geophysical flow situations, see Fulton and Schubert (1987a, 1987b) [14], [15].

For our ocean model we choose to use the Chebyshev-collocation scheme. We illustrate this method by means of a simple example using Burger's equation.

EXAMPLE 2: The governing equation, boundary and initial conditions are:

$$\frac{\partial u}{\partial t} + u\frac{\partial u}{\partial x} - \nu\frac{\partial^2 u}{\partial x^2} = 0, \quad x \in (-1, 1) \tag{13}$$

$$u(-1, t) = u(1, t) = 0 \tag{14}$$

$$u(x, 0) = u_0(x) \tag{15}$$

We choose our trial functions as Chebyshev polynomials:

$$\phi_k(x) = T_k(x) = \cos(k\cos^{-1}(x)), \quad k = 0, 1, \ldots, N \tag{16}$$

and our test functions as delta functions:

$$\psi_k(x) = \delta(x - x_k), \quad k = 0, 1, \ldots, N \tag{17}$$

We will discuss later on how to select the collocation points, but for now we just say that $x_0 = -1$ and $x_N = 1$. Our approximate solution is, therefore,

$$u^N(x,t) = \sum_{k=0}^{N} \hat{u}_k(t)T_k(x) \tag{18}$$

Employing the orthogonality condition given by equation (4), and using the usual inner product for square-integrable functions on the interval $-1 \leq x \leq 1$:

$$< u, v >= \int_{-1}^{1} u(x)v(x)dx \tag{19}$$

we obtain:

$$0 =< r^N, \psi_k >= \int_{-1}^{1} (\frac{\partial u^N}{\partial t} + u^N \frac{\partial u^N}{\partial x} - \nu \frac{\partial^2 u}{\partial x^2})\delta(x - x_k)dx$$

$$\Rightarrow \frac{\partial u^N}{\partial t} + u^N \frac{\partial u^N}{\partial x} - \nu \frac{\partial^2 u^N}{\partial x^2}\Bigg|_{x=x_k} = 0 \quad k = 0, 1, \ldots, N \tag{20}$$

The approximate solution satisfies the differential equation at the collocation points. The derivatives can be computed by differentiating equation (18), but the details will be described later when we discuss the selection of the collocation points. Once the derivatives are evaluated, then equation (20) can be solved for $u^N(x,t)$, using a suitable time discretization scheme. For this we use a fourth-order Runge-Kutta method. (see Canuto *et al.*, (1988) [7]). Note that with the collocation method, the equations are solved in *physical* space, whereas with the Galerkin (and also the Tau) method, they are solved in *transform* space. The boundary conditions in equation (14) can be applied at each time step: $u^N(-1,t) = u^N(1,t) = 0 \quad \square$

2.2 Spectral Accuracy

We illustrate the meaning of the term *spectral accuracy*, both for periodic and non-periodic functions. It is in seeking this degree of accuracy that helps to determine which set of functions one should use as trial functions for a given model problem.

2.2.1 Smooth, Periodic Functions

Recall from equation (6) that the Fourier-Galerkin approximation to the solution of the model problem (1) is given by:

$$u^N = \sum_{k=-N/2}^{N/2-1} \hat{u}_k e^{ikx} \tag{21}$$

For the continuous transform:

$$\hat{u}_k = \frac{1}{2\pi}\int_0^{2\pi} ue^{-ikx}dx = \frac{1}{2\pi}\int_0^{2\pi} \frac{\partial u}{\partial x}\frac{e^{-ikx}}{(-ik)}dx + \left.\frac{ue^{-ikx}}{-ik}\right|_0^{2\pi} \tag{22}$$

If u is periodic, then the boundary term in this last equation vanishes, and $\hat{u}_k \sim O(\frac{1}{k})$. Similarly, if u and its first m derivatives are smooth and periodic, then as a result of repeated integration by parts, we have:

$$\hat{u}_k \sim O(\frac{1}{k^m}) \tag{23}$$

Therefore, if u is infinitely smooth, and all its derivatives are periodic too, then $\hat{u}_k$ decays faster than any inverse power of k. This is a significant result in the light of the following:

$$< u - u^N, u - u^N >= \|u - u^N\|^2$$

(where $\|u\|$ is the *norm* of the function u)

$$= \| \sum_{k=-\infty}^{\infty} \hat{u}_k e^{ikx} - \sum_{k=-N/2}^{N/2-1} \hat{u}_k e^{ikx}\|^2 = \| \sum_{|k|\geq N/2} \hat{u}_k e^{ikx}\|^2$$

where we have used the notation:

$$\sum_{|k|\geq N/2} = \sum_{k<-N/2} + \sum_{k\geq N/2} .$$

On applying Parseval's identity to this last expression, we obtain:

$$\|u - u^N\|^2 = 2\pi \sum_{|k|\geq N/2} |\hat{u}_k|^2 \tag{24}$$

Thus, the norm of the truncation error is governed by how rapidly the coefficient $|\hat{u}_k|$ decays. Owing to the fact that $\hat{u}_k$ decays faster than any inverse power of k, the Fourier approximation has a high rate of convergence for this class of functions. This is referred to as *spectral accuracy*.

2.2.2 Smooth, Non-Periodic Functions

It is also possible to obtain spectral accuracy for functions which are smooth but not periodic. This case is more relevant from an oceanographic point of view, for limited-area models with either solid wall or open boundaries. It is not true that any set of orthogonal functions will produce this degree of accuracy to a smooth solution. The trial functions must be chosen correctly. We illustrate how the eigenfunctions of a *singular* Sturm-Liouville operator allow spectral accuracy for any smooth function with no restriction on the boundary conditions to be applied.

2.2.3 Sturm-Liouville Theory

The general Sturm-Liouville problem is written as:

$$\mathcal{L}[u] = -(pu')' + qu = \lambda wu, \quad x \in (-1,1) \tag{25}$$

together with some suitable boundary condition for $u(x)$. The prime $'$ denotes differentiation: $u' = \frac{du}{dx}$. We concern ourselves with *singular* Sturm-Liouville problems, and require:

$$p(x) > 0 \quad \in C^1(-1,1)$$

(*i.e.* $p(x)$ is continuously differentiable on the open interval $(-1,1)$)

$$q(x) \geq 0 \quad \in C^0(-1,1)$$

(*i.e.* $q(x)$ is continuous on the open interval $(-1,1)$)

$$w(x) \geq 0 \quad \in C^0(-1,1)$$

and is integrable over $(-1,1)$. A singular Sturm-Liouville problem occurs when $p(x) = 0$ on at least one of the boundary points. Let $L^2_w(-1,1)$ denote the Hilbert space of all square-integrable functions with respect to the weight function $w(x)$ on the interval $-1 \leq x \leq 1$. *i.e.*,

$$\int_{-1}^{1} u^2 w(x) dx < \infty \quad \forall \; u \in L^2_w(-1,1).$$

with inner product:

$$< u, v >= \int_{-1}^{1} u(x)v(x)w(x)dx$$

and norm:

$$\|u\|^2_w =< u, u > .$$

The eigenfunctions of the differential operator $\frac{\mathcal{L}}{w}$ form an orthogonal basis for this Hilbert space. Let us denote these eigenfunctions by the set $\{\phi_k\}_{k=0}^{\infty}$ and assume that they have already been normalized. If we expand the function u of our model problem in terms of these eigenfunctions, we obtain:

$$u = \sum_{k=0}^{\infty} \hat{u}_k \phi_k \tag{26}$$

where $\hat{u}_k = < u, \phi_k >$, since ϕ_k is an orthonormal basis. The only requirement we place on u is that it be infinitely differentiable. Since the ϕ_k are eigenfunctions of $\frac{\mathcal{L}}{w}$ we have:

$$\mathcal{L}[\phi_k] = \lambda_k w \phi_k \tag{27}$$

where λ_k is the k^{th} eigenvalue corresponding to ϕ_k.

$$\begin{aligned}
\Rightarrow \hat{u}_k &= \int_{-1}^{1} uw\phi_k dx \\
&= \frac{1}{\lambda_k} \int_{-1}^{1} u\mathcal{L}[\phi_k] dx \\
&= \frac{1}{\lambda_k} \int_{-1}^{1} u(-(p\phi_k')' + q\phi_k) dx \\
&= \frac{1}{\lambda_k} \left\{ \Big[-up\phi_k \Big]_{-1}^{1} + \int_{-1}^{1} (p\phi_k' u' + uq\phi_k) dx \right\} \\
&= \frac{1}{\lambda_k} \left\{ \Big[-up\phi_k' \Big]_{-1}^{1} + \int_{-1}^{1} \phi_k((-pu')' + qu) dx + \Big[pu'\phi_k \Big]_{-1}^{1} \right\} \\
&= \frac{1}{\lambda_k} \left\{ < \phi_k, \frac{\mathcal{L}[u]}{w} > + \Big[p(u'\phi_k - u\phi_k') \Big]_{-1}^{1} \right\}
\end{aligned}$$

We impose the boundary condition on $p(x)$: $p(-1) = p(1) = 0$, yielding:

$$\hat{u}_k = \frac{1}{\lambda_k} < \phi_k, \frac{\mathcal{L}[u]}{w} > \tag{28}$$

If, now, $u_{(1)} = \frac{\mathcal{L}}{w} \in L^2_w$, we can repeat the integration by parts. At the m^{th} stage, we obtain:

$$\hat{u}_k = \frac{1}{\lambda_k^m} < \phi_k, u_{(m)} > \tag{29}$$

where

$$u_{(m)} = \frac{\mathcal{L}[u_{(m-1)}]}{w} \quad \in \quad L^2_w(-1,1). \tag{30}$$

In our case, (using Chebyshev polynomials) and indeed for most cases of interest, $\lambda_k = O(k^2)$ (see Canuto *et al.* (1988, p. 285) [7]). Equation (29) therefore implies that:

$$|\hat{u}_k| \leq \frac{C}{k^{2m}} \|u_{(m)}\|_w \tag{31}$$

for some constant C. Compare this bound with the decay rate in the Fourier case given by equation (23). If u is infinitely differentiable, the coefficients $\hat{u}_k$ decay faster than algebraically, and spectral accuracy is obtained as in the Fourier case with periodic functions. Note, again, that we have not imposed specific boundary conditions on u to get this result.

2.2.4 Jacobi Polynomials

When deciding upon which functions to use as trial functions for a spectral method, *polynomials* are of particular interest because of the ease in which they can be evaluated, and their derivatives computed. It can be shown (Canuto *et al.*, (1988, p. 286) [7]) that the only polynomial solutions to the singular Sturm-Liouville problems just discussed are the Jacobi polynomials, where:

$$p(x) = c_1(1-x)^{\alpha+1}(1+x)^{\beta+1} \tag{32}$$

$$w(x) = c_2(1-x)^{\alpha}(1+x)^{\beta} \tag{33}$$

with $-\frac{1}{2} \leq \alpha, \beta \leq \frac{1}{2}$, $c1$, $c2$ constants. The two common sets of polynomials chosen are the Legendre polynomials ($\alpha = \beta = 0$) and the Chebyshev polynomials ($\alpha = \beta = \frac{1}{2}$). Fulton and Schubert (1987a) [14] indicate three important reasons why a Chebyshev series approximation is preferred for limited-area modelling:

- Chebyshev series give better global approximations than do Legendre series for the same number of terms.
- Chebyshev series converge faster than Legendre series for approximations to non-smooth functions.
- Chebyshev series can be evaluated very efficiently using the Fast Fourier Transform algorithm.

This last point is a very significant one for ocean modelling, because a large number of modes is often necessary.

2.2.5 Chebyshev Polynomials

The Chebyshev polynomials, $\{T_k(x)\}_{k=0}^{\infty}$ are the eigenfunctions of the singular Sturm-Liouville problem:

$$(\sqrt{1-x^2}T_k'(x))' + \frac{k^2}{\sqrt{1-x^2}}T_k(x) = 0 \tag{34}$$

This is equation (25) with $p(x) = \sqrt{1-x^2}$, $q(x) = 0$, $w(x) = \frac{1}{\sqrt{1-x^2}}$. If $T_k(x)$ is chosen so that $T_k(1) = 1$ then we have:

$$T_k(x) = \cos(k \cos^{-1} x) \tag{35}$$

If we substitute $\theta = \cos^{-1}(x)$ we can write:

$$T_k(\theta) = \cos(k\theta) \tag{36}$$

so that a Chebyshev series is really the same as a Fourier cosine series with a change of independent variable. They satisfy the following recurrence relationship:

$$T_{k+1}(x) = 2xT_k(x) - T_{k-1}(x) \tag{37}$$

with $T_0(x) = 1$, $T_1(x) = x$ (figure 1). The inner product for the Hilbert space generated by $\{T_k(x)\}_{k=0}^{\infty}$ is:

$$< u, v >= \int_{-1}^{1} u(x)v(x)w(x)dx = \int_{-1}^{1} \frac{uv}{\sqrt{1-x^2}}dx \quad \forall u, v \in L_w^2(-1,1) \tag{38}$$

The Chebyshev polynomials are orthogonal on this space, but not orthonormal:

$$< T_j, T_k >= \frac{\pi c_k}{2}\delta_{jk} \tag{39}$$

where δ_{jk} is the Kronecker delta function, and c_k is defined as:

$$c_k = \begin{cases} 2 & k = 0 \\ 1 & k > 0 \end{cases} \tag{40}$$

From this we deduce the transform pair:

$$u(x) = \sum_{k=0}^{\infty} \hat{u}_k T_k(x) \tag{41}$$

$$\hat{u}_k = \frac{2}{\pi c_k}\int_{-1}^{1} \frac{uT_k}{\sqrt{1-x^2}}dx \tag{42}$$

In order to use a Chebyshev expansion, as in Example 2 above, we need to truncate the series in equation (41) to a finite number of terms, and to approximate the integral in equation (42) by some quadrature formula.

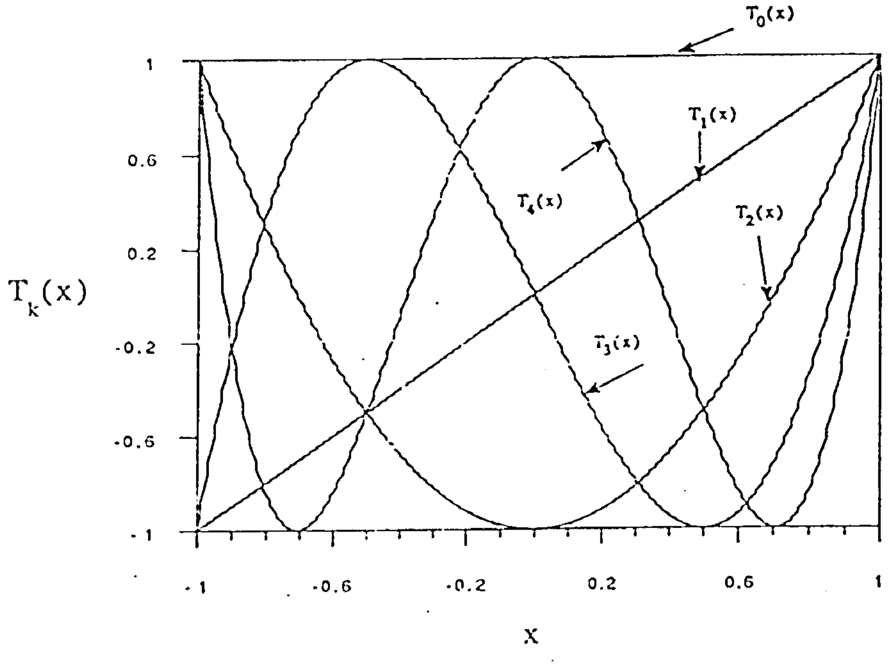

Figure 1: The first five Chebyshev polynomials on the interval $-1 \leq x \leq 1$. They are given by: $T_0(x) = 1$; $T_1(x) = x$; $T_2(x) = 2x^2 - 1$; $T_3(x) = 4x^3 - 3x$; $T_4(x) = 8x^4 - 8x^3 + 1$.

2.2.6 Gauss-Lobatto Integration

To approximate the integral in equation (42), we use the fact that a Gauss quadrature rule will give an optimal result for polynomials on the interval $(-1,1)$. The quadrature points will be the same as the collocation points, which we referred to in Example 2. The optimal points for a Gauss quadrature rule are given by the zeros of the $(N+1)^{th}$ order orthogonal polynomial retained in the truncated series - in this case, the zeros of T_{N+1}. However, as indicated by figure (1) , $T_k(-1)$ and $T_k(+1)$ are never zero. (In fact, $T_k(\pm 1) = (\pm 1)^k$). This means that the boundary points would be excluded from the set of collocation points, making it impossible to apply the boundary condition. We, therefore, select to use Gauss-Lobatto integration. Following Canuto *et al.* (1988) [7], let $\mathcal{P}_N$ denote the set of all polynomials of degree $\leq N$. The result for Chebyshev polynomials can be stated as follows:

Gauss-Lobatto Integration: Let $\{x_k\}_{k=0}^{N}$ be the points $x_0 = -1, x_N = 1$ and the $N-1$ roots of the polynomial $T'_N(x)$. Let $w_0, w_1, \ldots, w_N$ be the solution of the linear system:

$$\sum_{j=0}^{N} (x_j)^k w_j = \int_{-1}^{1} x^k w(x)dx \quad 0 \leq k \leq N.$$

Then

$$\sum_{j=0}^{N} p(x_j)w_j = \int_{-1}^{1} p(x)w(x)dx$$

for all polynomials p in $\mathcal{P}_{2N-1}$. (See Canuto *et al.* (1988, p. 57) [7]). The collocation and weight points are:

$$x_j = \cos(\frac{j\pi}{N}) \quad j = 0,\ldots,N; \qquad w_j = \begin{cases} \frac{\pi}{2N} & j = 0, N \\ \frac{\pi}{N} & 1 \leq j \leq N-1 \end{cases} \tag{43}$$

The resulting discrete Chebyshev transform pair is:

$$u^N = \sum_{k=0}^{N} \tilde{u}_k T_k(x) \tag{44}$$

$$\tilde{u}_k = \frac{2}{N\bar{c}_k} \sum_{j=0}^{N} \frac{u(x_j)}{\bar{c}_j} T_k(x_j) \tag{45}$$

where $\bar{c}_k = 2, \ k = 0; \ \bar{c}_k = 1, \ k \geq 1$.

With the choice of collocation points given by equation (43), $T_k(x_j)$ takes on a very convenient form:

$$T_k(x_j) = \cos(k \cos^{-1} x_j) = \cos(\frac{jk\pi}{N}) \tag{46}$$

This means that, as pointed out earlier, the discrete Chebyshev transform can be evaluated very efficiently using an FFT routine.

We note here also that with these collocation points the grid lines are closer together nearer the boundaries than in the interior (figure 4). This might lead one to conclude that with more grid points in the boundary regions, there is better resolution there. This is not necessarily the case. Solomonoff and Turkel (1989) [55] have carried out a study of the approximation properties of Chebyshev collocation methods. Their results show that for the approximation of a function with a "moderate" slope (*i.e.* one which can be resolved by the collocation points), the Chebyshev scheme does give better results near the boundaries with a Gauss-Lobatto grid. However, the results are also better near the boundaries when a uniform grid is used (although the approximation is not as good as with a Gauss-Lobatto grid). For the case of a function with a "steep" slope, the approximation is the same everywhere in the domain. This illustrates the fact that spectral methods are global methods and cannot be interpreted in terms of local methods. The closeness of the grid points near the boundaries serves only to counter the tendency of the approximating polynomials to oscillate with large amplitude in these regions.

2.3 Differentiation

Let us return, firstly, to the continuous Chebyshev transform given by equations (41) and (42). Differentiating the first of these equations with respect to x, and denoting the coefficients of the derivative by $\hat{u}_k^{(1)}$ we have:

$$u'(x) = \sum_{k=0}^{\infty} \hat{u}_k T_k'(x) = \sum_{k=0}^{\infty} \hat{u}_k^{(1)} T_k(x) \tag{47}$$

A relationship between the coefficients $\hat{u}_k$ and $\hat{u}_k^{(1)}$ can be found using the easily verifiable result:

$$2T_k(x) = \frac{T_{k+1}'(x)}{k+1} - \frac{T_{k-1}'(x)}{k-1} \tag{48}$$

Substituting (48) into (47) gives:

$$2k\hat{u}_k = c_{k-1}\hat{u}_{k-1}^{(1)} - \hat{u}_{k+1}^{(1)} \quad k \geq 1 \tag{49}$$

where $c_k = 2$, $k = 0$ and $c_k = 1$ $k \geq 1$. If we truncate the series expansion for $u(x)$ to N terms, then (49) gives the following recurrence relationship to compute the coefficients for the derivative:

$$\begin{aligned} &\hat{u}_k^{(1)} = 0 \quad k \geq N \\ &c_k\hat{u}_k^{(1)} = \hat{u}_{k+2}^{(1)} + 2(k+1)\hat{u}_{k+1} \quad k = N-1, N-2, \ldots, 0 \end{aligned} \tag{50}$$

The collocation derivative of the discrete Chebyshev transform (44) is simply the ordinary derivative of this finite sum at each of the points x_j. There are two ways to compute this derivative: 1) FFT method: 2) Matrix multiplication method.

FFT method: Compute the Chebyshev coefficients in (45) with an FFT routine. Then modify these coefficients using the recurrence relationship (50) and transform back again. A similar modification to the coefficients can produce second and higher order derivatives easily.

Matrix multiplication method: From the equations for the discrete Chebyshev transform, (44) and (45), it is easy to show the following holds using the orthogonality properties of discrete Fourier sums:

$$u^N(x_j) = \sum_{k=0}^{N} \tilde{u}_k T_k(x_j) = u(x_j) \tag{51}$$

This means that the collocation approximation is simply the interpolating polynomial through the data points $(x_j, u(x_j))$. The derivative can therefore be computed by differentiating the Lagrange interpolating formula. Using the notation $\mathcal{D}_N u$ to denote this derivative, the result is:

$$(\mathcal{D}_N u)(x_k) = \sum_{j=0}^{N} (D_N)_{kj} u(x_j) \quad k = 0, 1, \ldots, N \tag{52}$$

where the matrix $(D_N)_{kj}$ is computed to be:

$$(D_N)_{kj} = \begin{cases} \frac{\bar{c}_k}{\bar{c}_j} \frac{(-1)^{k+j}}{x_k - x_j} & k \neq j \\ \frac{-x_j}{2(1-x_j^2)} & 1 \leq k = j \leq N-1 \\ \frac{2N^2+1}{6} & k = j = 0 \\ -(\frac{2N^2+1}{6}) & k = j = N \end{cases} \tag{53}$$

and $\bar{c}_k$ is as defined before.

The best choice of differentiation method is dependent upon the particular choice of computer. It is therefore advisable to compare both methods for efficiency. Generally speaking, if a low number of modes is retained, the matrix multiplication method is more efficient. This means that there is a cross-over point for some number N_0 of modes, and that N_0 is machine dependent.

Chapter 3

The Model

Layered models are quite popular amongst oceanographers for the numerical simulation of the ocean circulation. In particular the 1-1/2 layer "reduced-gravity" model has been shown to be very capable of reproducing essential features observed in the real oceans. Luther and O'Brien (1985) [36] used this type of model, applying it to the northwest Indian Ocean. They were able to compute important phenomena such as the formation and coalescence of the two-gyre system during the southwest monsoon, the formation and decay of the energetic eddy field off the Arabian Peninsula during the transition period from southwest to northeast monsoon, and then the formation of the southwestward Somali Current with the onset of the northeast monsoon. Indeed much work has been done with layered models applied to the Indian Ocean (Simmons *et al.* (1988) [54], Woodberry *et al.* (1989) [64], Kindle and Thompson (1989) [32], Jensen (1991) [28]), the Pacific Ocean (Pares-Sierra and O'Brien (1989) [45], Johnson and O'Brien (1990a) [30], Johnson and O'Brien (1990b) [31]), the Atlantic Ocean (O'Brien *et al.* (1978) [43], Busalacchi and Picaut (1983) [6]) as well as to other regions of the world's oceans. Here, we present the numerical formulation of a nonlinear 1-1/2 layer "reduced-gravity" ocean model using a Chebyshev-collocation spectral method. We describe how the theory of chapter (2) is applied to our two-dimensional model. A bicharacteristic method is developed for the boundary solution and an algebraic grid-generation scheme is implemented to construct grids over non-rectangular simply-connected domains. We use a Runge-Kutta time-stepping method.

3.1 Model Equations

Under the assumption that the ocean consists of two incompressible, hydrostatic, homogeneous layers of slightly different densities ρ_1 and ρ_2 with the lower layer infinitely deep and at rest, (figure 2) the vertically-averaged equations of motion for the upper layer are :

$$\frac{\partial u}{\partial t} + u\frac{\partial u}{\partial x} + v\frac{\partial u}{\partial y} - fv = -g'\frac{\partial h}{\partial x} + \frac{\tau_x}{\rho_1 h} + A\nabla^2 u \tag{54}$$

$$\frac{\partial v}{\partial t} + u\frac{\partial v}{\partial x} + v\frac{\partial v}{\partial y} + fu = -g'\frac{\partial h}{\partial y} + \frac{\tau_y}{\rho_2 h} + A\nabla^2 v \tag{55}$$

$$\frac{\partial h}{\partial t} + \frac{\partial hu}{\partial x} + \frac{\partial hv}{\partial y} = 0 \tag{56}$$

where u and v are the eastward and northward depth-averaged velocity components respectively, h is the thickness of the upper layer, τ_x and τ_y are the wind stress components, $g' = g\frac{\rho_2-\rho_1}{\rho_2}$ is the "reduced gravity", A is the kinematic eddy viscosity and f is the Coriolis parameter. For a domain bounded by solid walls, the boundary conditions on u and v are: $u = v = 0$.

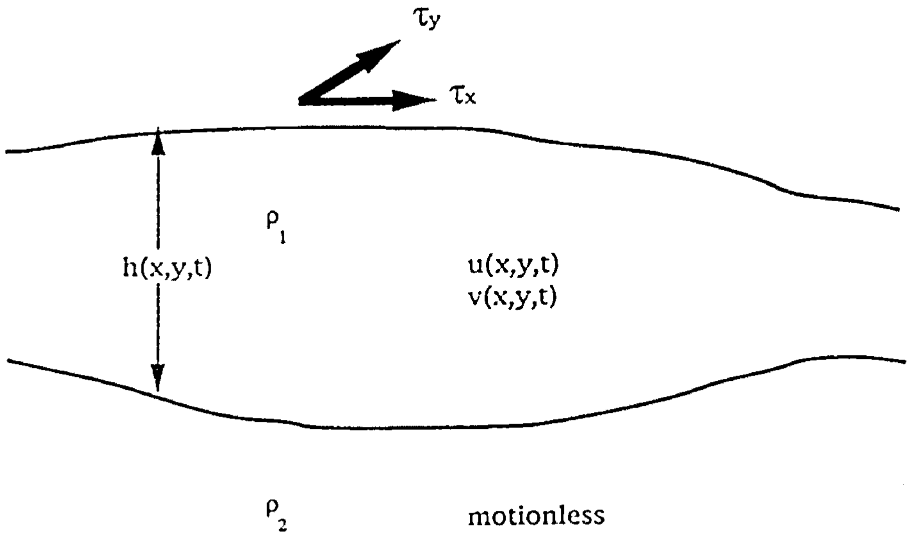

τ_y
τ_x
ρ_1
h(x,y,t)
u(x,y,t)
v(x,y,t)
ρ_2
motionless

Figure 2: Schema for a 1-1/2 layer "reduced-gravity" model.
The wind stress vector is (τ_x, τ_y), and the upper layer thickness and velocity components are h, u (eastward) and v (northward) respectively. The layer densities are ρ_1 and ρ_2, assumed to be constants. The lower layer is infinitely deep and motionless.

3.2 Numerical Formulation

We consider the square domain: $-1 \leq x, y \leq 1$. Let the variable $\psi(x, y, t)$ denote any of the dependent variables u, v and h of equations (54), (55) and (56). By firstly considering ψ as a function of x, writing down its discrete Chebyshev transform according to equations (44) and (45), then secondly considering this transform as a function of y and transforming now with respect to y, we obtain the double discrete Chebyshev transform pair:

$$\psi^{NM}(x_j, y_k, t) = \sum_{n=0}^{N} \sum_{m=0}^{M} \tilde{\psi}_{nm}(t) T_n(x_j) T_m(y_k) \tag{57}$$

$$\tilde{\psi}_{nm} = \frac{4}{MN\bar{c}_m\bar{c}_n} \sum_{j=0}^{N} \sum_{k=0}^{M} \frac{\psi^{NM}}{\bar{c}_j\bar{c}_k} \cos(\frac{jn\pi}{N}) \cos(\frac{km\pi}{M}) \tag{58}$$

where $x_j = -\cos(\frac{j\pi}{N})$, $j = 0, 1, \ldots, N$ and $y_k = -\cos(\frac{k\pi}{M})$, $k = 0, 1, \ldots, M$. We make this substitution for each of the dependent variables, *i.e.* $u \approx u^{NM}$, $v \approx v^{NM}$, $h \approx h^{NM}$, and proceed to solve equations (54), (55), and (56) as outlined earlier in Example 2. The extension of the ideas in differentiation already presented, to two dimensions is straight forward. For the matrix multiplication method we have:

$$\frac{\partial \psi}{\partial x}^{NM}(x_j, y_k, t) = \sum_{l=0}^{N} (D_N)_{jl} \psi(x_l, y_k, t); \quad j = 0, \ldots, N \;\; k = 0, \ldots, M \tag{59}$$

where $(D_N)_{jl}$ is the $(N+1)$x$(N+1)$ matrix given by equation (53). Similarly,

$$\frac{\partial \psi}{\partial y}^{NM}(x_j, y_k, t) = \sum_{l=0}^{M} (D_M)_{kl} \psi(x_j, y_l, t); \quad j = 0, \ldots, N \;\; k = 0, \ldots, M \tag{60}$$

where $(D_M)_{kl}$ is a $(M+1)$x$(M+1)$ matrix with an analogous definition to (53). We note here that it is not necessary to compute these differentiation matrices at every timestep. Once the number of modes to be used in each direction has been specified, $(D_N)_{jl}$ depends only on the known quantities (x_j, y_k), and specific constants $\bar{c}_j, \bar{c}_k$. Thus, (D_N) and (D_M) can be computed, or read in at the beginning of a computer program before the timestep loop. A similar matrix can also be computed and stored for the second derivatives.

The transform technique for computing derivatives also extends easily to two dimensions:

$$\frac{\partial \psi}{\partial x}^{NM}(x_j, y_k, t) = \sum_{n=0}^{N} \sum_{m=0}^{M} \tilde{\psi}^x_{nm}(t) T_n(x) T_m(y) \tag{61}$$

where a recursion relation similar to (50) is used to compute the coefficients $\tilde{\psi}^x_{nm}$:

$$\tilde{\psi}^x_{nm} = 0 \ \forall\, n \geq N$$

$$c_k \tilde{\psi}^x_{nm} = \tilde{\psi}^x_{n+2m} + 2(n+1)\tilde{\psi}_{n+1m} \quad n = N-1, \ldots, 0.$$

We remark here that, under a simple linear transformation of variables, the computational square domain $-1 \leq x, y \leq 1$ can be transformed into a rectangle: $x_{min} \leq x \leq x_{max}$, $y_{min} \leq y \leq y_{max}$:

$$x_j = x_{min} + \frac{1}{2}[1 + X_j](x_{max} - x_{min}) \quad j = 0, 1, \ldots, N \tag{62}$$

$$y_k = y_{min} + \frac{1}{2}[1 + Y_k](y_{max} - y_{min}) \quad k = 0, 1, \ldots, M \tag{63}$$

where $X_j = -\cos(\frac{j\pi}{N})$, $Y_k = -\cos(\frac{k\pi}{M})$. Later we shall describe how to provide for more irregular shaped domains.

3.3 Boundary Conditions

The model equations (54) - (56) form a set of parabolic quasilinear partial differential equations. However the frictional terms are small for most solutions of interest. Without these terms (*i.e.* $A = 0$), the resulting set of equations is hyperbolic. The regions where these terms are largest are close to the boundaries, but still they are an order of magnitude smaller than the local acceleration. For the following realistic choice of scales: Length $L = 100\ km$, time $T = 10$ days, velocity $V = 1\ m\,s^{-1}$, $A = 1000\ m^2\,s^{-1}$ we obtain:

$$[\frac{\partial u}{\partial t}] = \frac{V}{T} \sim O(10^{-6})\ m\,s^{-2}$$

$$[A\frac{\partial^2 u}{\partial x^2}] = 1000\frac{V}{L^2} \sim O(10^{-7})\ m\,s^{-2}$$

We, therefore, select to put the model equations in characteristic form by regarding the friction terms as right-hand-side source terms or forcing functions, along with the Coriolis force and wind stress components.

Spectral methods are very sensitive to boundary treatments. Their solutions follow very closely to the mathematical solutions to the problem. For the case of hyperbolic wave equations it is important to make a good attempt to solve for the characteristics on the boundary. Otherwise, the solution may become rapidly unstable in time. This problem may also be encountered with finite difference and finite element methods, as discussed for example by Gottlieb *et al.* (1982) [16]. In a study of the boundary treatment for hyperbolic systems using the Chebyshev collocation method and an *implicit* time differencing scheme, Canuto and Quarternoni (1987) [8] state that the *only* unconditionally stable treatment at the boundaries consists of using the prescribed physical conditions together with certain linear combinations of the differential equations which express the incoming characteristics. In our model we use an explicit Runge-Kutta method, solving the equations in characteristic form for the height field at the boundaries.

Rewriting the model equations putting the Laplacian friction terms together with the right-hand-side "forcing" terms yields:

$$\frac{\partial u}{\partial t}+u\frac{\partial u}{\partial x}+v\frac{\partial u}{\partial y}+g'\frac{\partial h}{\partial x}=F_1 \tag{64}$$

$$\frac{\partial v}{\partial t}+u\frac{\partial v}{\partial x}+v\frac{\partial v}{\partial y}+g'\frac{\partial h}{\partial y}=F_2 \tag{65}$$

$$\frac{\partial h}{\partial t}+u\frac{\partial h}{\partial x}+v\frac{\partial h}{\partial y}+h(\frac{\partial u}{\partial x}+\frac{\partial v}{\partial y})=0 \tag{66}$$

where

$$F_1=fv+\frac{\tau_x}{\rho_1 h}+A\nabla^2 u$$

$$F_2=-fu+\frac{\tau_y}{\rho_1 h}+A\nabla^2 v$$

Following Lardner *et al.* (1986) [34] we put this system of equations in characteristic form by taking the nonlinear combination $\sigma_1(64)$ $+\sigma_2(65)$ $+\sigma_3(66)$, where the σ_i $(i=1,2,3)$ are as yet unspecified functions of the dependent variables:

$$\begin{aligned}\sigma_1\frac{\partial u}{\partial t}+(\sigma_1 u+\sigma_3 h)\frac{\partial u}{\partial x}+\sigma_1 v\frac{\partial u}{\partial y}+\\ \sigma_2\frac{\partial v}{\partial t}+\sigma_2 u\frac{\partial v}{\partial x}+(\sigma_2 v+\sigma_3 h)\frac{\partial v}{\partial y}+\\ \sigma_3\frac{\partial h}{\partial t}+(\sigma_1 g'+\sigma_3 u)\frac{\partial h}{\partial x}+(\sigma_2 g'+\sigma_3 v)\frac{\partial h}{\partial y}=\sigma_1 F_1+\sigma_2 F_2\end{aligned} \tag{67}$$

The σ_i are chosen so that all three directional derivatives in (67) are constrained to lie in the same plane in $xyt-$space. Let the vector $\vec{N}=(\cos\theta,\sin\theta,N)$ denote the normal to this plane. This constraint implies:

$$(u\cos\theta + v\sin\theta + N)\sigma_1 + h\cos\theta\sigma_3 = 0 \tag{68}$$

$$(u\cos\theta + v\sin\theta + N)\sigma_2 + h\sin\theta\sigma_3 = 0 \tag{69}$$

$$(g'\cos\theta)\sigma_1 + (g'\sin\theta)\sigma_2 + (u\cos\theta + v\sin\theta + N)\sigma_3 = 0 \tag{70}$$

The two distinct solutions to this set of equations are discussed by Lardner *et al.* (1986) [34]. We choose the one which gives the ***bicharacteristics*** for the system:

$$N = a - u\cos\theta - v\sin\theta; \quad \sigma_1 = -h\cos\theta; \quad \sigma_2 = -h\sin\theta; \quad \sigma_3 = a = \sqrt{g'h}$$

where a is the local wave speed. The plane perpendicular to N is called a wave plane. As θ varies, the wave plane envelopes a cone, called the Mach cone, and is expressed by:

$$(dx - udt)^2 + (dy - vdt)^2 = a^2dt^2$$

The tangential direction of a wave plane with the Mach cone is called a bicharacteristic direction and is given by:

$$\frac{dx}{dt} = u - a\cos\theta \tag{71}$$

$$\frac{dy}{dt} = v - a\sin\theta \tag{72}$$

Equation (67), known as the *compatibility* equation, becomes:

$$\cos\theta\frac{du}{dt} + \sin\theta\frac{dv}{dt} - \frac{a}{h}\frac{dh}{dt} - a\sin\theta(\sin\theta\frac{\partial u}{\partial x} - \cos\theta\frac{\partial u}{\partial y})$$
$$-a\cos\theta(-\sin\theta\frac{\partial v}{\partial x} + \cos\theta\frac{\partial v}{\partial y}) = \cos\theta F_1 + \sin\theta F_2 \tag{73}$$

where the operator $\frac{d}{dt} \equiv \frac{\partial}{\partial t} + (u - a\cos\theta)\frac{\partial}{\partial x} + (v - a\sin\theta)\frac{\partial}{\partial y}$. Because of the fact that the Laplacian friction term has been incorporated into a forcing function, the appropriate boundary condition to apply to equation (73) at a solid wall is the "no normal flow" condition. We consider two distinct cases: (a) edge point; (b) corner point.

Edge point: Taking as an example the western boundary we select the bicharacteristic normal to the boundary and directed towards it (figure (3a)). The appropriate value for θ is the angle between the bicharacteristic direction and the x-axis measured in the sense shown. We assume that $u - a < 0$, so that $\theta = 0$ gives the bicharacteristic in the negative x-direction. A unit normal to this boundary is $\hat{n} = (\cos\theta, \sin\theta)$. The "no normal flow" condition becomes:

$$\begin{aligned} u\cos\theta + v\sin\theta &= 0 \\ \Rightarrow \cos\theta\frac{\partial u}{\partial t} + \sin\theta\frac{\partial v}{\partial t} &= 0 \\ \Rightarrow \sigma_1\frac{\partial u}{\partial t} + \sigma_2\frac{\partial v}{\partial t} &= 0 \end{aligned} \tag{74}$$

Substituting this condition into equation (67) and rearranging the terms yields:

$$\sigma_1(R_u) + \sigma_2(R_v) + \sigma_3(R_h) + \sigma_3\frac{\partial h}{\partial t} = 0 \tag{75}$$

where

$$\begin{aligned} R_u &= u\frac{\partial u}{\partial x} + v\frac{\partial v}{\partial y} + g'\frac{\partial h}{\partial x} - F_1 \\ R_v &= u\frac{\partial v}{\partial x} + v\frac{\partial v}{\partial y} + g'\frac{\partial h}{\partial x} - F_2 \\ R_h &= u\frac{\partial h}{\partial x} + v\frac{\partial h}{\partial y} + h(\frac{\partial u}{\partial x} + \frac{\partial v}{\partial y}) \end{aligned}$$

$$\Rightarrow \frac{\partial h}{\partial t} = \frac{a}{g'}[\cos\theta R_u + \sin\theta R_v] - R_h \tag{76}$$

Corner point: We take as an example the northwest corner. Let θ_W and θ_N denote the

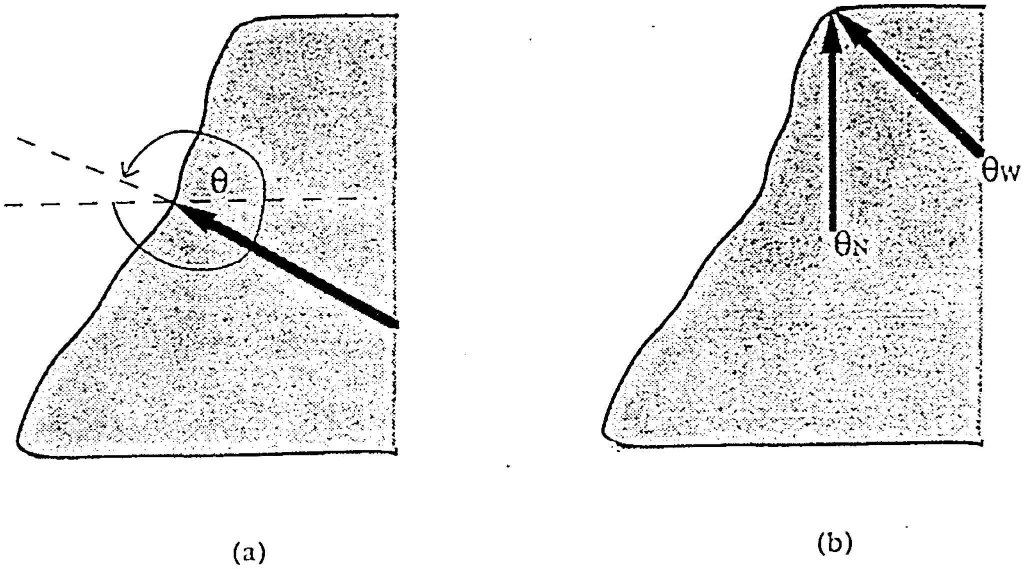

Figure 3: The western portion of the physical domain showing the bicharacteristics, directed perpendicularly towards the boundary from the interior region, used to compute the height field at boundary points: (a) At a point on the western boundary one bicharacteristic is used with angle θ measured in the sense shown. (b) At the northwest corner the two bicharacteristics normal to the northern boundary (θ_N) and western boundary (θ_W) are used.

angles corresponding to the bicharacteristics at the northwest corner normal to the western and northern boundaries respectively (figure (3b)). For each of these angles we may obtain an equation for $\frac{\partial h}{\partial t}$ similar to equation (76). Taking the average of these two equations we obtain:

$$\frac{\partial h}{\partial t} = \frac{a}{2g'}[(\cos\theta_W + \cos\theta_N)R_u + (\sin\theta_w + \sin\theta_N)R_v] - R_h \tag{77}$$

Equations (76) and (77) are integrated to compute all the boundary h values at each time step. Once the height field has been determined we revert back to the original form of the model equations (equations (54) - (56)) no longer regarding the frictional force as a source term and apply the "no-slip" conditions on the velocity fields: $u = v = 0$ on the boundaries. We remark here that equations (76) and (77) are not "new", but are simply a re-arrangement of the original model equations in order to get a better estimate for the bicharacteristics on the boundaries and thus obtain solutions which are stable in time.

3.4 Numerical Grid Generation

In this section we outline the construction of a non-orthogonal grid over an irregular domain bounded by four specified curves. The coordinate transformation from physical space to computational space does, of course, alter the model equations by introducing certain mapping factors in the derivative terms. An algebraic grid generation method is used.

3.4.1 Two-Dimensional Coordinate Transformation

We denote the original coordinate system in physical space by the variables (x, y) and the transformed system by (X, Y). In general, for a non-orthogonal system, we require two sets of basis vectors: The *covariant* basis vectors $(\vec{e}_i)$ and the *contravariant* basis vectors $(\vec{e}^i)$. They are defined simply as follows:

$$\vec{e}_i = \frac{\partial \vec{r}}{\partial X^i}\ ; \quad \vec{e}^i = \nabla X^i \quad i = 1, 2$$

where $X^1 = X,\ \ X^2 = Y$ and $\vec{r} = \vec{r}(X, Y)$ is the position vector. Thus the covariant basis vectors are parallel to the coordinate lines in physical space and the contravariant basis vectors are perpendicular to the level curves of the transformed coordinates in physical space (figure 4). For a detailed coverage of coordinate transformation and grid generation see Thompson *et al.* (1985) [57].

The volume element in the transformed system is :

$$dV = JdXdY$$

where J = Jacobian = $(\frac{\partial x}{\partial X}\frac{\partial y}{\partial Y} - \frac{\partial x}{\partial Y}\frac{\partial y}{\partial X})$. The relationship between the contravariant and the covariant vectors is:

$$\vec{e}^i = \frac{1}{J}(\vec{e}_j \times \vec{e}_k) \tag{78}$$

with i, j, k cyclic in 1, 2, 3 and taking $\vec{e}^3 = \vec{e}_3 = \hat{k}$, the unit vector perpendicular to the (x, y) plane. The conservative forms of the gradient and Laplacian operators for any scalar A are:

$$\nabla A = \frac{1}{J}\sum_{i=1}^{2}\frac{\partial J\vec{e}^i A}{\partial X^i} \tag{79}$$

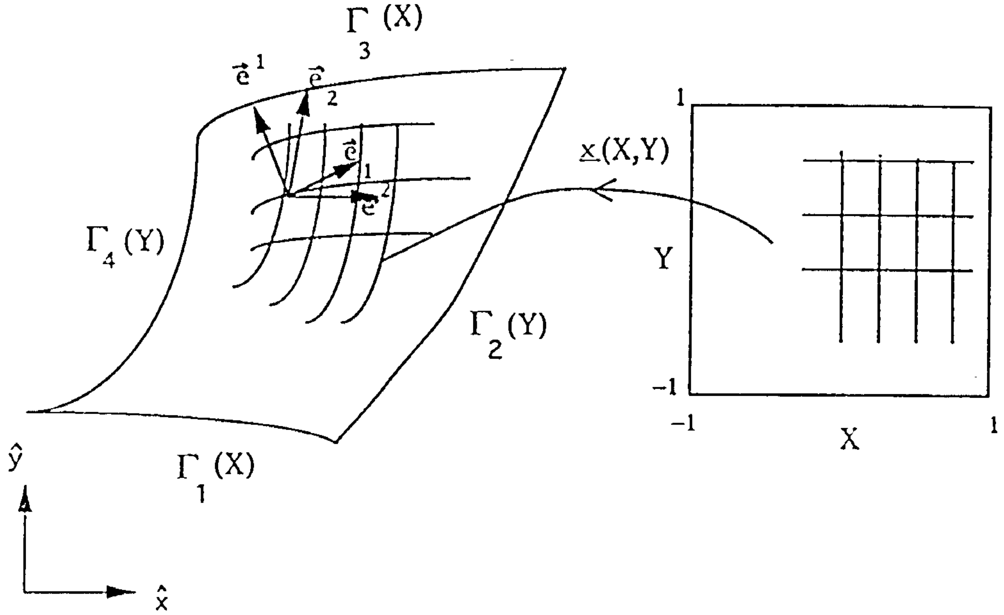
Γ_3 (X)
$\vec{e}^1$
$\vec{e}_2$
$\vec{e}_1$
$\vec{e}^2$
Γ_4 (Y)
Γ_2 (Y)
Γ_1 (X)
$\underline{x}$(X,Y)
1
Y
−1
−1
X
1
$\hat{y}$
$\hat{x}$

Figure 4: The mapping function $\underline{x}$ maps the square computational domain into the irregular physical domain bounded by four specifiable curves: Γ_1, Γ_2, Γ_3, and Γ_4.

The vectors $\vec{e}^i$ are the contravariant basis vectors at each point and the $\vec{e}_i$ are the covariant basis vectors.

$$\nabla^2 A = \frac{1}{J}\sum_{i=1}^{2}\sum_{j=1}^{2}\frac{\partial}{\partial X^i}(\vec{e}^{\,i}\cdot\vec{e}^{\,j}J\frac{\partial A}{\partial X^j}) \tag{80}$$

Let $(\hat{x}, \hat{y})$ denote orthonormal basis vectors in cartesian coordinates. From equations (78) above we have:

$$\begin{aligned} J\vec{e}^{\,1} &= \frac{\partial y}{\partial Y}\hat{x} - \frac{\partial x}{\partial Y}\hat{y} \\ J\vec{e}^{\,2} &= -\frac{\partial y}{\partial X}\hat{x} + \frac{\partial x}{\partial X}\hat{y} \end{aligned}$$

Substituting these expressions into equation (79) yields:

$$\begin{aligned} \nabla A &= \frac{\partial A}{\partial x}\hat{x} + \frac{\partial A}{\partial y}\hat{y} \\ &= \frac{1}{J}[\frac{\partial}{\partial X}(A\{\frac{\partial y}{\partial Y}\hat{x} - \frac{\partial x}{\partial Y}\hat{y}\}) + \frac{\partial}{\partial Y}(A\{-\frac{\partial y}{\partial X}\hat{x} + \frac{\partial x}{\partial X}\hat{y}\})] \end{aligned}$$

$$\Rightarrow \frac{\partial A}{\partial x} = \frac{1}{J}[\frac{\partial}{\partial X}(\frac{\partial y}{\partial Y}A) - \frac{\partial}{\partial Y}(\frac{\partial y}{\partial X}A)] \tag{81}$$

$$\frac{\partial A}{\partial y} = \frac{1}{J}[-\frac{\partial}{\partial X}(\frac{\partial x}{\partial Y}A) + \frac{\partial}{\partial Y}(\frac{\partial x}{\partial X}A)] \tag{82}$$

For the model equations, all first order spatial derivatives are computed according to equations (81) and (82) and the friction terms using equation (80). Note that the number of derivatives in each case to be computed in the transformed coordinates is exactly double the number of derivatives in the original cartesian coordinates.

3.4.2 Mapping Procedure

We assume that the physical domain is bounded by four specifiable curves: $\Gamma_1(X)$, $\Gamma_2(Y)$, $\Gamma_3(X)$, $\Gamma_4(Y)$ where $0 \le X, Y \le 1$ (figure 4). We use the *transfinite* grid generation procedure to construct a grid over this physical domain. This essentially consists of doing a "linear blending" of curve Γ_1 into its opposite side Γ_3 and Γ_4 into Γ_2. The coordinates

$\underline{x} = (x, y)$ in physical space are given in terms of the transformed coordinates (X, Y) according to:

$$\begin{aligned}\underline{x}(X, Y) = {} & (1 - X)\Gamma_4(Y) + X\Gamma_2(Y) + (1 - Y)\Gamma_1(Y) \\ & + Y\Gamma_3(X) - (1 - X)(1 - Y)\Gamma_1(0) - (1 - X)Y\Gamma_3(0) \\ & - X(1 - Y)\Gamma_1(1) - XY\Gamma_3(1) \qquad (83)\end{aligned}$$

Although we think of mapping the physical domain into a square, it is more usual to express the mapping in the above form, *i.e.* where the transformed coordinates (X, Y) are the independent variables. It is not always possible to obtain an analytical expression for the inverse mapping.

An example of a grid constructed using this type of mapping is shown in figure (5). The physical domain is a section of the western Indian Ocean basin from 10°S to 25°N, excluding the Gulf of Aden, extending 10,000 km eastwards into the basin. The western boundary is approximated by a polynomial of degree 8. The points on each boundary, through which the grid lines pass, are selected according to an arc-length parameterization of each curve. In other words, for a regular spaced grid in the computational square domain (*i.e.* not a Gauss-Lobatto grid) the points would be equidistant along each boundary. This yields a more even grid particularly in cases where opposite boundaries are irregular and not near the same length. An uneven grid can greatly affect the stability properties of the numerical method.

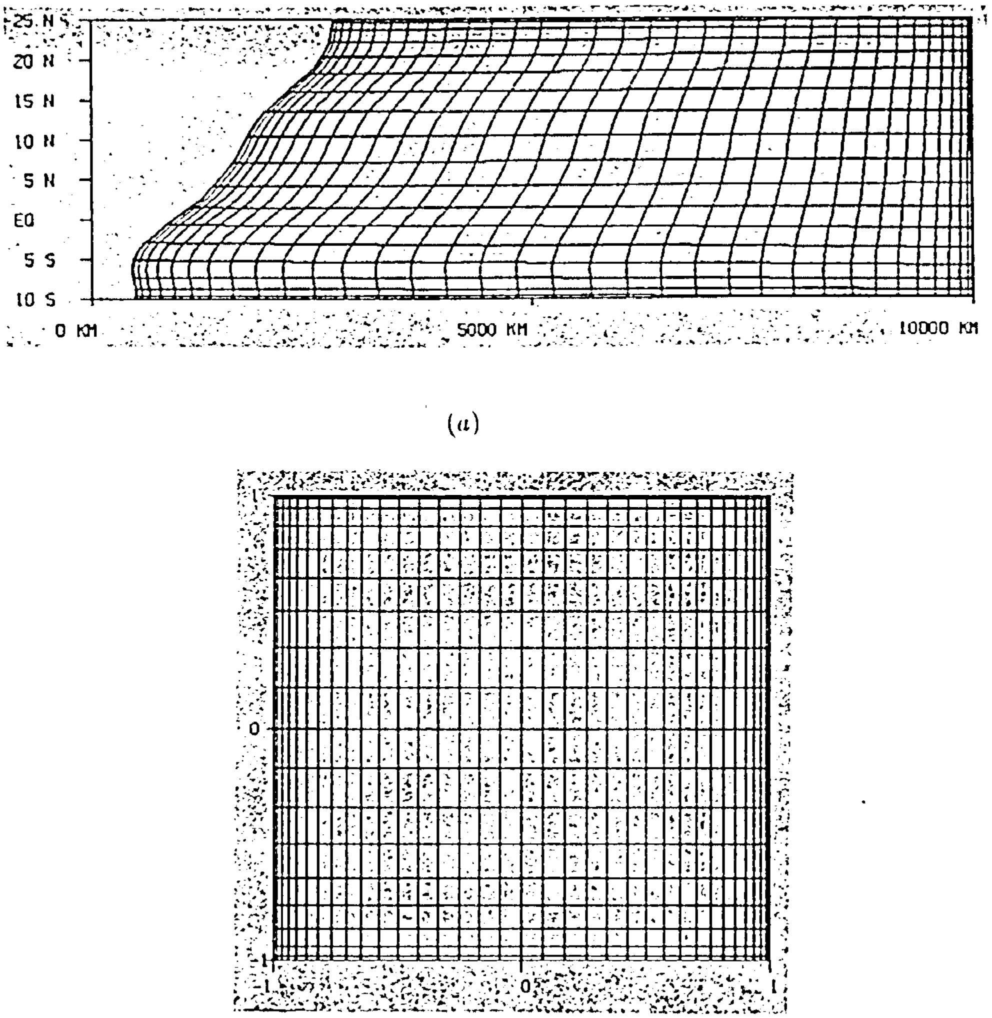
25 N
20 N
15 N
10 N
5 N
EQ
5 S
10 S
0 KM
5000 KM
10000 KM
1
0
-1
-1
0
1

(a)

(b)

Figure 5: (a) Physical domain showing a section of the Indian ocean from 10S to 25N, excluding the Gulf of Aden. (b) The square computational domain illustrating a Gauss-Lobatto grid.
Note the closeness of the grid lines near the boundaries. This does not improve the accuracy near the boundaries, but rather serves to prevent large oscillations in the polynomial approximations in these regions.

3.5 Time Differencing Scheme

On applying the finite Chebyshev series expansion given by equation (57) to the model equations (54) – (56), there results a system of differential equations to be solved in time, as described in EXAMPLE 2 of section (2.1). We can express the equations to be solved in the form:

$$\underline{u} = \begin{bmatrix} u_0 \\ \vdots \\ u_N \end{bmatrix}$$

$$\frac{\partial \underline{u}}{\partial t} = L_N \underline{u} \tag{84}$$

(with similar expressions for $\underline{v}$ and $\underline{h}$) where L_N is the nonlinear spatial approximation operator. The matrix L_N is similar to a diagonal matrix Λ, and we can rewrite equation (84):

$$\frac{\partial \underline{w}}{\partial t} = \Lambda \underline{w} \tag{85}$$

where $L_N = p\Lambda p^{-1}$ and $\underline{w} = p^{-1}\underline{u}$. The matrix Λ is diagonal whose nonzero elements are the eigenvalues of the operator L_N. This implies that the system of equations is now decoupled. The k^{th} equation is:

$$\frac{\partial w_k}{\partial t} = \lambda_k w_k \tag{86}$$

with λ_k being the k^{th} eigenvalue. The region of absolute stability for a particular time integration scheme is the set of all $\lambda \Delta t$ in the complex plane for which the solution does not grow in time. Solomonoff and Turkel (1989) [55] indicate the following reasons for using a fourth order Runge-Kutta method for the Chebyshev collocation scheme:

- It is closer to the high spatial accuracy of this numerical method than a second order formula.
- The region of stability includes a significant portion of the left-half complex plane, with a comparatively large section of the imaginary axis (see Canuto *et al.* (1988) [7]).

We use the following formulation of a Runge-Kutta method applied to equation (84), denoting by $\underline{u}^n$ the value of $\underline{u}$ at time level n:

```
Initialize $\underline{u}^* = \underline{u}^n$
for $k = 4, 1, -1$
    $\underline{u}^* = \underline{u}^n + \frac{\Delta t}{k} L_N(\underline{u}^*)$
end for
$\underline{u}^{n+1} = \underline{u}^*$
```

This yields a fourth order accurate scheme (for linear problems) and requires only two levels of storage.

Spectral methods usually have severe time-step restrictions in comparison with finite difference methods. The CFL stability criterion for finite difference schemes applied to the one-dimensional advection equation ($\frac{\partial u}{\partial t} + a\frac{\partial u}{\partial x} = 0$) is of the form:

$$\frac{\Delta t}{\Delta x}|a| \le Const. \tag{87}$$

Since $\Delta x = O(\frac{1}{N_{fd}})$, where N_{fd} is the number of spatial grid points, we have:

$$\Delta t \le \frac{Const.}{N_{fd}} \tag{88}$$

Gottlieb and Tadmor (1991) [18] present a study of the CFL condition for spectral approximations to hyperbolic problems. Using the Chebyshev collocation method with N_{sp} being the highest order basis function retained (*i.e.* $N_{sp}+1$ collocation points), they derive the following stability criterion for Runge-Kutta time differencing:

$$\Delta t|a|(\lambda_{N_{sp}} + \frac{2}{\Delta x_{min}}) \leq Const. \tag{89}$$

where $\lambda_{N_{sp}}$ is the N_{sp}^{th} eigenvalue and Δx_{min} is the minimum spacing between grid lines on a Gauss-Lobatto grid. Since $\Delta x_{min} \sim O(\frac{1}{N_{sp}^2})$ and $\lambda_{N_{sp}} \sim O(N_{sp}^2)$, this implies:

$$\Delta t \leq \frac{Const.}{N_{sp}^2} \tag{90}$$

Comparing (90) and (88) it would appear that the spectral method requires a much shorter time step, but it must be remembered that for the same degree of accuracy $N_{sp} << N_{fd}$. Spectral methods are in general more expensive with CPU time than finite difference methods. For a quantitative comparison, with a linear model, see Jensen and Kopriva (1988) [29].

It has been argued, heuristically, that the severe time restriction for the spectral collocation method is due to the closeness of the grid lines near the boundaries: $\Delta x_{min} \sim (\frac{1}{N_{sp}^2})$ (figure 4a). This is a misleading argument and indeed using a uniform grid would not give a larger allowable time step. Equation (89) shows that there are two influencing factors on the stability criterion, namely, the size of the eigenvalue $\lambda_{N_{sp}}$ and the size of $\frac{1}{\Delta x_{min}}$, both of which are $O(N_{sp}^2)$. In fact, it is possible to construct problems where the stability criterion is governed solely by $\lambda_{N_{sp}}$ and independent of the minimal grid size, as Gottlieb and Tadmor (1991) [18] have shown.

Chapter 4

Previous Studies on Yanai Waves

4.1 Introduction

In recent times, interest has been growing in the observed instability waves of the equatorial oceans. They appear as seasonally modulated, near-surface waves with period around one month and zonal wavelength of approximately 1000 km. Observations taken from the Pacific, Atlantic and Indian Oceans have detected these waves within a latitude band between 3°S and 5°N approximately. Simulation studies have also been performed, with the instabilities appearing as wave-like oscillations in the northward component of the velocity field and in the sea surface temperature just north of the equator. Possessing a group velocity that is both eastward and downward, the waves provide a mechanism for transporting energy both to the east and to the deep interior oceans. They play a major role in the momentum balance of the surface regions of the equatorial oceans and it has also been suggested that they play a similar role in the heat balance through meridional convergence towards the equator. These characteristics indicate the presence of Yanai waves (or mixed Rossby-gravity waves). In this chapter we describe some of the previous important studies that have been carried out on these waves.

4.2 Historical Background

4.2.1 Observations

The near-surface flows in the equatorial regions of the oceans are characterized by strong zonal currents. The strongest of these currents is the equatorial undercurrent (EUC) flowing to the east with speeds sometimes surpassing 100 $cm\, s^{-1}$. The EUC is flanked on either side by the westward flowing south equatorial current (SEC). North of the equator there are the eastward flowing north equatorial counter-current (NECC) and the westward flowing north equatorial current (NEC). (The Indian Ocean is an exception as the zonal equatorial currents there reverse four times during each year in response to the reversal of the monsoon winds). The horizontal shears existing between these oppositely moving currents may produce instabilities in the equatorial flow (barotropic instability). Instability waves have been observed and it is widely believed that they are a result of the barotropic shear between the SEC and the NECC.

Interest in these waves began following the observations of meridional oscillations of the SEC and the EUC during the GARP Atlantic Tropical Experiment (GATE) in the summer of 1974. These observations are described by Duing *et al.* (1975) [12]. Using ship data collected from meridional crossings of the equator at 23°30'W and 28°W they observed meandering motions in the flow fields as well as the temperature and salinity fields from the surface to well below the core of the EUC. The core of the EUC was seen to oscillate approximately $\frac{1}{2}$°on either side of the equator. They reported a wavelength of 2600 ± 390 km, phase speed 1.9 ± 0.3 $m\,s^{-1}$ westwards and a meander period of 16 ± 2 days as being compatible with the available observations. Subsequent studies by Weisberg (1979) [59] and Weisberg *et al.* (1979) [62] using data also collected during the GATE experiment show that these 16-day meanders appear above the EUC but longer period waves of about one month radiate downward and upward with westward phase propagation. Deep current measurements taken by Harvey and Patzert (1976) [26] produced the first evidence of 25-day waves in the eastern equatorial Pacific. From data collected using near-bottom current recorders, they isolated oscillations of wavelength 1000 km, amplitude 4 $cm\,s^{-1}$, propagating westwards at 50 $cm\,s^{-1}$ approximately, and suggested that the wave was a first-mode baroclinic Rossby wave trapped at the equator. Evidence of similar westward propagating long waves in the eastern equatorial Pacific surface layers was presented by Legeckis (1977) [35]. The westward flowing SEC has relatively low temperature waters because of equatorial upwelling and the advection of cold waters from the coast of South America. The oppositely flowing NECC advects relatively warm waters from the west. Consequently there are large latitudinal temperature gradients, especially in the eastern Pacific, and a sea-surface temperature front (known as the *equatorial front*) is visible on satellite produced infrared images. Legeckis (1977) [35] detected long waves in the equatorial front from satellite images taken during 1975, propagating to the west with a period of about 25 days and wavelength around 1000 km. He also noted a decrease in wavelength from about

1200 km to 800 km going from east to west which indicated the presence of a wave packet with the long waves having a greater group velocity.

The mathematical stability analysis of these equatorial zonal currents was addressed by Philander (Philander (1976) [47] and Philander (1978) [48]). He was able to show, using a realistic zonal velocity profile of the surface currents in the equatorial Atlantic and Pacific, that the most unstable waves have a period and wavelength around 1 month and 1100 km respectively and propagate to the west. These scales were independent of the changes in the velocity scale of the mean currents and Philander (1978) [48] proposed this as an explanation for the observed waves. A comparison of the mean zonal profile used by Philander (1978) [48] and an estimate of the true profile obtained from drifter buoy data was presented by Hansen and Paul (1984) [25] and showed a good agreement between the two apart from a displacement of about 1°latitude. Philander's hypothesis is very plausible and there is a general consensus that this is the generating mechanism for the instability waves at least in the eastern parts of the equatorial Atlantic and Pacific Oceans.

Evidence for the vertical propagation and surface generation of the waves in the Gulf of Guinea was discussed by Weisberg *et al.* (1979) [61] based on data collected from an array of current meter recorders. They described the waves as equatorially trapped vertically propagating Yanai (Rossby-gravity) waves and presented an analysis of their kinematics, dynamics and energetics. This research was extended by Weisberg and Horigan (1981) [60] where they discussed the seasonal variability of the waves. The observations were taken from current meters located on the equator at 3°W, at depths between 558 m and 1936 m. They calculated the group velocity using a ray tracing argument and estimated that it took

2 - 3 months for the wave packet to reach the observational depth from a source in the central Atlantic around 15°W. The authors illustrated the seasonal variation of the waves and suggested a generation time during the July to August maximum trade wind period in the central Atlantic. In other words, the subsurface waves observed appeared to be a result of waves generated by surface instabilities between the SEC and the NECC further to the west and thus the waves provided a stabilizing effect for these currents.

The structure of the currents in the equatorial Indian Ocean is quite different to that of the Atlantic and Pacific. The zonal wind and the zonal surface current reverse four times per year. (For an excellent description of these currents as modelled by a 1-1/2 layer reduced-gravity model driven by mean monthly winds, see Woodberry *et al.* (1989) [64]). Nevertheless, instability waves as described above for the eastern Pacific and Atlantic have also been observed in the Indian Ocean, but in the *western* part of the basin. They were first discovered in the moored records of the meridional velocity field as described in Luyten and Roemmich (1982) [37], although the authors did not discuss these waves. (See figure 5(c) of their paper). Reverdin and Luyten (1986) [51] observed 26-day oscillations from current records at depths of 200 m and greater between 47°E and 62°E. They were also able to infer a surface expression of these waves from drifter buoy data. In June and July (the beginning of the south west (SW) summer monsoon) of 1976, 1979 and 1981 buoys deployed on the equator in the western Indian Ocean drifted in a clockwise gyre centred on the equator at 50°E with a period of about 25 to 30 days. During the peak of the SW monsoon at the end of July buoys away from the coast started to meander meridionally with a period of 20 - 30 days. In August of 1979 one of the buoys happened to be located close to a mooring on the equator at a nominal depth of 155 m at 62°E. Energetic oscillations were detected by the current meter one month later with a period of approximately one month. These oscillations were predominantly in the meridional direction and in September the phases in the buoy and current meter data were close although the amplitude at the surface was at least twice as large as that at 160 m depth. The fact that the meanders were observed earlier at the surface suggests that energy propagated downwards in a similar fashion as that hypothesised by Weisberg and Horigan (1981) [60] for the case of the eastern equatorial Atlantic. The authors also suggested that the upper ocean circulation was a candidate for the generation of these waves because the observations seemed to imply a source of energy during the late summer monsoon. At this time the circulation does bear some resemblence to that of the Atlantic and Pacific Oceans with an eastward flow north of the equator and a westward flow to the south. However there are some obvious differences too. For example, the thermocline is deeper in the western Indian Ocean and there is no equatorial front. Also there is no equivalent to the Somali Current system elsewhere with its semi-annual reversal and complex gyre system. Another important difference is the fact that buoys in the region 0°- 5°N in the Indian Ocean during the oscillations drifted towards the east. In the other oceans the westward drift (see, *e.g.*, Hansen and Paul (1984) [25]) is believed to be important in the generation of these waves, in accordance with the stability analysis of Philander (1978) [48]. These results seem to indicate that there are possibly other generating mechanisms for the waves at least in the western Indian Ocean.

Further observational evidence for the existence of 26-day waves in the Indian Ocean was provided by Tsai (1990) [58]. In an analysis of SST data obtained from the NOAA-9 satellite he isolated antisymmetric long waves trapped within 6 degrees latitude of the equator between 52°E and 60°E and demonstrated the similarity in structure between these waves and linear Yanai waves.

Another distinguishing feature in the observations of the equatorial instability waves is the distinct frequency separation between the time scales for the eastward velocity component (4 - 8 months) and the northward component (1 month). This was noticed, *e.g.*, by Weisberg and Horigan (1981) for the Atlantic Ocean and by Luyten and Roemmich (1982) for the Indian Ocean.

The importance of the instability waves with regard to their effect on the momentum and heat budgets was studied by Hansen and Paul (1984) [25] for the Pacific Ocean and by Weisberg and Weingartner (1988) [63] for the Atlantic Ocean. Hansen and Paul reported a significant conversion of mean potential energy to eddy energy with approximately equal contributions from barotropic and baroclinic instability. They estimated the barotropic contribution could be as much as an applied wind stress of about 0.3 $dynes\,cm^{-2}$ which is quite significant in comparison to the annual and interannual variations in wind stress. Both studies discovered a similar meridional convergence of eddy heat flux towards the equator. For the case of the Atlantic Hansen and Paul (1984) [25] estimated this heat flux to be about $\frac{2}{3}$ the value of the equatorial cooling due to upwelling and Ekman divergence along the equator. Another point of interest to note from the results of these investigations is that the wave generation did not occur exactly in the shear region between the SEC and the NECC, but rather further south of this region. The waves observed by Legeckis

(1977) [35] from satellite images appeared with cusp-like peaks and smooth troughs. Each of the troughs had an anticyclonic eddy moving westward with the phase of the wave while a cyclonic eddy resided south of the peaks. It was in the cyclonic shear region of the SEC between the equator and .75°N that the waves were generated rather than in the shear region between the SEC and the NECC, according to Weisberg and Weingartner (1988) [63]. Hansen and Paul (1984) [25] noted that the equatorial front was not in fact the boundary between the SEC and the NECC but rather that westward flow continued to exist about 300 *km* further to the north of the wave troughs.

More recently, evidence for the existence of 30-day instability wave packets in the western and central Pacific has been noted. They appear to be less energetic in the west than in the region of strong latitudinal shear in the east. Perigaud (1990) [46] analyzed Geosat data of sea-level variations across the equatorial Pacific over a 26-month period and identified three disconnected regions of wave activity in the 28 – 40 day frequency band: West of 175°E; between 160°W and 175°E; east of 160°W. There was an increase in the period of the waves in going from east to west. An energy high along 6°N was noticed and the waves here varied from about 33 days in the east to 40 days in the west. This increase in the period can be explained as being due to the dispersion of Yanai waves: The waves with larger period have shorter wavelengths and smaller group velocities. If the generating mechanism for these waves is the latitudinal shear between the zonal currents then one would expect there to be a high correlation between wave amplitude and shear strength. However, Perigaud (1990) found a very low correlation (.05) between the maximum wave amplitude and the maximum meridional gradient absolute value. This result suggests that there may be other generating mechanisms for the waves in the Pacific, particularly the western region. In fact, McPhaden *et al.* (1990) [39] proposed that observed oscillations of the meridional velocity in the 10 – 30 day period band in the western Pacific could be remotely forced by the wind. Yanai waves can be generated by a cross-equatorial wind stress. Chiswell and Luckas (1989) [9] observed 10-day period Yanai waves in the central Pacific and showed that they probably originated in the western Pacific where the wind stress was coherent with them, allowing for wave dispersion.

4.2.2 Numerical Experiments

There has been some research work done on the equatorial long waves using numerical models although not as extensively as has been done with observations and data analysis. The first major numerical investigations were carried out by Cox (1980) [11] using a multi-level primative equation model. He was able to reproduce many of the observed features of these waves. Simulations of the Pacific ocean were performed using long-term averaged monthly-varying wind stress. Instability waves similar to those reported by Legeckis (1977) [35] were evident by mid-September north of the equator in the eastern part of the ocean. They did not extend as far to the east as the waves observed by Legeckis. The peak in the eddy activity resulting from the waves was seen to follow soon after the peak in the shear of the mean currents during late summer giving credence to the hypothesis that the waves were caused by a barotropic instability resulting from this shear. Cox (1980) [11] also performed a series of experiments using the same numerical model applied to a zonal channel domain centred on the equator with solid wall boundaries north and south and cyclic east – west boundary conditions. The model was initiated by a random perturbation meridional velocity field over the upper 233 metres of the domain, superposed upon a mean zonal velocity field taken from the output during August of the Pacific model. A spectral analysis of the meridional velocity field taken at the surface and 3°N revealed that the waves with periods around 30 days grew most rapidly. The experiments also revealed that the mean stratification could be as significant in contributing to the instabilities as the meridional shear: On reducing the vertical stratification a more intense horizontal divergence resulted which had a destabilizing effect on the westward flowing SEC. (Philander (1978) [48] has shown that the most unstable waves in the equatorial Atlantic and Pacific are westward propagating). Baroclinic instability while present, had a very low growth rate. The Pacific model simulations of Cox (1980) [11] also demonstrated the westward and upward phase velocity of the waves and their eastward and downward group velocity, as has been described from observational data by Weisberg *et al.*(1979) [61] in the Atlantic Ocean and by Reverdin and Luyten (1986) [51] in the Indian Ocean.

Philander *et al.* (1986) [49] reported on the results from general circulation models of the Atlantic and Pacific driven by the Hellerman and Rosenstein mean monthly winds (Hellerman and Rosenstein (1983) [27]). The instabilities appeared as equatorial waves non-homogeneous in space and non-stationary in time with period around one month and zonal wavelength around 1000 *km*. In both oceans the waves transported heat and momentum, with results near the surface in good agreement with the measurements of Hansen and Paul (1984) [25]. Although the heat flux by the waves was comparable to that across the ocean surface, their meridional heat transport was small (about 10%) compared to the net northward annual mean heat flux across the equator in both oceans, due to the fact that the eddies were effective only over the upper ocean.

Equatorial oscillations with period around one month for the Indian Ocean were simulated by the numerical models of Kindle and Thompson (1989) [32] and Woodberry *et al.* (1989) [64]. Both models were forced by the monthly mean climatological winds of Hellerman and Rosenstein (Hellerman and Rosenstein (1983) [27]). In a time versus longitude plot of meridional transport across the equator Woodberry *et al.*(1989) [64] discovered wave packets with zonal wavelength 500 – 650 km increasing slightly in the east, westward phase speed ($\sim$ 20 $cm\,s^{-1}$) and eastward group velocity ($\sim$ 24 $cm\,s^{-1}$). Kindle and Thompson presented spectral plots of the zonal and meridional velocity fields on the equator at 62°E from years 6 through 9 of their simulations. The results are in good agreement with the observations reported by Luyten and Roemmich (1982) [37] and by Reverdin and Luyten (1986) [51]: The zonal component was dominated by a semi-annual period and the meridional component by a 27-day period with little energy in the semi-annual period. A sequence of contour plots, begining in late August, of the meridional velocity field showed an intense wave packet generated from the western boundary symmetric about the equator, with increasing wavelength from west to east indicating the presence of Yanai waves.(See figure (14) in the next chapter). The authors believed that the wave packet was generated by an instability associated with the circulation of the southern gyre with the northward movement of the gyre being an important part of the generation. However, they pointed out that the waves were excited in other years too when there was no real movement of the gyre at all. In addition, the authors noted that this mechanism does not explain why the waves were generated during the NE monsoon and while they believed that "the unstable nature of the western boundary is the primary cause of the 26-day oscillation" they also recognized "direct wind forcing as an alternative mechanism and a potential contributor to the observed Yanai wave energy in the 20 – 30 day band".

Moore and McCreary (1990) [41] investigated the excitation of equatorial waves at a western boundary using a linear continuously stratified model. They forced the model with a wind patch at the western boundary of zonal extent 2500 km and oscillating at periods of 30 and 60 days. Different cases were examined where the wind was directed either meridionally or zonally with the boundary oriented meridionally or at an angle of 45°. Kelvin and Yanai waves were generated by the 30-day period wind while at the 60-day period short Rossby waves were generated in addition to these waves. They demonstrated that the western boundary is an efficient source for these waves and that the slant of the western boundary can effect the solution. For example, when the boundary was tilted at 45°to the zonal direction, an oscillating zonal wind patch can excite Yanai waves in addition to the Kelvin waves but when the boundary was purely meridional only the Kelvin waves were excited. The authors also claimed that, unlike the Kelvin waves, the Yanai waves were almost entirely indirectly forced at the western boundary rather than directly by the wind forcing area, due to the fact that the Yanai waves had short wavelengths in comparison to the zonal scale of the wind patch. Nevertheless, the Yanai waves did respond to the change in the period of the wind: The 60-day zonal wind generated Yanai waves of wavelength 347 km whereas the 30-day wind generated waves of length 840 km.

Chapter 5

On A Generating Mechanism for Yanai Waves

In the previous chapter we presented an overview of the observational and numerical studies that have been carried out on Yanai waves in the equatorial regions of the world's oceans. For the most part there appears to be a general agreement amongst the scientists who have studied these instability waves that the generating mechanism is a barotropic shear instability between the equatorial zonal currents in the equatorial front region – at least for the case of the eastern Pacific and Atlantic oceans. Scientists have argued that there is a different generating mechanism for the waves in the western Indian Ocean (Kindle and Thompson (1989) [32]). In this chapter we investigate the possibility that these waves may also be generated by a cross-equatorial wind stress over the oceans. This may be a more likely cause for the waves in the Indian Ocean. We begin with a description of linear equatorial free waves on an unbounded domain and derive analytical expressions for Yanai waves.

5.1 Linear Equatorial Free Waves

The derivation of the analytical expressions for linear equatorial waves have previously been presented in the literature, with applications to both the atmosphere (*e.g.* Matsuno (1966) [38]) and the ocean (*e.g.* Moore and Philander (1977) [42]). Here we give an outline of the derivation of the dispersion relations for these waves with particular focus on the Yanai wave. Consider the linear equations for a 1-1/2 layer reduced-gravity model with no forcing or friction:

$$\frac{\partial u}{\partial t} - \beta y v + \frac{\partial \phi}{\partial x} = 0 \tag{91}$$

$$\frac{\partial v}{\partial t} + \beta y u + \frac{\partial \phi}{\partial y} = 0 \tag{92}$$

$$\frac{\partial \phi}{\partial t} + c^2 \left(\frac{\partial u}{\partial x} + \frac{\partial v}{\partial y}\right) = 0 \tag{93}$$

where $\phi = g'h$ is the "geopotential" and $c = \sqrt{g'h_0}$ is the internal gravity wave speed, the constant h_0 being the upper layer thickness when the fluid is at rest. Equations (91) - (93) are the linearized versions of equations (54) - (56) without forcing and friction. It is convenient to non-dimensionalize the equations by choosing the following length scale L and time scale T:

$$L = \sqrt{\frac{c}{\beta}}; \qquad T = \sqrt{\frac{1}{c\beta}} \tag{94}$$

The quantity L is the equatorial Rossby deformation radius. Denoting all non-dimensional quantities with a prime the transformed system becomes:

$$\frac{\partial u'}{\partial t'} - y'v' + \frac{\partial \phi'}{\partial x'} = 0 \tag{95}$$

$$\frac{\partial v'}{\partial t'} + y'u' + \frac{\partial \phi'}{\partial y'} = 0 \tag{96}$$

$$\frac{\partial \phi'}{\partial t'} + \frac{\partial u'}{\partial x'} + \frac{\partial v'}{\partial y'} = 0 \tag{97}$$

We shall drop the prime for notational convenience and for the remainder of this section all quantities are non-dimensional. We seek normal mode solutions to these equations of the form:

$$\begin{pmatrix} u \\ v \\ \phi \end{pmatrix} = \begin{pmatrix} \bar{u}(y) \\ \bar{v}(y) \\ \bar{\phi}(y) \end{pmatrix} e^{i(kx-\omega t)} \tag{98}$$

Substituting (98) into (95) - (98) gives:

$$-i\omega\bar{u} - y\bar{v} + ik\bar{\phi} = 0 \tag{99}$$

$$-i\omega\bar{v} + y\bar{u} + \frac{d\bar{\phi}}{dy} = 0 \tag{100}$$

$$-i\omega\bar{\phi} + ik\bar{u} + \frac{d\bar{v}}{dy} = 0 \tag{101}$$

Case a: $v \equiv 0$. *Kelvin Wave.*

If we put $v = 0$ in equations (95) - (97) then the solution for u and ϕ is:

$$u = \pm\phi = F(x \mp t)e^{\mp\frac{y^2}{2}} \tag{102}$$

where F is an arbitrary function. To ensure bounded solutions for large values of y we choose the solution with the decaying exponential in y. The corresponding normal mode solution is:

$$u = \phi = \bar{u}e^{ik(x-t)} = e^{-\frac{y^2}{2}}e^{ik(x-t)} \tag{103}$$

together with the dispersion relation:

$$\omega = k \tag{104}$$

(figure 6).

Case b: $v \not\equiv 0$. *Rossby, Inertia-Gravity and Yanai Waves.*

In this case we can eliminate $\bar{u}$ and $\bar{\phi}$ to obtain a single equation for $\bar{v}$:

$$\frac{d^2\bar{v}}{dy^2} + (\omega^2 - k^2 - \frac{k}{\omega} - y^2)\bar{v} = 0 \tag{105}$$

The solution must be bounded in y: $\bar{v} \to 0$ as $y \to \pm\infty$. This boundary condition gives the constraint that the quantity $\omega^2 - k^2 - \frac{k}{\omega}$ must be an odd integer:

$$\omega^2 - k^2 - \frac{k}{\omega} = (2n+1), \quad n = 0, 1, 2, \ldots \tag{106}$$

Regarding this as a quadratic equation in k, we can solve for k in terms of ω. Both of the roots lead to physically admissable solutions: One root gives a high frequency class of solutions known as inertia-gravity waves with modes $n = 1, 2, 3, \ldots$. The other root gives the low frequency Rossby wave solutions with modes $n = 1, 2, 3, \ldots$. The $n = 0$ mode corresponds to the Yanai wave (figure 6). The solution to equation (105) for the Yanai wave is:

$$\bar{v} = \frac{1}{\sqrt{2^n n! \sqrt{\pi}}} e^{-\frac{1}{2}y^2} H_n(y) \tag{107}$$

where $H_n(y)$ is the n^{th} order Hermite polynomial. The multiplicative parameter in front of this expression is a normalization factor, *i.e.*, if we define:

$$\psi_n = \frac{e^{-\frac{y^2}{2}} H_n(y)}{\sqrt{2^n n! \sqrt{\pi}}} \tag{108}$$

then the ψ_n's satisfy the orthogonality conditions:

$$\int_{-\infty}^{\infty} \psi_n \psi_m dy = \delta_{nm} \tag{109}$$

For the remainder of this section we shall focus on the *Yanai wave.* Putting $n = 0$ in the dispersion relation (106) and solving for k in terms of ω yields two solutions:

$$k = -\omega; \quad k = \omega - \frac{1}{\omega} \tag{110}$$

We reject the solution corresponding to $k = -\omega$ because the u field becomes unbounded for large y. Equations (107) and (110) then give the solution for v:

$$v(x, y, t) = \psi_0(y) e^{i(\omega - \frac{1}{\omega})x - i\omega t} \tag{111}$$

Substituting the corresponding solution for $\bar{v}$ into equations (99) – (101) and using the recurrence relations for Hermite polynomials we obtain the solutions for u and ϕ:

$$u = \phi = \frac{i\omega}{\sqrt{2}} \psi_1(y) e^{i(\omega - \frac{1}{\omega})x - i\omega t} \tag{112}$$

where the appropriate functions ψ_n are given by:

$$\psi_0 = \frac{e^{-\frac{y^2}{2}}}{\pi^{\frac{1}{4}}}; \quad \psi_1 = \frac{\sqrt{2} y e^{-\frac{y^2}{2}}}{\pi^{\frac{1}{4}}} \tag{113}$$

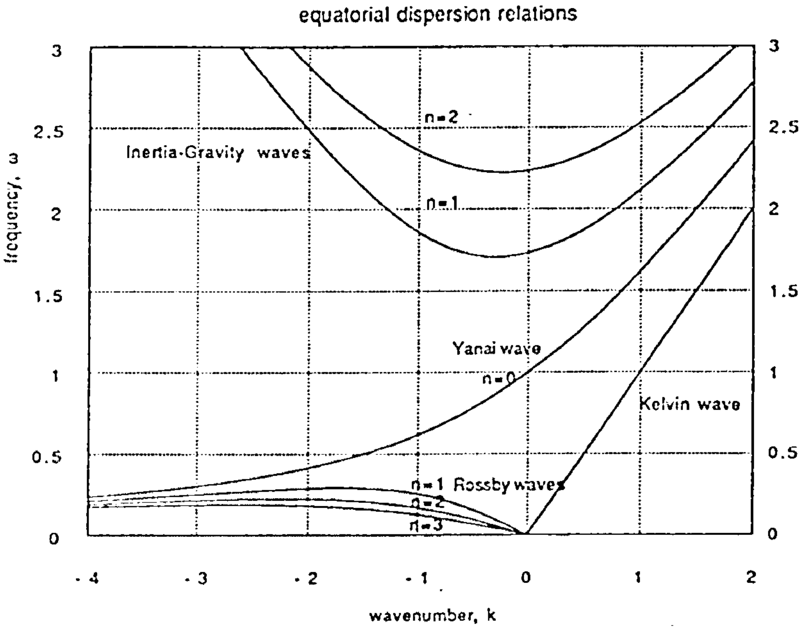

Figure 6: Dispersion diagram for linear equatorial free waves.

The wavenumber k and frequency ω have been non-dimensionalized by units of $\sqrt{\frac{\beta}{c}}$ and $\sqrt{\beta c}$ respectively.

We shall use these solutions later on to illustrate the structure of Yanai wave packets and compare them with the results from our numerical model. As can be seen from the dispersion diagram (figure 6) the group velocity is always towards the east (the slope of the curve is always positive) whereas the phase velocity can be either eastwards (positive k) or westwards (negative k) depending on the size of the frequency. In fact the phase and group velocities, c_p and c_g respectively, are quite easily computed:

$$c_p = \frac{\omega^2}{\omega^2 - 1} \tag{114}$$

$$c_g = \frac{\omega^2}{\omega^2 + 1} \tag{115}$$

The latitudinal structure of the u and ϕ fields for the Yanai wave are identical (equation (112)). They are anti-symmetric about the equator and have extrema points exactly one Rossby deformation radius distant north and south of the equator (figure 7). The v field is symmetric and has a maximum value on the equator. Later, we shall exploit the anti-symmetry property of the ϕ field in order to isolate the h anomalies in our model solutions from the Kelvin waves which are symmetric about the equator (equation (103)).

5.2 Choice of Model Parameters

A list of parameter choices for our model is given in table (1). They are the same for all the experiments to be described unless otherwise stated. The values $h_0 = 200\ m$ and $g' = .03\ m\,s^{-2}$ giving a phase speed of $c = 2.45\ m\,s^{-1}$ are reasonable choices for the Indian Ocean and have been used, *e.g.*, in the numerical model of Woodberry *et al.* (1989) [64]. Applying these scales to the non-dimensional dispersion relations of the previous section,

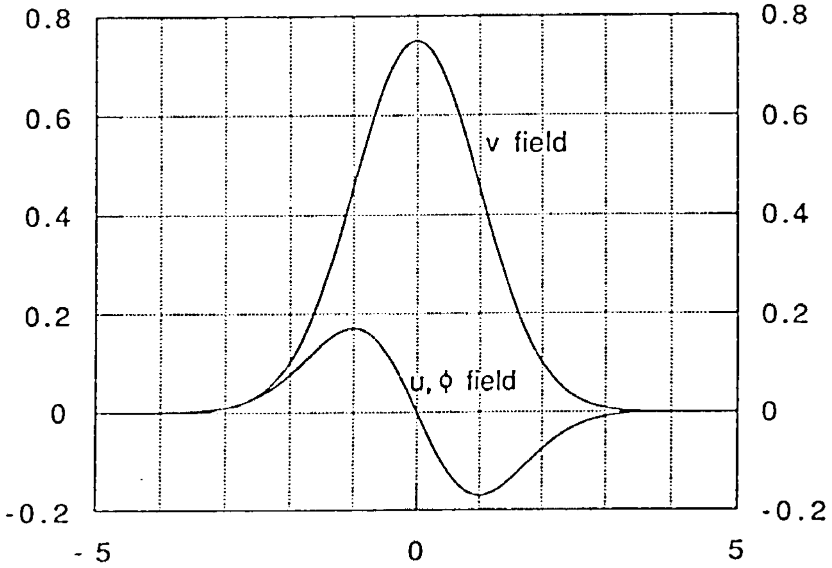

Figure 7: The non-dimensional u, v and ϕ latitudinal profiles for the Yanai wave. Each unit of length on the horizontal axis is equivalent to 1 Rossby deformation radius.
The maximum value for the v field occurs on the equator and at one deformation radius from the equator for the u and ϕ fields. All three fields decay in the poleward directions in accordance with the imposed boundary conditions.

parameter	description	value
β	Coriolis parameter	$2.28 \times 10^{-11}\ m^{-1}\ s^{-1}$
A	eddy viscosity	$750\ m^2\ s^{-1}$
Δt	time step	$1800\ s$
h_0	initial upper-layer thickness	$200\ m$
g'	reduced-gravity	$.03\ m\, s^{-2}$
c	phase speed	$2.45\ m\, s^{-1}$
T	time scale $= \frac{1}{\sqrt{c\beta}}$	1.55 days
L	Rossby deformation radius	$327.75\ km$
$N+1$	Chebyshev modes in x	73
$M+1$	Chebyshev modes in y	37
L_x	length of domain in x	$15,000\ km$
L_y	length of domain in y	$3,000\ km$

Table 1: List of various model parameters used in the model. These are the values used in all of the experiments performed unless otherwise specified.

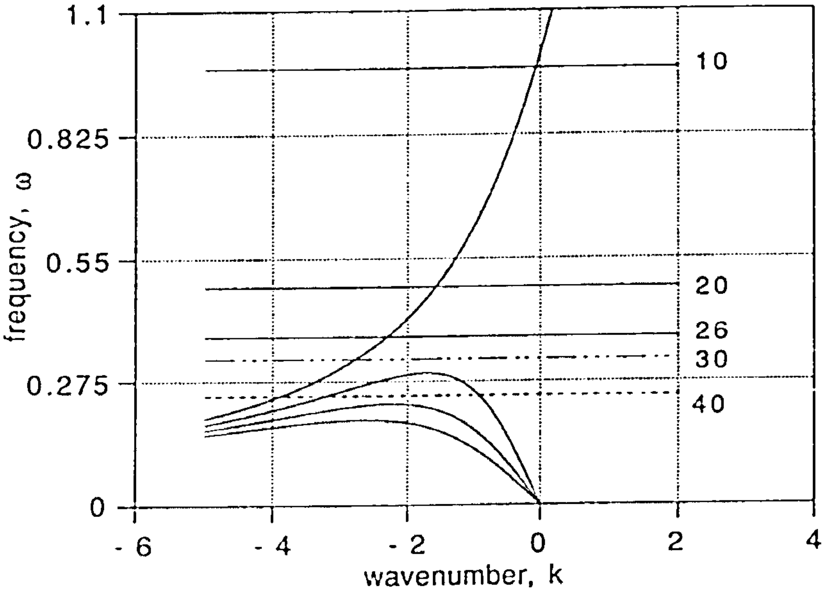

Figure 8: Dispersion curves for Yanai and Rossby waves.The horizontal lines indicate the locations of periods for 10, 20, 26, 30 and 40 days.
Note that only the 40-day period gives rise to both Rossby and Yanai waves; *i.e.* , short Rossby waves propagating energy eastwards may be excited at this period from a western boundary, but not at the 30-day period or less.

we see that for the period set of 10, 20, 26 and 30 days only the Yanai and Kelvin waves are available whereas at 40 days both short and long Rossby waves may be excited in addition to these waves (figure 8). The Yanai wave becomes infinitely long as $k \rightarrow 0^-$ (*i.e.* as the period approaches 9.73 days). As k becomes positive the phase speed of the Yanai wave is eastward, *i.e.*, in the same direction as its group speed. But this occurs at periods which are too short for our interest. We focus our attention on waves with periods greater than about 13 days which implies the wavelengths are less than 3,500 km approximately (figure 9a). The group velocity increases with increasing frequency and therefore decreases with increasing period (figure 9b). It is interesting to note the *rate* at which the group velocity increases with decreasing period: *e.g.*, it doubles in size from 25 to 50 $cm\,s^{-1}$ in going from 30 to 20 days and more than doubles in going from 20 to 10 days. This implies there will be a significant separation in time between waves of different wavelengths and this fact turns out to be a very important one for the experiments we shall describe.

Yanai waves in the 20- to 30-day period range have been observed and modelled in the equatorial regions of all the oceans as we have already discussed in the previous chapter. The particular value of this peak in the period varies slightly between the different oceans as a result of the different stratifications. In the Indian Ocean the peak is observed to be about 26 days (Reverdin and Luyten (1986) [51]). The 26-day wave has a wavelength of 896 km with the particular set of parameter values we have selected for our model. Contour plots of the u, v and h fields for this wave calculated from the analytical solutions (equations (111) and (112)) are shown in figure (10) with the domain size we shall use for the experiments to be described in the next section.

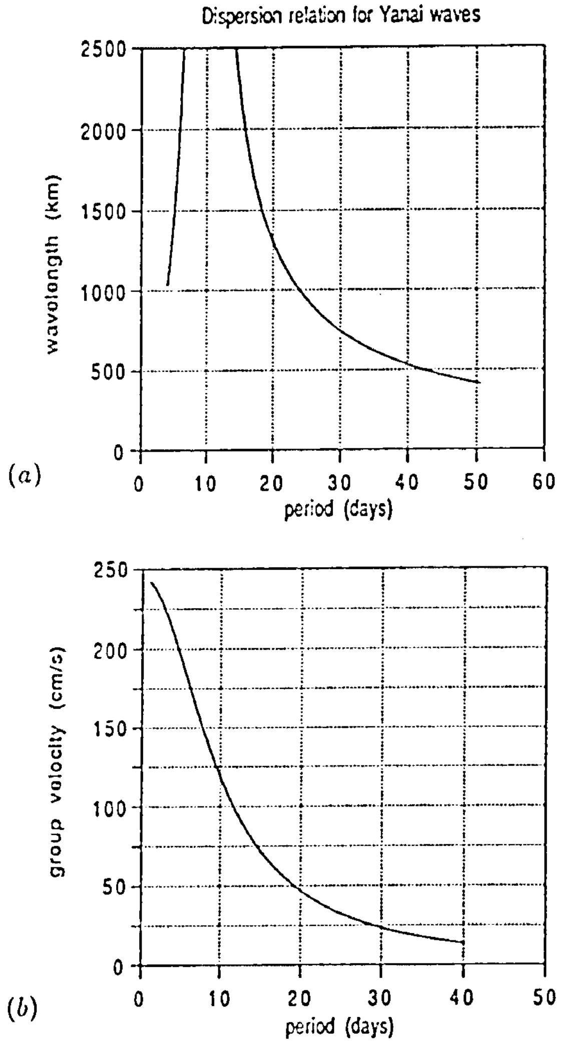

Figure 9: (a): The dispersion curve for the Yanai waves with wavelength plotted vs. the period in days. The 25-day period wave has a wavelength of 945 km approximately. (b): The group velocity as a function of the period for Yanai waves. Note that the group velocity doubles (from 25 to 50 $cm\,s^{-1}$ approximately) when the period changes from 30 to 20 days.

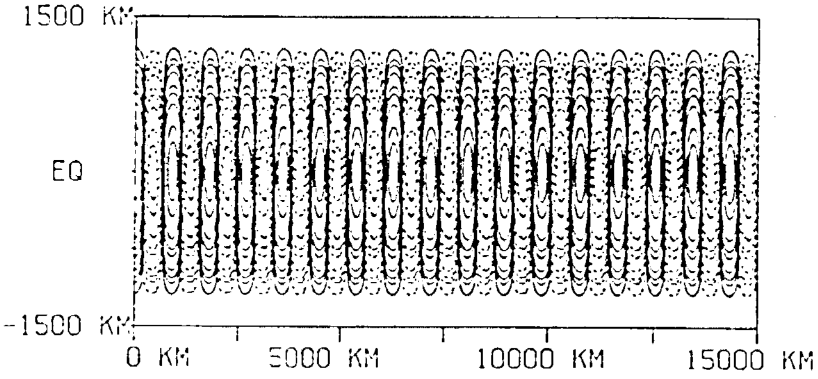

(*a*)

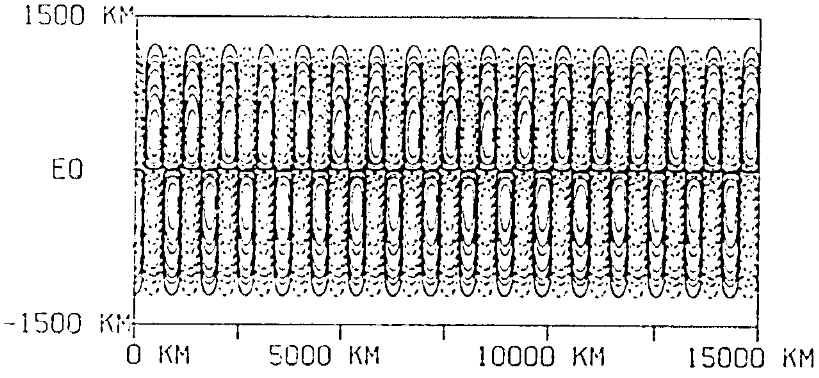

(*b*)

Figure 10: (a): Contours of the v field for the 26-day period Yanai wave over the same domain size as used in the numerical experiments. (Contours are non-dimensional and dashed contours indicate negative values). (b): As in (a), but for the u and h fields.

5.3 Numerical Experiments

We describe a sequence of model simulations generating Yanai waves by applying a wind stress forcing. For all but one of these simulations the wind stress is adjacent to the western boundary of the domain. The purpose of our experiments is to address the following questions:

1. Can a simple cross-equatorial wind stress generate Yanai wave patterns similar to those found in the numerical modelling results of, for example, Kindle and Thompson (1989) [32] ?
2. What effect does the angle of the western boundary have on the Yanai waves generated from such a simple wind stress pattern at this boundary ?
3. Does the area of the wind forcing region influence the wavelength selected for these waves and is this related in any way to the Rossby deformation radius ?
4. Can these waves be generated by a similar wind stress forcing in the interior of the domain?
5. What is the mechanism by which Yanai waves of a specific period around 25 days are generated ?

For all the simulations we use a wind stress profile of the form:

$$\begin{aligned} \tau_{x'}(x', y') &= 0 \\ \tau_{y'}(x', y') &= \frac{\tau_0}{2}(1 + tanh[\frac{(x_l - x')}{s}]) \qquad (116) \end{aligned}$$

with $\tau_0 = 5 \times 10^{-2}\ N\,m^{-2}$ and $s = 300\ km$ (figure 11). The variables x' and y' specify the direction normal to and along the western boundary, respectively, so that the wind is everywhere parallel to this boundary ($\tau_{x'} = 0$). The parameter x_l is a measure of the width of the wind stress region which is varied amongst the different experiments. We use a damping function, $d(x)$, to absorb the waves propagating towards the eastern boundary (as in, *e.g.*, Moore and McCreary (1990) [41]). This function is continuous and is effectively zero over most of the domain apart from a narrow region close to the eastern boundary:

$$d(x) = A tanh(\frac{S}{A}[x - x_0]) \tag{117}$$

where $A = 10^{-4}\ s^{-1}$, $S = 1.6 \times 10^{-10}\ m^{-1}\,s^{-1}$ and $x_0 = L_x - 5 \times 10^5\ m$ (figure 12). The damping effect is applied as an extra linear term to the right hand side of the model equations (equations (54) - (56)) so that we solve:

$$\mathcal{L}[\psi] = R(x, y, t) - d(x)\psi \tag{118}$$

where ψ represents either u, v or $h - h_0$. $\mathcal{L} \equiv \frac{\partial}{\partial t} + u\frac{\partial}{\partial x} + v\frac{\partial}{\partial y}$ and $R(x, y, t)$ contains the remaining "right-hand-side" terms.

EXPERIMENT 1: Indian Ocean model simulation.

The western boundary of our model domain is a polynomial approximation to the east African coast from 10°S to 10°N, similar to that of figure (5a). The wind stress profile is that of figure (11), with a width of 1000 km, turned on at $t = 0$, and everywhere parallel to the coast. Both Yanai and Kelvin waves are generated because the wind stress has a component meridionally and zonally. (On a rectangular domain a purely meridional wind

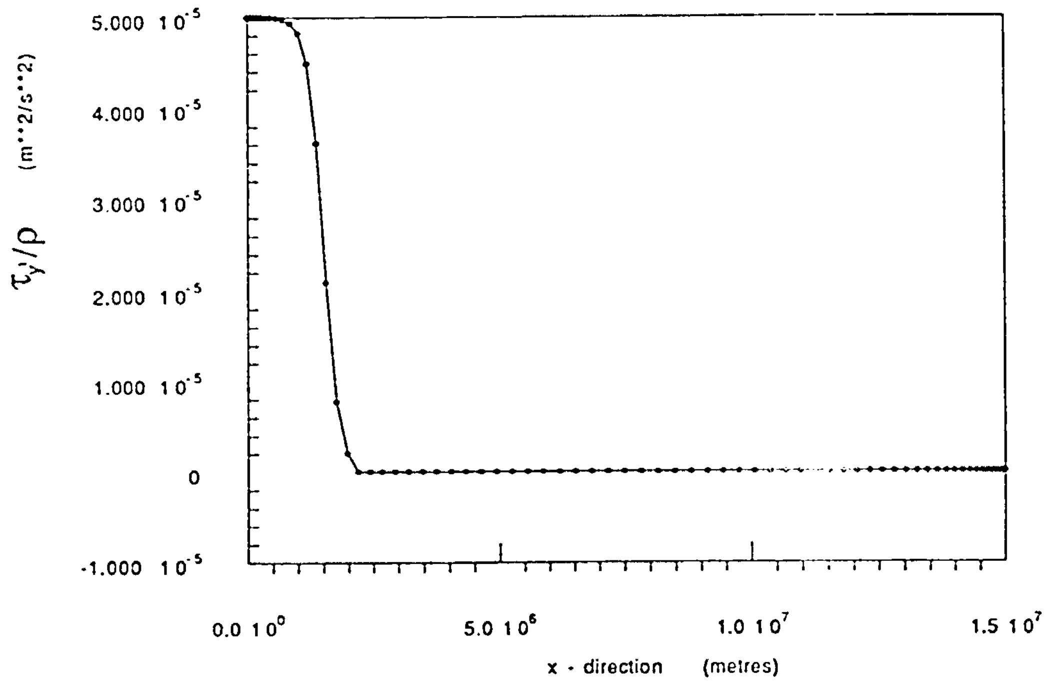

Figure 11: The wind stress profile used in subsequent numerical experiments. Here the "x'– direction" refers to the direction normal to the western boundary and y' is along this boundary. ($\rho = 1000\ kg\,m^{-3}$)

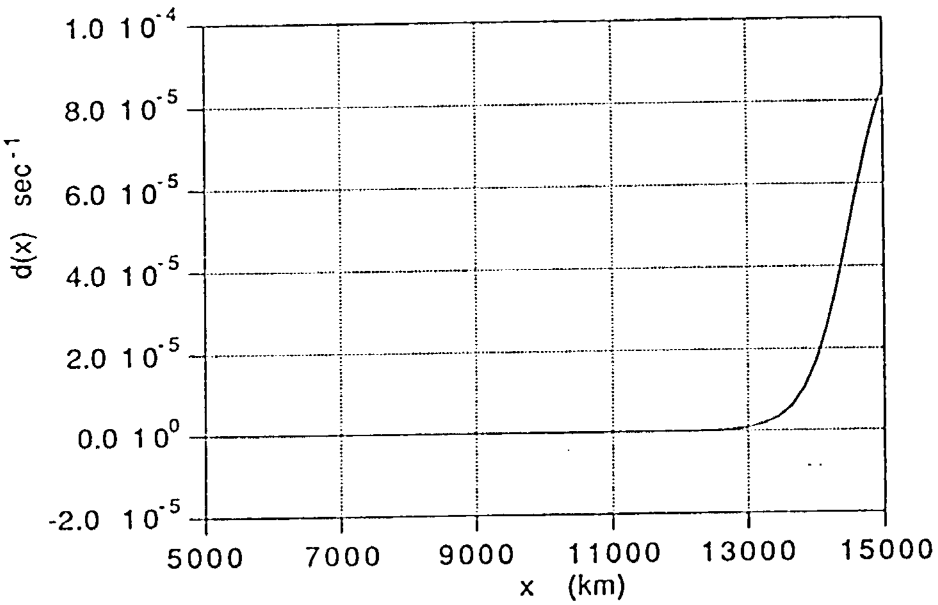

Figure 12: The damping function used to absorb the waves approaching the eastern boundary. Effectively there is an open boundary on this side of the domain.

stress generates a Yanai wave whereas a purely zonal wind stress generates a Kelvin wave, as has been demonstrated by Moore and McCreary (1990) [41]). The (dispersive) Yanai waves have eastward group speeds in the range 12 - 80 $cm\,s^{-1}$ and westward phase speeds in the range 15 - 75 $cm\,s^{-1}$. A sequence of "snap-shot" pictures of the meridional velocity field from the model simulation at days 20, 48 and 76 show a packet of Yanai waves emanating from the western boundary region propagating energy eastward at the group velocity (figure 13). The Kelvin wave is not seen because it has zero meridional velocity. (NOTE: The boundaries of the domains in our model experiments are always smooth curves even though the figures show jagged lines on the western boundaries. This is merely due to the way in which we transformed the model solution from the computational domain to the physical domain.) There is an increase in the wavelength of the Yanai waves eastwards across the basin because of the dispersive properties of these waves: The waves with the higher group velocity have longer wavelengths (figure 8) and in time separate out from the shorter waves which remain closer to the western boundary. The longer waves have shorter periods (figure 9a) and so there is a decrease in period from west to east. But the decrease in period is not a linear one as group velocity does not vary linearly with period (figure 9b). As we shall see later, this fact gives rise to a preferred period selection in the interior of the domain, with the very long period waves remaining close to the western boundary and the short period waves disappearing eastwards out of the domain. For a comparison we show the results of a simulation of the Indian Ocean by Kindle and Thompson (1989) [32]. The model was driven by the Hellerman and Rosenstein monthly wind stress (Hellerman and Rosenstein (1983) [27]). Figure (14) shows three "snap-shots" of the meridional velocity

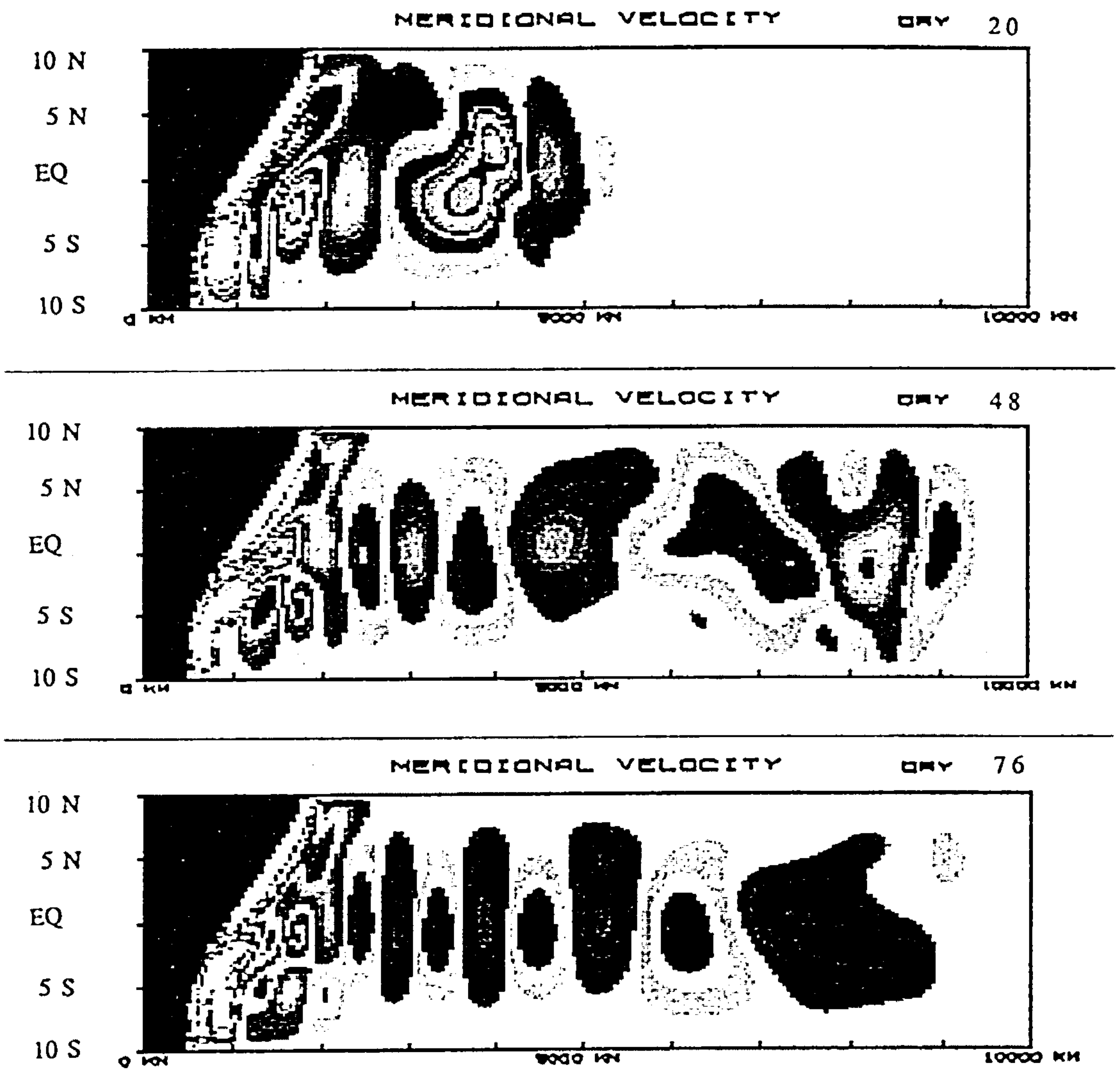

Figure 13: Spectral model simulation on the Indian Ocean domain from 10^{0}S to 10^{0}N. The wind stress is everywhere parallel to the coast extending a distance of 1000 km from it and switched on immediately at $t = 0$. The figure shows three snap-shots of the meridional velocity field at days 20, 48 and 76. A packet of Yanai waves is generated propagating energy eastwards from the western boundary. Note the increase in wavelength from west to east.

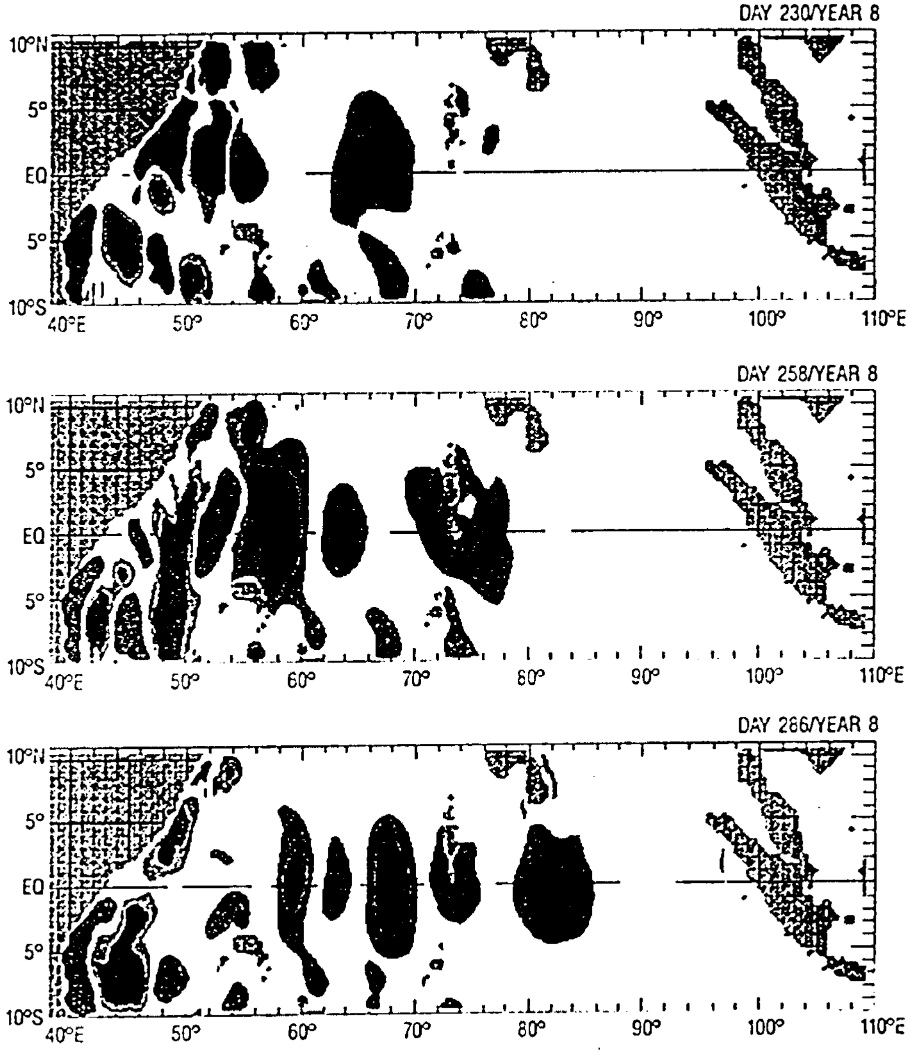

Figure 14: Indian Ocean model simulation using the monthly climatological winds of Hellerman and Rosenstein (from Kindle and Thompson (1989)). The figure is a sequence of snap-shots of meridional velocity contours for days 230, 258 and 286 of the 8^{th} year of integration, showing a packet of Yanai waves propagating from the west. A similar increase in wavelength occurs in going from west to east, as in our model solution.

contours at days 230, 258 and 286 of the 8^{th} year of integration. A packet of Yanai waves is seen to propagate energy eastwards from the western boundary region, with wavelength increasing eastwards. Comparing, for example, this wave packet from 60°E to 85°E on day 286 with our model solution from 3000 km to 5,500 km we see that the train of Yanai waves generated are similar (allowing for the difference in domain size). There are more frequencies available in the wind stress we chose for our model and consequently more waves seen in the wave packet of our simulation. The large wavelengths leading the wave packet are due to the impulsive turn-on of the wind. Nevertheless, by day 76 the emergence of wavelengths around 1000 km west of the 5000 km mark is becoming clear.

The question arises as to how well do the Yanai waves in our model couple with the wind frequencies. We used a "ramp" type wind forcing by turning on the wind stress to its constant maximum value impulsively at $t = 0$. Theoretically, therefore, all frequencies are available from the forcing. But we do not obtain wavelengths longer than a few thousand kilometres. The reason for this is due to the power spectra of the wind. For example, let us simplify the wind stress profile to a "ramp" function of height b and length T:

$$\tau_y(t) = \begin{cases} b & 0 \leq t \leq T \\ 0 & \text{otherwise} \end{cases} \tag{119}$$

Expanding this function in a Fourier series of the form:

$$\tau_y(t) = \sum_{n=0}^{\infty} a_n \cos(\frac{n\pi t}{T}) + \sum_{n=1}^{\infty} b_n \sin(\frac{n\pi t}{T}) \tag{120}$$

we obtain the coefficients:

$$a_0 = \frac{b}{2}$$

$$a_n = 0$$
$$b_n = \begin{cases} \frac{2b}{n\pi} & n = 1,3,5,\ldots \\ 0 & n = 2,4,6,\ldots \end{cases} \tag{121}$$

Since the coefficients (other than a_0) are at most $O(\frac{1}{n})$ this implies that the power at frequency n is at most $O(\frac{1}{n^2})$. Hence there is little power input to the higher frequency, longer wavelength waves with this type of ramp wind stress and similarly with the wind stress profile we have used in this experiment. In order to clarify this further, we present results from two model simulations with meridional wind forcing at 10 and 13 days on a rectangular domain to show that extremely long Yanai waves can be generated by high frequency winds. The theoretical wavelengths for these waves are 37,688 km and 3,505 km respectively. The wind patch size is 1000 km and the height field anomalies after 299 days are shown in figure (15). The longer wave is too long for the domain and is absorbed by the sponge layer, but the results are in good agreement with the theoretical values. We conclude that the Yanai waves couple very well with the frequencies in the wind forcing and that the preferential wavelength selection of around 1000 km is not directly associated with the Rossby deformation radius. In addition, examining the time scale and the length scale (= Rossby deformation radius) given in equation (94) it is clearly possibly to alter the time scale keeping the deformation radius fixed by altering the values of β and c appropriately. Such a change in the time scale can produce any desired change in the wavelength of the wave at the same frequency because the dispersion curve is changed.

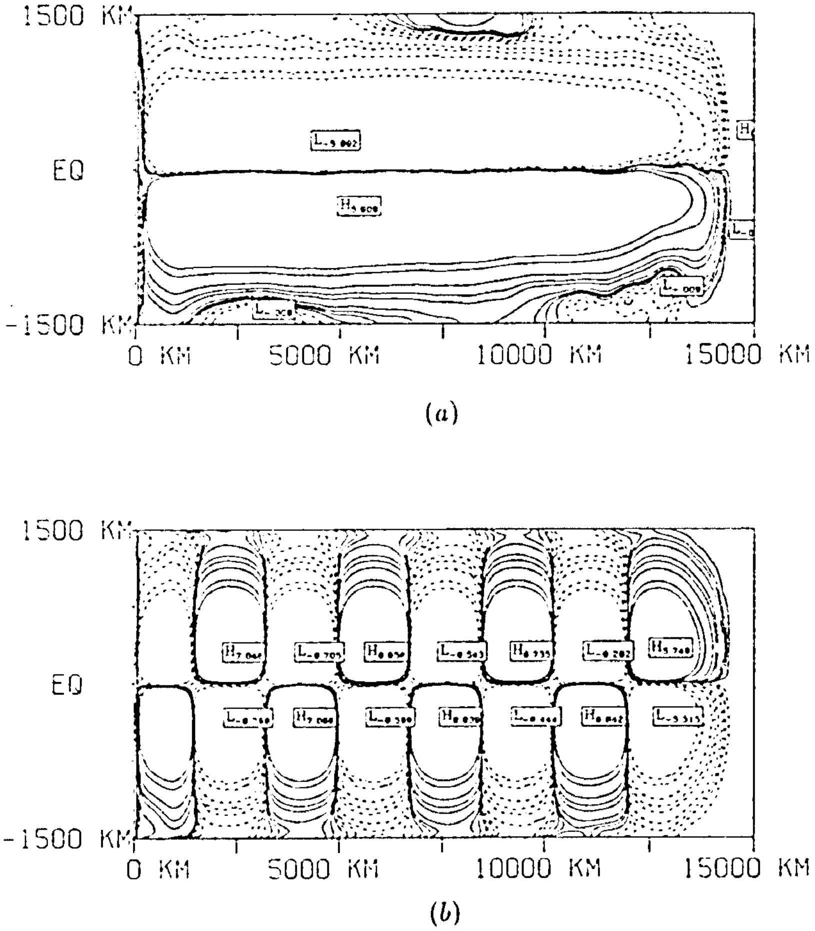

Figure 15: (a): The height field anomaly after 299 days with a purely meridional wind patch oscillating with period 10 days at the western boundary. The wind patch size is 1000 *km* and the theoretical wavelength is 37,688 *km*. The wave is too long for the domain and is absorbed by the sponge layer. (Contours are in metres, with solid contours indicating positive values and dashed contours indicating negative values). (b): As in (a) except that the forcing period is 13 days. The theoretical wavelength is 3,505 *km* and the simulation is in good agreement with this.

EXPERIMENT 2: Dependence of solution on wind patch size.

We begin by using the analytical solution for the height field (equation (112)) to generate a "synthetic" wave packet similar to that produced by our model simulations. The purpose of this is to illustrate more clearly the structure of the model solutions and to use it as a comparison between some of them. Consider a rectangular domain (as we had in figure (15)) and a purely meridional wind stress at the western boundary with a profile as in figure (11) of width 1000 km. The wind is switched on immediately at $t = 0$ and the solution for the height field anomaly after 100 days is shown in figure (16b). Because of the impulsive turn-on of the wind the ocean "feels" the higher frequency components of the forcing first and then in time responds more to the lower frequencies. If the time period is long enough (~ 400 days) the ocean eventually adjusts to a balance between the height field and the wind stress. In other words, the ocean is tending towards responding to zero frequency and the waves are extremely short, have negligible group velocity and have been damped by friction so much so that they are not seen anymore. We generate a wave packet to mimic this scenario crudely from the (non-dimensional) solution for the height field (equation (112)) by superposing 20 frequencies together equally distributed from (non-dimensional) frequency .3 (corresponding to a dimensional wavelength of 679 km) to .9 (corresponding to a dimensional wavelength of 9,755 km). Each separate wave is enveloped by a Gaussian amplitude function with a standard deviation equal to $\frac{1}{8}^{th}$ of the wavelength of that particular wave and moves eastward in time with it's group velocity. This enables a simulation of the initial "burst" of long waves propagating away from the source and having no influence on the shorter waves appearing later. The situation at 100 days is

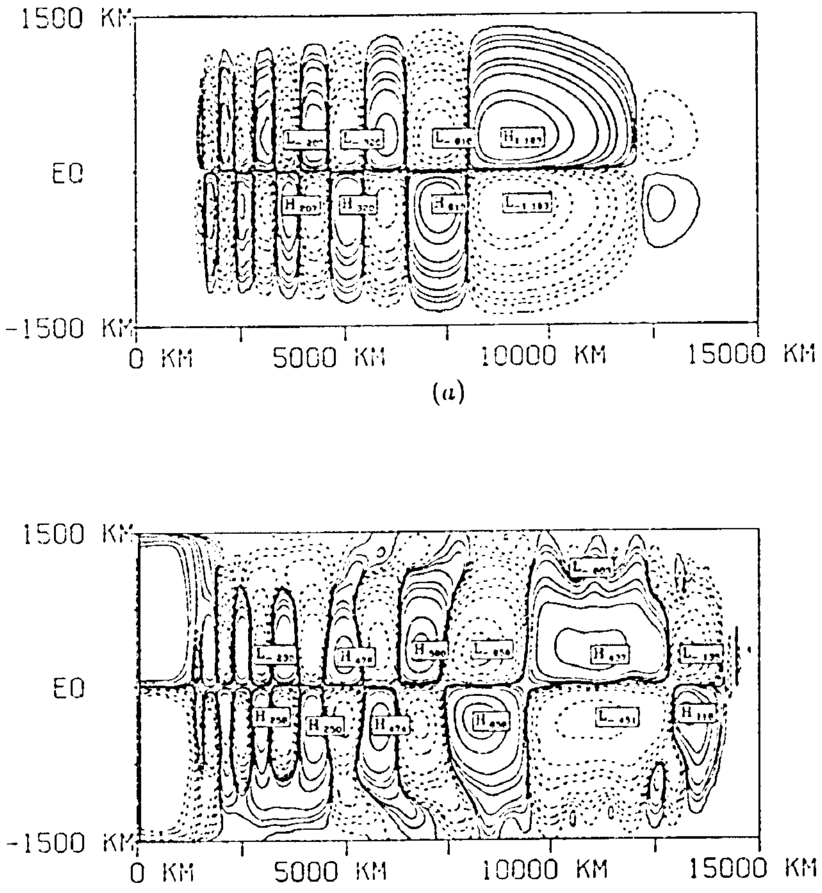

(*a*)

(*b*)

Figure 16: (a):A synthetic wave packet of Yanai waves generated by superposing 20 frequencies of the (non-dimensional) analytical height solution. Each individual wave is enveloped by a Gaussian amplitude function with a standard deviation equal to $\frac{1}{8}^{th}$ of the wavelength and moving with the group velocity of that wave. (Contours are non-dimensional). (b): Model solution on a rectangular domain after 100 days. The wind patch size is 1000 km. ($\tau_r \equiv 0$). Note the similarity in wavelength selection with (a). (Contours are in metres).

shown in figure (16a) and compares well with the model solution in (b). The numerical simulation does exhibit a little distortion particularly closer to the northern and southern boundaries. Distortion was even more pronounced with the Indian Ocean results of the previously described experiment which we attribute to the irregular shape of the western boundary (and consequently the wind stress profile) but nevertheless this really does not effect the wavelengths selected.

Having discussed the generating mechanism and resulting structure of these Yanai wave packets in a simple rectangular domain we now turn our attention to the possible influence that the wind patch size (the present experiment) and the orientation of the western boundary (the next experiment) may have on wavelength selection. We shall use as a standard test experiment the solution on a domain with a sloping western boundary of angle 45°with the eastward direction, a wind patch size of 1000 km and a time period of 100 days. Since we are only interested in the Yanai wave part of the solution we extract the anti-symmetric part of the height field anomaly leaving behind the symmetric Kelvin waves. Let the subscript "top" denote the position of any point in the domain north (south) of the equator and the subscript "bot" denote the corresponding point due south (north) from "top" and the same distance from the equator. Let h_{tot} denote the total height field so that $h = h_{tot} = h_{top}$. Then we can write:

$$h_{tot} = \frac{1}{2}(h_{top} + h_{bot}) + \frac{1}{2}(h_{top} - h_{bot}) \tag{122}$$

The quantity $\frac{1}{2}(h_{top} - h_{bot})$ is the anti-symmetric component of the total height field and $\frac{1}{2}(h_{top} + h_{bot})$ is the symmetric component. The anti-symmetric part of the h field solution to the standard test experiment described above is shown with the synthetic wave packet in figure (17). Although there is slightly more distortion in this solution, the wavelengths appearing are very similar to the synthetic wavelengths and hence to the model solution on the rectangular domain of figure (16b).

The standard test experiment is next compared with what happens when the wind patch size is increased to 2000 *km*. The anti-symmetric height field anomalies of these two model runs reveal little difference after 100 days except that, due to the slightly larger zonal extent between the eastern edge of the wind patch area and the sponge layer in the test experiment, more of the shorter waves in this case are seen (figure (18)). Thus, the size of the wind patch zonal extent does not interfere with the wavelength selection. To reinforce this conclusion we performed a simulation on a rectangular domain with a wind patch size of 280 *km* which is less than the Rossby deformation radius (327.75 *km*). Although the wave amplitudes of the larger wavelengths are small in this case (there is less energy being supplied by the wind) and are distorted by the small-amplitude inertia-gravity waves, the wavelengths themselves compare well with those produced when the wind patch extends for 1000 *km* (figure 19). Again, because of the larger zonal distance in the former case between the forcing region and the sponge layer, more shorter waves are visible.

EXPERIMENT 3: Dependence of solution on coastline geometry.

In our first experiment with the Indian Ocean model domain we noticed a distortion of the initial long waves propagating away from the coastal forcing region but in time the (v field) wave packet in the interior ocean became more symmetric about the equator. As a further

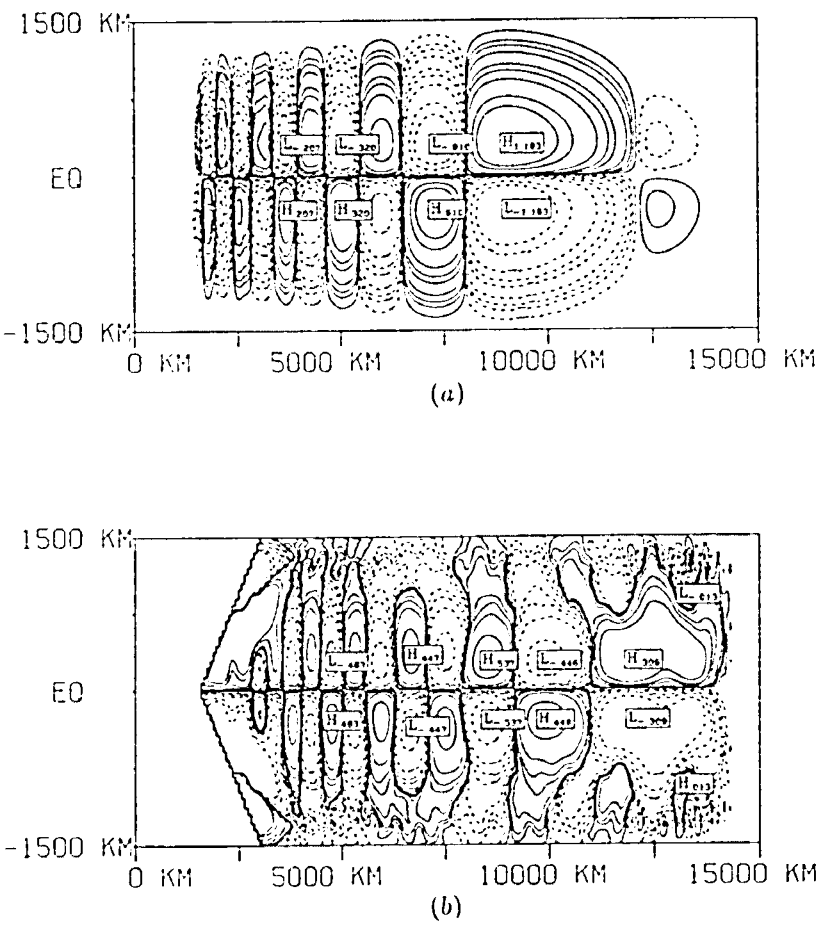

(*a*)

(*b*)

Figure 17: (a): Analytical wave packet as in the previous figure. (b): The anti-symmetric component of the model height field anomaly after 100 days. The physical domain has a sloping western boundary at 45^0. The wind stress is directed northwards everywhere parallel to the coast and has a patch size of 1000 *km*. Note the similarity in wavelengths present with those in (a) (and hence with those of the model solution on the rectangular domain) indicating that the sloping boundary has no effect on this selection. (Contours are in metres).

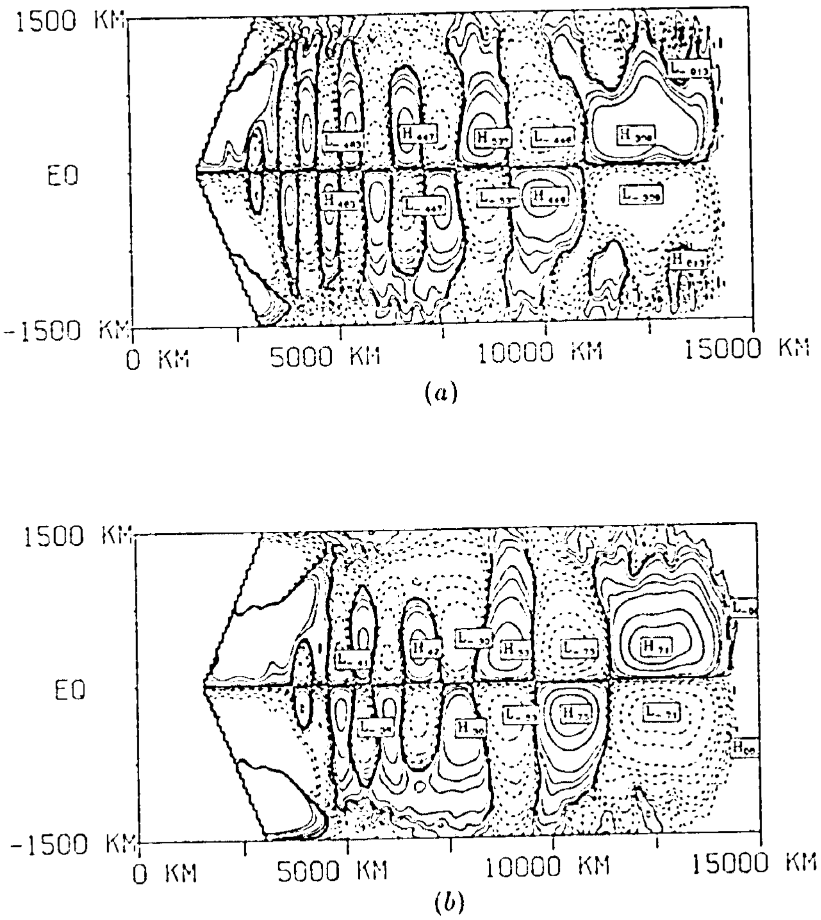

Figure 18: (a): Model solution of the standard test experiment after 100 days as in the previous figure. (b): As in (a) except that the wind patch size has been increased to 2000 *km*. No appreciable change in the wavelengths selected is noticed as can be seen in the similarity of the wave pattern of (a). (Contours are in metres).

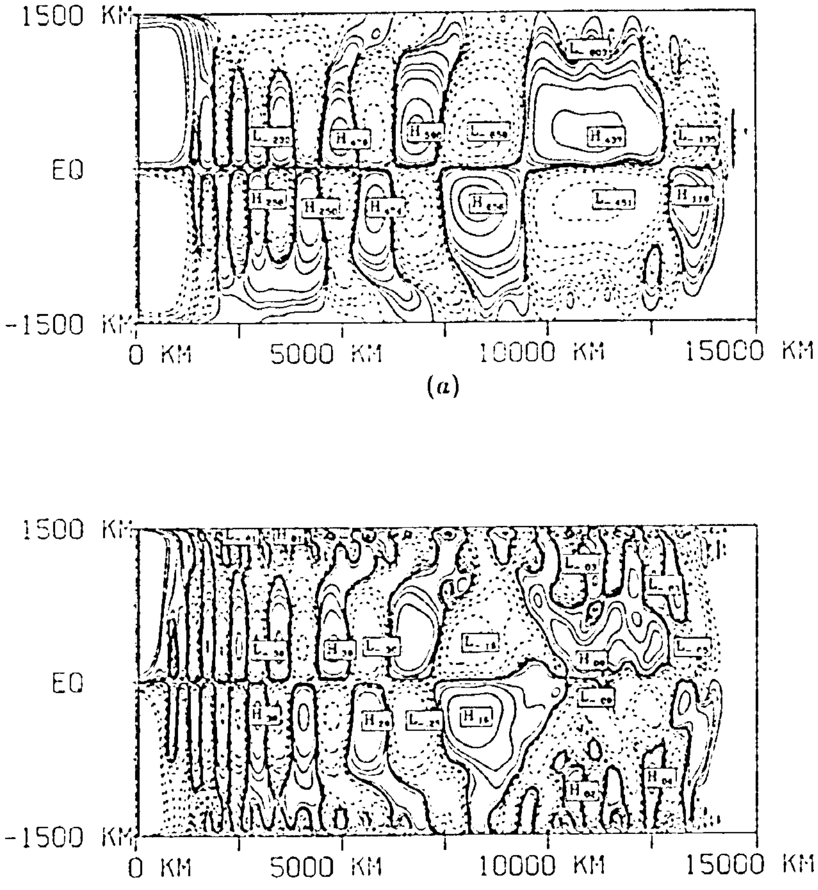

(*a*)

(*b*)

Figure 19: (a): Height field anomaly after 100 days with a wind patch size of 1000 *km* as in figure (16b). (b): Same as in (a) except that the wind patch size has been reduced below the Rossby deformation radius to 280 *km*. Although the waves are weaker and more distorted than in (a), the wavelength selection has not been affected except that more of the short waves are visible near the forcing region. Inertia-gravity waves appear near the boundaries which interfere with the longer wavelengths because of their small amplitudes, causing them to be distorted. (Contours are in metres).

illustration of this distortion due to the coastline geometry we present two solutions for the v field after 50 days; the first is on a rectangular domain and the second has a sloping western boundary at 30°(figure 20). In both cases the wind stress is parallel to the western boundary with a patch size of 1000 km. The longer wavelengths in the irregular domain are distorted and there is no such distortion in the rectangular domain. In time this distortion disappears just as with the Indian Ocean case (experiment 1).

Next we investigate whether the angle of the western boundary has any effect on the wavelengths selected, apart from the distortion. To do this we compare the anti-symmetric component of the height field of the standard test experiment (sloping western boundary at 45°, wind patch size of 1000 km and time period of 100 days) to the same simulation with the boundary sloping at 60°(figure 21) and the boundary sloping at 30°(figure 22). The only essential difference between the three cases is the length of the leading wave group because of the change in zonal extent between the wind forcing region and the sponge layer. For example, the 30°case has the smallest zonal extent and consequently more of the longest wave group has been absorbed by the sponge layer.

As a final experiment to examine the western boundary influence apart from its orientation, we present the result of what happens when the forcing region is in the interior of the domain with no forcing at all near the boundaries. We select a rectangular domain with a meridional forcing of patch size 1000 km exactly as before except that the whole wind patch has been shifted 4000 km eastwards into the interior. (The wind has also been tapered north and south to minimize any effect from the northern and southern boundaries). The model is run for 100 days. This is compared with the case where the wind

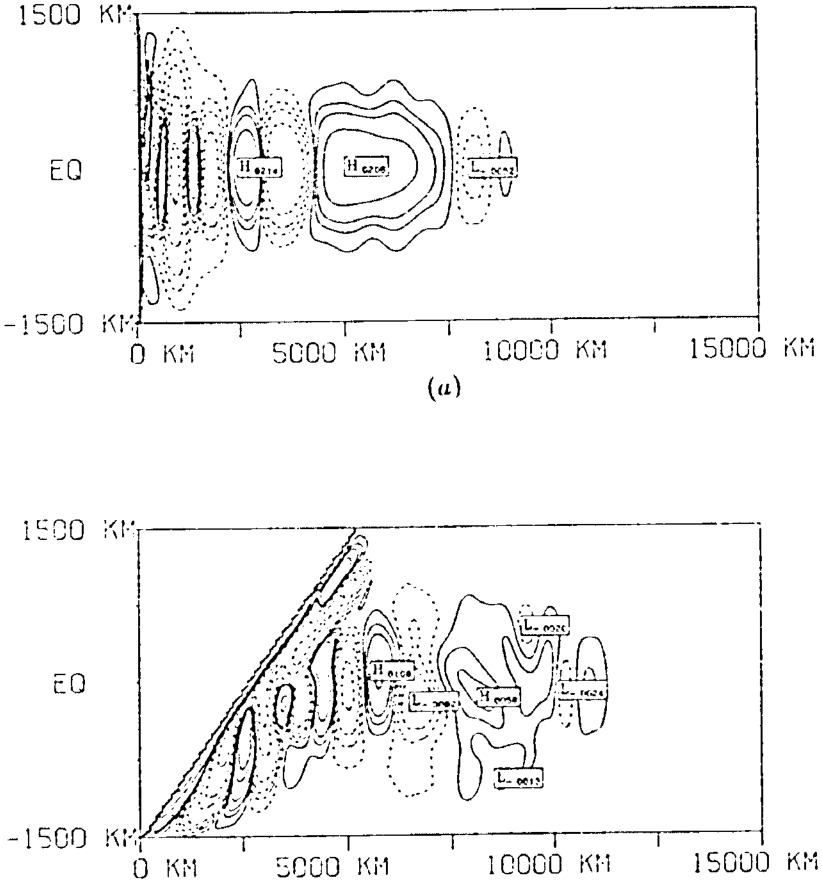

(*a*)

(*b*)

Figure 20: (a): Model v field on a rectangular domain after 50 days. The wind stress is parallel to the western boundary with a patch size of 1000 km. (Contours are in $m s^{-1}$). (b): As in (a) except that the western boundary is sloping at 30^0 to the eastern direction. The wind stress is everywhere parallel to the coast. Note the distortion of the long waves in this case caused by the boundary slope.

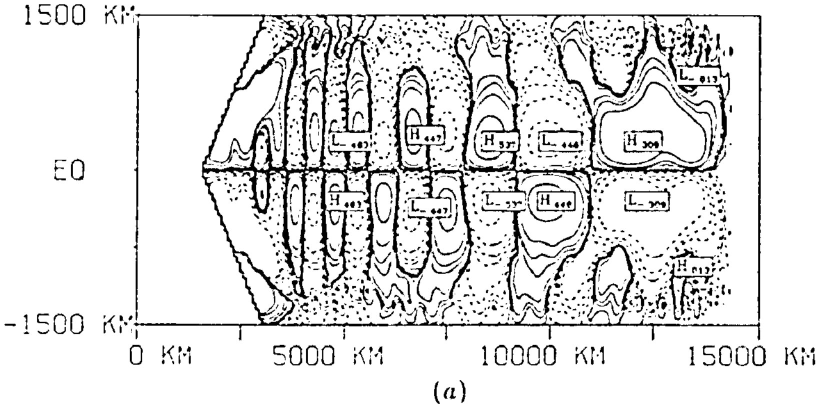

(*a*)

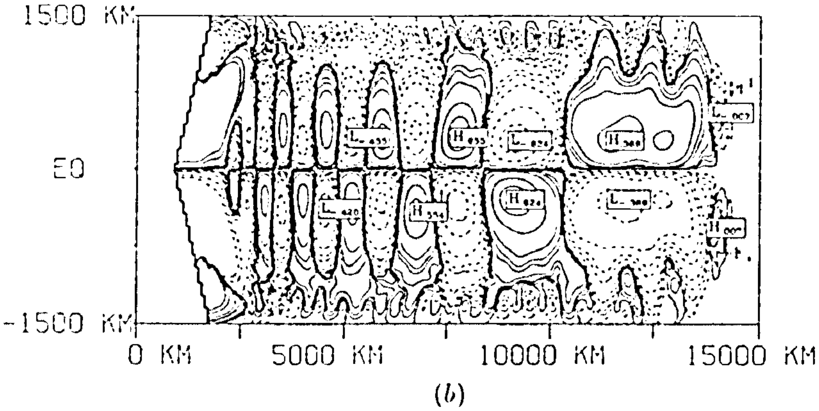

(*b*)

Figure 21: (a): Anti-symmetric height field anomaly of the standard test experiment as in figure (18a). (Contours are in $m s^{-1}$). (b): As in (a) except that the slope of the western boundary has been increased to 60^0. The wavelengths excited are virtually identical in both cases. The longest wave group has been absorbed by the sponge layer more in (a) because of the shorter distance between the forcing region and the eastern boundary (due to the shallower slope of the western boundary).

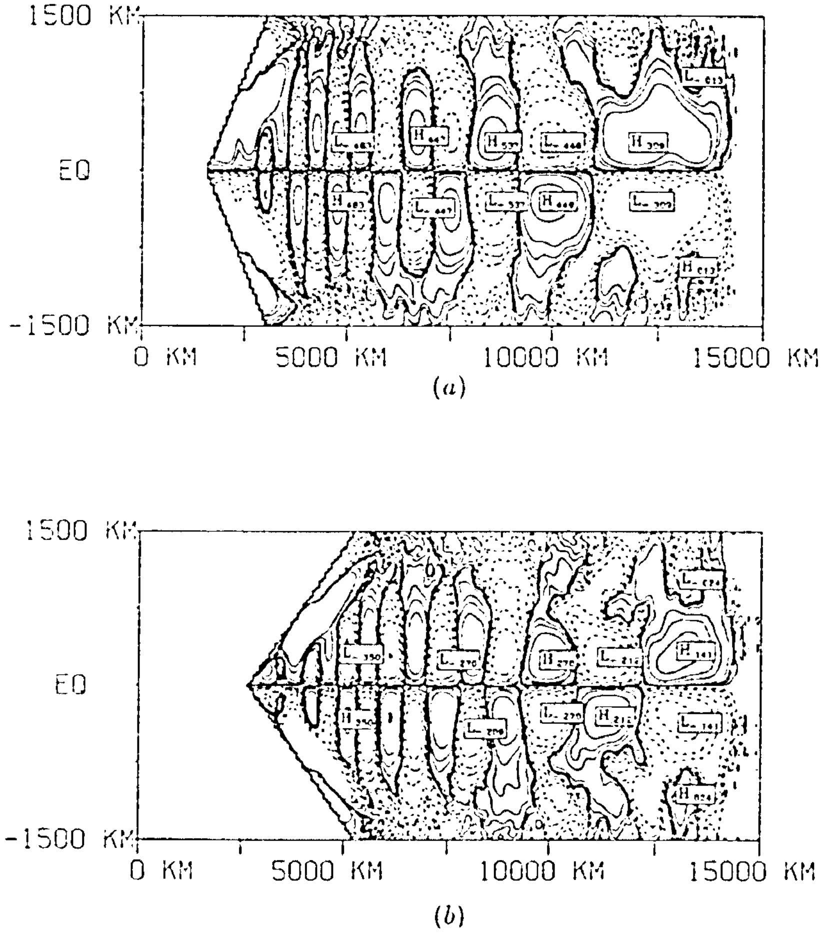

Figure 22: (a): Anti-symmetric height field anomaly of the standard test experiment as in figure (18a). (Contours are in $m\,s^{-1}$). (b): Same as (a) except that the slope of the western boundary has been decreased to 30^0. Again the wavelengths selected are the same apart from the increased distortion and the greater absorption of the leading wave group by the sponge layer.

patch is adjacent to the western boundary (figure 23). The leading wave group with the interior forcing simulation has already been almost completely absorbed by the sponge layer by day 100 but, nevertheless, the remaining wavelengths in the wave packet are similar to the boundary forced case. There is considerably more distortion in the latter case but the wave amplitudes do not seem to have been altered much despite the fact that some of the energy from the forcing goes into generating anti-symmetric Rossby waves which propagate westwards from the eastern edge of the wind patch. This is an interesting result in view of the observations reported by Perigaud (1990) [46] for the Pacific Ocean and which we discussed in chapter 4. According to this study, 30-day instability wave packets both in the western and central Pacific were detected. In other words the waves were observed further to the west than the region of strong latitudinal shear and it is feasible that they could have been generated by a cross-equatorial wind stress in the interior ocean rather than a shear in the mean flow. As we shall see more clearly later on, the Yanai wave packets in our model do, in time, settle down to a period band centred on 25 days once the long waves with the high group speeds, which are a result of the impulsive turn-on of the wind, have disappeared out of the basin through the sponge layer. This may also be an explanation of why Perigaud (1990) [46] discovered a very low correlation between the maximum wave amplitude and the maximum meridional gradient absolute value.

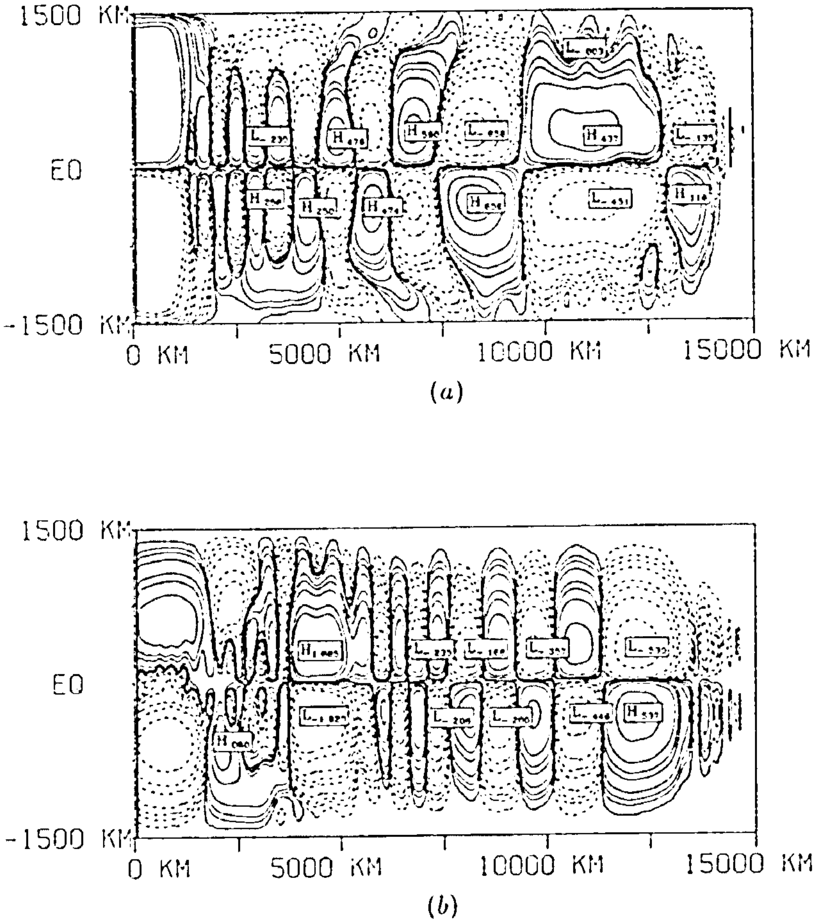

Figure 23: (a):Contours of the model height field anomaly after 100 days. The (meridional) wind forcing is adjacent to the western boundary and has a patch size of 1000 *km*. (Contours are in metres). (b): As in (a) except that the wind has been shifted eastwards to a distance 4000 *km* from the western boundary. The leading wave group has been almost completely damped by the sponge layer but nevertheless the remaining wavelengths are similar to (a). There is an anti-symmetric Rossby wave packet emanating from the eastern side of the forcing region propagating westwards.

5.4 Fourier Analysis

We have described rather qualitatively the generation of Yanai wave packets by cross-equatorial wind forcings in various configurations. In all of the experiments described a similar selection of wavelengths appeared and we indicated that, in time, a narrow band of wavelengths will dominate the interior region of the domain. The particular value of the centre of this narrow band depends on the choice of model parameters (effectively, those parameters which determine the phase speed c) because it can be altered for different stratifications. We now present a more quantitative description of the dynamics described using Fourier analysis (this section) and wavelet analysis (the next section).

We consider the height field anomaly of two of the experiments described in the previous section: The solution on the rectangular domain of figure (16b) and on the domain with sloping western boundary at 45°of figure (17b) (our standard test experiment). In both cases the model was boundary forced and the wind patch size was 1000 km. Figure (24a) shows the (de-meaned) time series for the first case at a position 5, 201 km from the western boundary and 167 km north of the equator. Initially there are high-frequency Yanai waves which are as a result of the impulsive turn-on of the wind and we note a steady growth in amplitude of these waves to a maximum value of about 45 cm. This is in accordance with the decrease in power with increase in frequency as we discussed previously. In time the waves separate out more and the amplitude decays as the ocean tends towards a balance between the height field and the wind stress. The very low-frequency waves have such small group velocity that they never reach the interior ocean before they are damped out

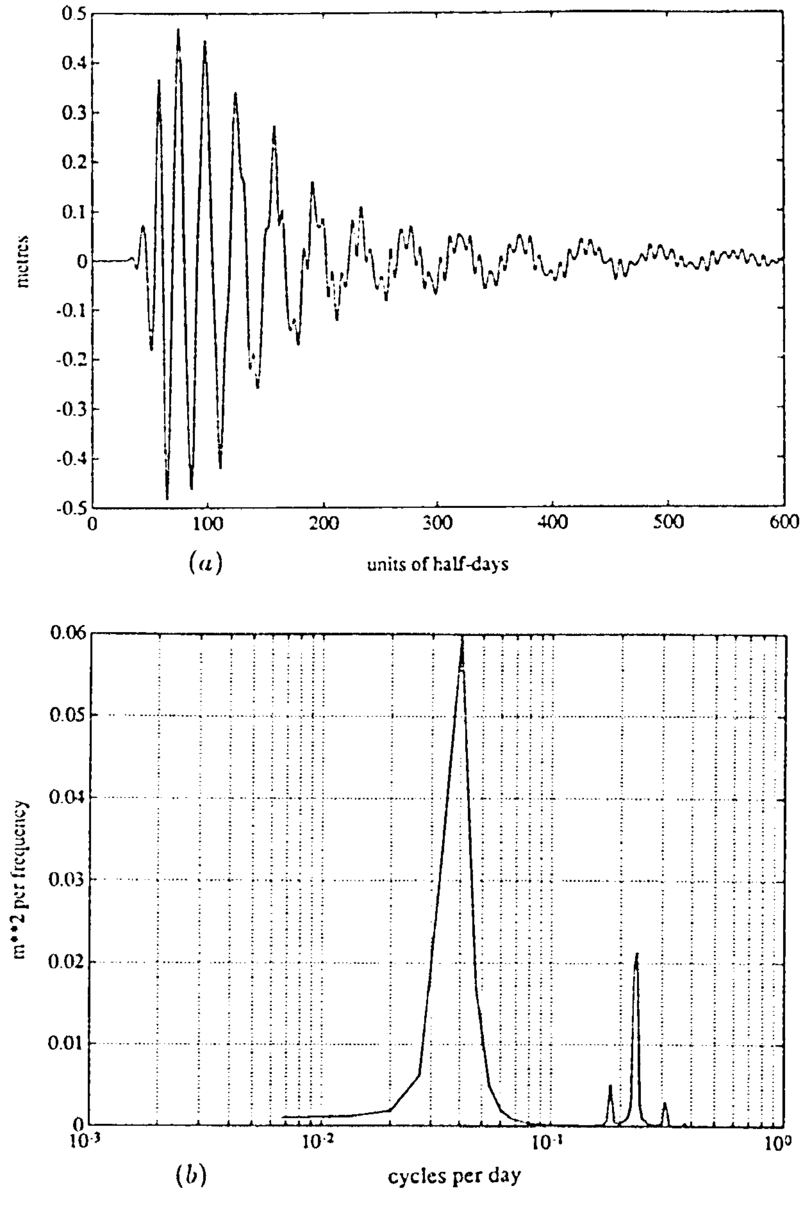

Figure 24: (a): The de-meaned time series of the height field anomaly located at a position 5,201 *km* from the western boundary, 167 *km* north of the equator. The model run is the same as that of figure (16b). The record is at every $\frac{1}{2}$ day for 300 days. Note the appearance of the 25-day waves after the initial burst of high frequency oscillations. (b): The power spectrum of the time series in (a) taken from days 150 to 300, showing a high peak centred on 25 days.

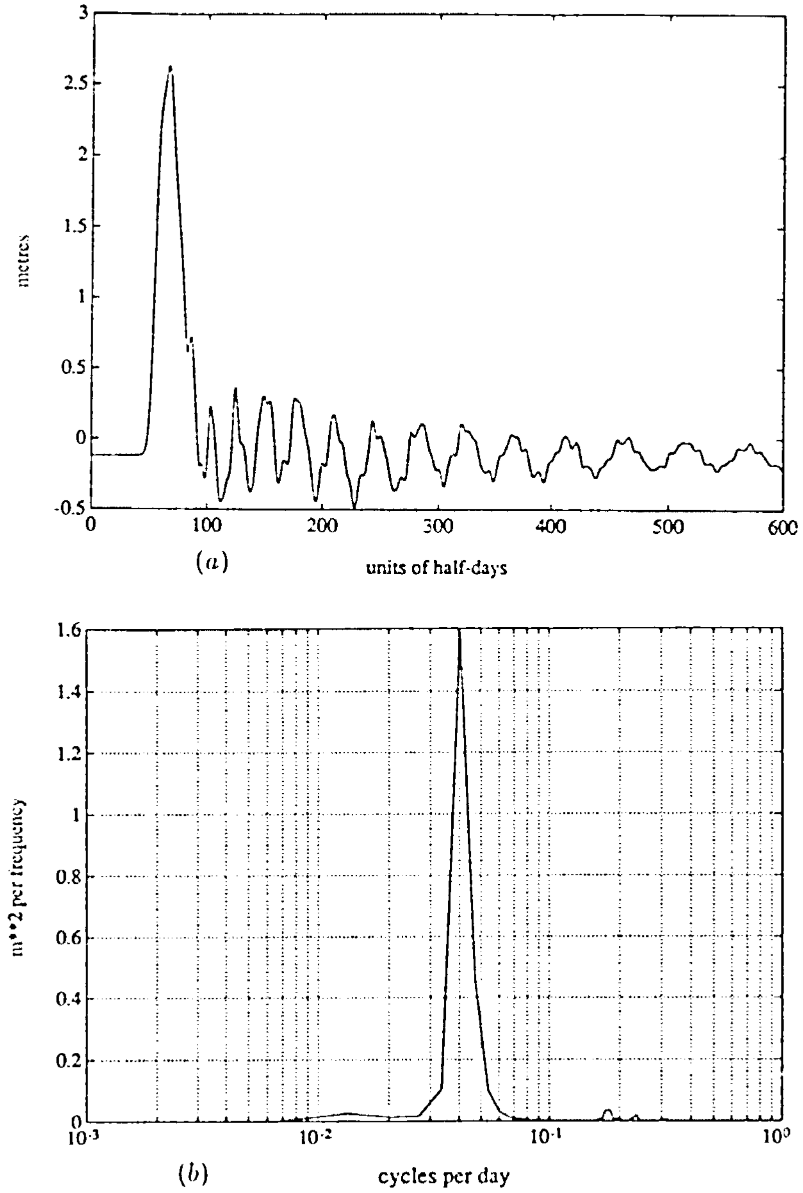

Figure 25: (a): The de-meaned time series of the height field anomaly from the same model run as in figure (18a). The wind stress is parallel to the western boundary sloping at 45^0. Since $\tau_x \neq 0$ there are Kelvin waves present in addition to the Yanai waves. The 25-day waves appear again after about 150 days when the Kelvin wave peak and high frequency Yanai waves have passed. (b): The power spectrum of the time series in (a) taken from days 150 to 300 showing a high peak centred on 25 days.

completely. The very-high frequency waves, on the other hand, disappear rapidly out of the domain through the sponge layer due to the high group velocities. The relationship between group velocity and period is not a linear one and in fact in the narrow period band between 30 and 20 days the group velocity doubles in size, as we pointed out before, from 25 to 50 $cm\,s^{-1}$ (figure 9b). This large change in group velocity over such a narrow period range causes a preferential period selection in the interior of the domain, after a time period. To see this more clearly we present the energy spectrum of this time series between days 150 and 300 (figure 24b). The dominant peak is centred on 25 days. (The secondary peaks are due to inertia-gravity waves).

In the second case we examine the simulation with a sloping western boundary at 45°as in figure (17b). The wind stress, being parallel to the western boundary, has both a τ_x and a τ_y component and therefore there are Kelvin waves as well as the Yanai waves in the solution. We take the time series of the height field anomaly for 300 days at a point located the same distance from the western boundary as in the previous case and subtract out the mean value (figure 25a). The initial large peak is due to the Kelvin waves and thereafter the Yanai waves are apparent. The energy spectrum for this series for days 150 to 300 again shows a dominant peak centred on 25 days (figure 25b). This result verifies our previous findings that the slope of the boundary does not interfere with the preferential period selection.

5.5 Wavelet Analysis

Fourier analysis of a time series yields an average amplitude for each wave component over the entire series. This means that all local information is lost. Wavelet analysis can provide this local information and we now demonstrate how this can be used to illustrate further the particular frequency (or wavelength) selection in the dispersive Yanai wave packets we have discussed.

Meyers *et al.* (1992) [40] illustrated how wavelet analysis can be used to measure group velocities over a finite range of wavenumbers in an Yanai wave packet. Here we use the same wavelet transform as discussed in their study. For a given function $f(x)$ we define the wavelet transform as follows:

$$T_g(b,a) = \frac{1}{\sqrt{a}} \int g(\frac{x-b}{a}) f(x) dx \tag{123}$$

The function $g(x)$ is known as the "mother wavelet" and must satisfy specific properties (as detailed in Meyers (1992) *et al.* [40]). b is a translation parameter in the x dimension and a is a length scale. The transform is essentially a convolution of $f(x)$ with the set of functions obtained from the translations and dilations of the wavelet $g(x)$. It maps the one-dimensional function $f(x)$ into a two-dimensional function $T_g(a,b)$ which is a measure of the relative "energy" at scale a and position b. We use the Morlet wavelet defined as:

$$g(x) = e^{icx - x^2/2} \tag{124}$$

with the parameter $c = 5$. We can think of the parameter a as being a measure of the wavelength of the waves in the function $f(x)$ and in fact, for this particular mother wavelet, Meyers *et al.* (1992) [40] derived a relationship between a and the wavelength λ of a Fourier mode:

$$a = (\frac{c + \sqrt{2 + c^2}}{4\pi})\lambda \qquad (125)$$

We select the anti-symmetric component of the height field anomaly from the standard test experiment (figure 17b) for our analysis. The function $f(x)$ is chosen to be the discrete function consisting of an array of 1064 data points on a zonal "slice" stretching from the western to the eastern boundary at a position 177 km north of the equator. The data together with the corresponding wavelet transform from the model simulation after 20, 60, 100, 140, 160 and 200 days are shown in figures (26) – (28). The contour values can be considered to be a measure of the relative "energy" in a particular wave (characterized by its wavelength which decreases in the vertical direction of the contour box) at a particular location (characterized by distance from the western boundary which increases in the horizontal direction of the contour box). (The contour values themselves are not shown because they do not correspond to a known quantitative measure of the energy field). Note the appearance of a "tongue" at the top-left corner after 20 days. This is a region of relatively high-energy, and as the simulation continues it begins to reach towards the bottom-left corner of the contour box. Then after about 140 days this "tongue" begins to rise and narrow bending into a shape more centred on the wavelength at 945 km (which corresponds to a period of 25 days). After 200 days the selection of this particular wavelength by the "tongue" has become quite clear.

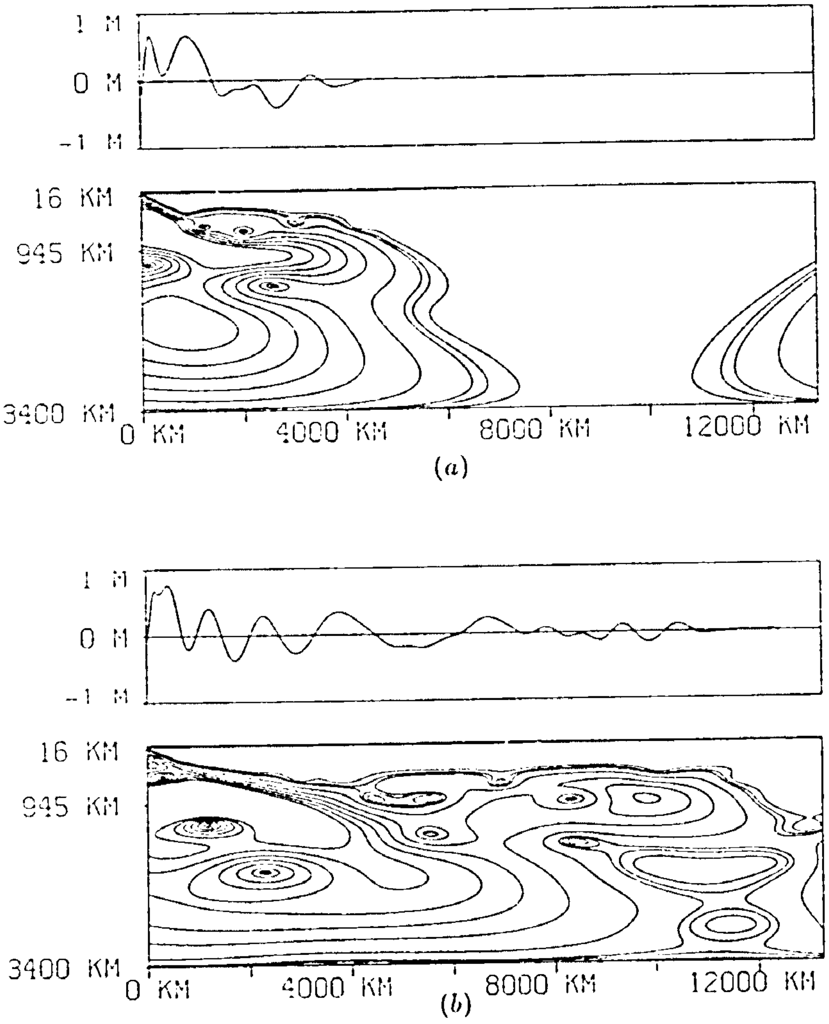

Figure 26: (a): *Top*: A west-east section of the anti-symmetric component of the height field anomaly (from the standard test experiment) at 177 *km* north of the equator after 20 days. (Values are in metres). *Bottom*: The wavelet transform of the profile above. Note the appearance of the "tongue" on the top-left corner of the plot, which corresponds to high contour values. (The contour values can be considered as an "energy" but are not labeled since they do not have a quantitative measure). (b): As in (a) after 60 days. Note the growth of the "tongue".

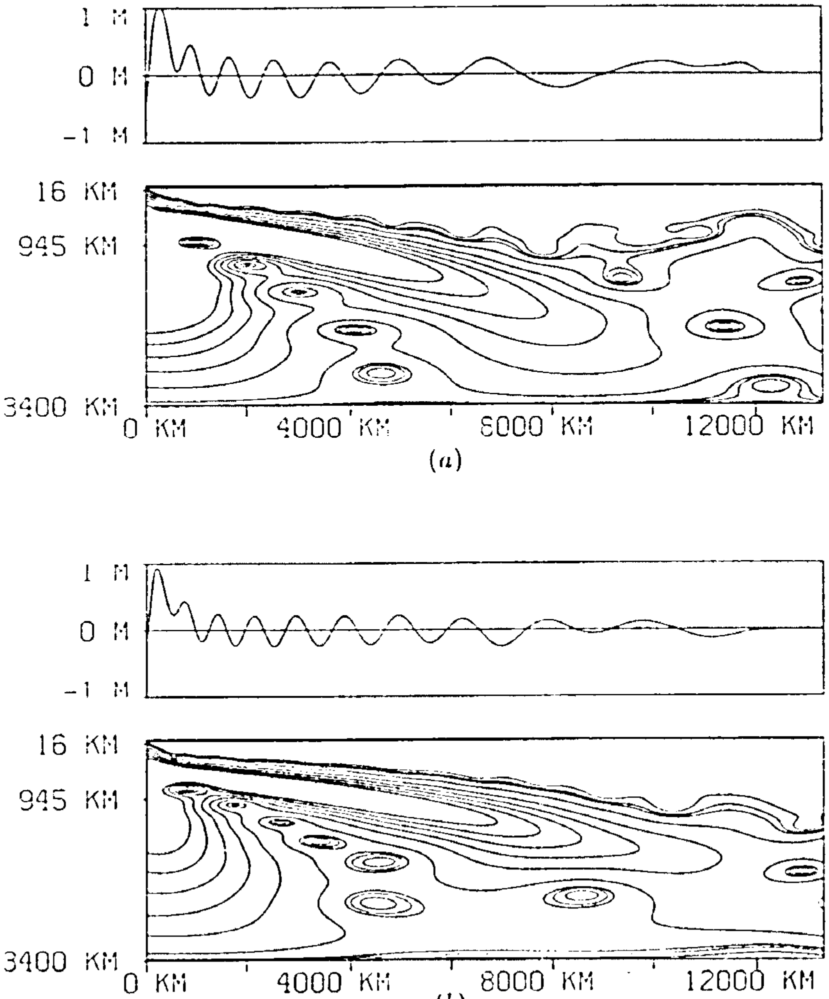

(*a*)

(*b*)

Figure 27: (a): The anti-symmetric height field and wavelet transform after 100 days. (b): As in (a) at time 140 days. The "tongue" is starting to narrow and rise after having extended almost to the bottom-left part of the domain. This is an indication of the waves beginning to select a narrow wavelength range.

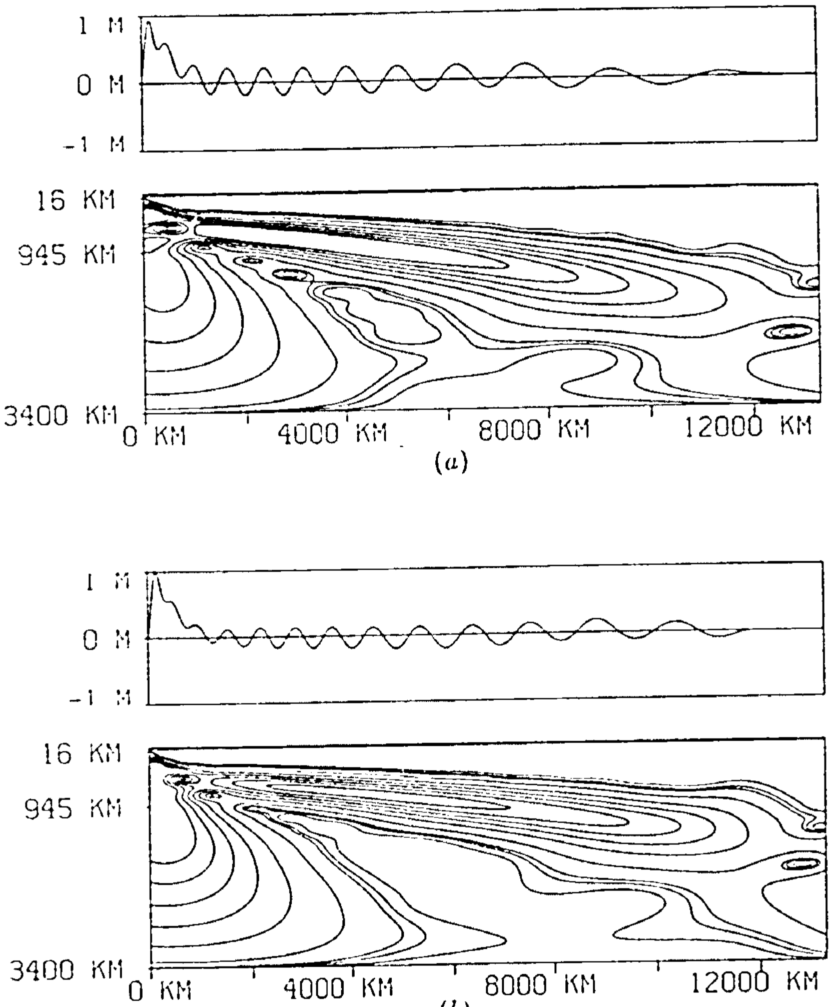

(*a*)

(*b*)

Figure 28: (a): The anti-symmetric height field and wavelet transform after 160 days. (b): As in (a) after 200 days. The "tongue" has continued to narrow and become more horizontal with a central wavelength around 945 *km*, which corresponds to a period of 25 days.

Chapter 6

Summary and Conclusions

The technological advances in computer architecture of recent years have inspired scientists to search for and develop new numerical techniques for solving partial differential equations. The fields of numerical weather prediction and oceanographic modelling have benefitted tremendously from these advances particularly with the advent of vector computers. Although finite difference methods are most popular amongst ocean modellers (mainly because of the ease in which complicated domains can be handled without coding difficulty) spectral models have also been constructed and are in use. We have designed and implemented a spectral Chebyshev-collocation ocean model using the 1-1/2 layer nonlinear reduced-gravity equations. The model employs an algebraic grid generating method to handle "moderately" complicated boundaries on simply connected domains. Extremely high-accuracy results can be obtained with a minimum number of Chebyshev modes due to the property of "spectral-accuracy" which the model possesses. A bi-characteristic scheme was applied to the boundaries which minimizes the boundary errors and maintains stable integrations.

The model is very useful for examining geophysical flows when the domains are not too complicated. It is feasible to extend it in order to handle more complex geometries (domains with islands and sharp inlets, etc.) by using multi-domain and more powerful mapping techniques. In this study we used the model to investigate certain dynamical properties of equatorial Yanai waves. These dispersive "instability" waves appear as anti-symmetric oscillations about the equator in the temperature (or pressure) field in the observations and are believed to play an important role in the momentum and heat balance in these regions. Although, theoretically at least, Yanai waves can have any value for the frequency, both the observations and the modelling results of previous works indicate that a preferential period of around 25 days is selected. This value may vary slightly between the oceans because of the different stratifications. To date, scientists have believed that the waves are caused by a latitudinal shear in the equatorial zonal mean currents (barotropic instability). We performed a series of experiments using simple cross-equatorial wind stress forcings in various configurations to show that the waves may also be generated without any shear in the mean flow. They may be generated either in interior regions or at the western boundary. If they originate from the western boundary then the geometry of this boundary may distort the initial packet of waves breaking the anti-symmetry in the height field but it does not interfere with the wavelengths selected nor with the value of the preferential wavelength of 945 km which becomes apparent in time. Nor is this particular wavelength dependent upon either the length scale of the forcing region or the Rossby deformation radius. In all of the experiments we performed, a packet of Yanai waves was generated with wavelengths ranging from about 15 km to 5000 km. The longest waves have the greatest group velocity and so they disappeared through the sponge layer on the eastern boundary most rapidly. The shortest waves have the smallest group velocity and they were damped in and near the forcing region. After a time period of about 150 days a narrow band of waves with central period of 25 days occupies the interior of the domain due to the nonlinear relationship between the group velocity and the period of the waves.

Although we do not refute the theory that equatorial instability waves are caused by a latitudinal shear in the mean zonal flow, we have presented a plausible explanation for the existence of these waves in regions where this shear is small (*e.g.* in the western Pacific) or where the shear is virtually non-existent at the generation times (*e.g.* in the Western Indian Ocean). Further observational investigations are necessary to elucidate this.

Bibliography

[1] A. Arakawa. Computational design for long-term numerical integrations of the equations of atmospheric motion. *J. Comp. Phys.*, 1:119 – 143, 1966.

[2] F. Baer and G. W. Platzman. A procedure for numerical integration of the spectral vorticity equation. *J. Meteorol.*, 18:393 – 410, 1961.

[3] J. P. Boyd. *Chebyshev & Fourier Spectral Methods.* Lecture notes in engineering. Springer-Verlag, 1989. 800 pp.

[4] F. P. Bretherton and M. J. Karweit. Mid-ocean mesoscale modelling. In *Numerical models of ocean circulation*, pages 237 – 249, NAS, Washington, D.C., 1975. Ocean Affairs Board, Nat. Res. Counc.

[5] D. Broutman and R. Grimshaw. Spectral multigrid and collocation methods for barotropic non-divergent flow over irregular coastal topography. *Geophys. Astrophys Fluid Dyn.*, 52:1 – 23, 1990.

[6] A. Busalacchi and J. Picaut. Seasonal variability from a model of the Tropical Atlantic Ocean. *J. Phys. Oceanogr.*, 13:1,564 – 1,588, 1983.

[7] C. Canuto, M. Y. Hussaini, A. Quarteroni, and T. Zang. *Spectral methods in fluid dynamics.* Springer-Verlag, 1988. 557 pp.

[8] C. Canuto and A. Quarteroni. On the boundary treatment in spectral methods for hyperbolic systems. *J. Comput. Phys.*, 71:100 - 110, 1987.

[9] S. M. Chiswell and R. Lukas. Rossby-gravity waves in the central equatorial Pacific Ocean during the NORPAX Hawaii-to-Tahiti shuttle experiment. *J. Geophys. Res.*, 94(c2):2091 - 2098, 1989.

[10] T. W. Cooley and J. W. Tukey. An algorithm for the machine calculation of complex Fouries series. *Math. Comp.*, 19:297 - 301, 1965.

[11] M. D. Cox. Generation and propagation of 30-day waves in a numerical model of the pacific. *J. Phys. Oceanogr.*, 10:217 - 248, 1980.

[12] W. Duing, P. Hisard, E. Katz, J. Knauss, J. Meincke, L. Miller, K. Moroshkin, G. Philander, A. Rybnikov, K. Voigt, and R. Weisberg. Meanders and long waves in the equatorial Atlantic. *Nature*, 257:280 - 284, 1975.

[13] E. Eliasen, B. Machenhauer, and E. Rasmussen. On a numerical method for integration of the hydrodynamical equations with a spectral representation of the horizontal fields. Technical Report Rept. No. 2, Institute for Teoretisk Meteorologi, Kobenhavns Universitet, Denmark, 1970. 35 pp.

[14] S. R. Fulton and W. H. Schubert. Chebyshev spectral methods for limited-area models. part 1: Model problem analysis. *Mon. Wea. Rev.*, 115:1940 - 1953, 1987a.

[15] S. R. Fulton and W. H. Schubert. Chebyshev spectral methods for limited-area models. part 2: Shallow water model. *Mon. Wea. Rev.*, 115:1954 – 1965, 1987b.

[16] D. Gottlieb, M. Gunzburger, and E. Turkel. On numerical boundary treatment of hyperbolic systems for finite difference and finite element methods. *SIAM J. Numer. Anal.*, 19:671 – 682, 1982.

[17] D. Gottlieb and S. Z. Orszag. *Numerical analysis of spectral methods: Theory and Applications.* Regional conference series in applied mathematics. SIAM, Philadelphia, Pennsylvania 19103, 1977. 170 pp.

[18] D. Gottlieb and E. Tadmor. The CFL condition for spectral approximations to hyperbolic initial-boundary value problems. *Math. Comp.*, 56:565 – 588, 1991.

[19] A. Grammeltvedt. A survey of finite-difference schemes for the primative equations for a barotropic fluid. *Mon. Wea. Rev.*, 97(5):384 – 404, 1969.

[20] D. Haidvogel and P. B. Rhines. Waves and circulation driven by oscillatory winds in an idealized ocean basin. *Geophys. Astrophys. Fluid Dyn.*, 25:1 – 63, 1983.

[21] D. B. Haidvogel. Periodic and regional models. In A. R. Robinson, editor, *Eddies in marine science*, pages 404 – 437. Springer-Verlag, 1983.

[22] D. B. Haidvogel and I. M. Held. Homogeneous quasi-geostrophic turbulence driven by a uniform temperature gradient. *J. Atmos. Sci.*, 37:2644 – 2660, 1980.

[23] D. B. Haidvogel, A. R. Robinson, and E. E. Schulman. The accuracy, efficiency, and stability of three numerical models with application to open ocean problems. *J. Comput. Phys.*, 34:1 – 53, 1980.

[24] D. B. Haidvogel, J. L. Wilkin, and R. Young. A semi-spectral primative equation ocean circulation model using vertical sigma and orthogonal curvilinear horizontal coordinates. *J. Comp. Phys.*, 94:151 – 185, 1991.

[25] D. V. Hansen and C. A. Paul. Genesis and effects of long waves in the equatorial Pacific. *J. Geophys. Res.*, 89(c6):10,431 – 10,440, 1984.

[26] R. R. Harvey and W. C. Patzert. Deep current measurements suggest long waves in the eastern equatorial Pacific. *Science*, 193:883 – 884, 1976.

[27] S. Hellerman and M. Rosenstein. Normal monthly wind stress over the world ocean with error estimates. *J. Phys. Oceanogr.*, 13:1093 – 1104, 1983.

[28] T. G. Jensen. Modeling the seasonal undercurrents in the Somali Current System. *J. Geophys. Res.*, 93(c12):15,437 – 15,453, 1991.

[29] T. G. Jensen and D. A. Kopriva. Comparison of a finite difference and a spectral collocation reduced gravity ocean model. Technical Report FSU-SCRI-88-65, Supercomputer Computations Research Institute, Florida State University, Tallahassee, Fl., 1988.

[30] M. A. Johnson and J. J. O'Brien. Modelling the Pacific Ocean. *Intl J. Supercomp. App.*, 4(2):37 – 47, 1990a.

[31] M. A. Johnson and J. J. O'Brien. The role of coastal Kelvin waves on the Northeast Pacific Ocean. *J. Mar. Sys.*, 1:29 - 38, 1990b.

[32] J. Kindle and D. Thompson. The 26- and 50- day oscillations in the Western Indian Ocean: Model results. *J. Geophys. Res.*, 94(c4):4,721 - 4,736, 1989.

[33] D. A. Kopriva. Computation of hyperbolic equations on complicated domains with patched and overset Chebyshev grids. *SIAM J. Sci. Stat. Comput.*, 10(1):120 - 132, 1989.

[34] R. W. Lardner, H. M. Cekirge, and N. Gunway. Numerical solution of the two-dimensional tidal equations using the method of characteristics. *Comp. & Maths. with Appls.*, 12A(10):1015 - 1080, 1986.

[35] R. Legeckis. Long waves in the eastern equatorial Pacific Ocean: A view from a geostationary satellite. *Science*, 197:1179 - 1181, 1977.

[36] M. E. Luther and J. J. O'Brien. A model of the seasonal circulation in the Arabian Sea forced by observed winds. *Prog. Oceanogr.*, 14:353 - 385, 1985.

[37] J. R. Luyten and D. H. Roemmich. Equatorial currents at semi-annual period in the Indian Ocean. *J. Phys. Oceanogr.*, 12:406 - 413, 1982.

[38] T Matsuno. Quasi-geostrophic motions in the equatorial area. *J. Meteor. Soc. Japan*, 44(1):25 - 42, 1966.

[39] M. J. McPhaden, S. P. Hayes, L. J. Mangum, and J. M. Toole. Variability in the western equatorial Pacific Ocean during the 1986 – 1987 El Nino/Southern Oscillation event. *J. Phys. Oceanogr.*, 20:190 – 208, 1990.

[40] S. D. Meyers, B. G. Kelly, and J. J. O'Brien. The dispersion of Yanai waves examined by wavelet analysis. To be submitted to J. Phys. Oceanogr., 1992.

[41] D. W. Moore and J. P. McCreary. Excitation of intermediate-frequency equatorial waves at a western ocean boundary: With application to the Indian Ocean. *J. Geophys. Res.*, 95(c4):5219 – 5231, 1990.

[42] D. W. Moore and S. G. H. Philander. Modeling of the tropical oceanic circulation. In E. D. Goldberg, I. N. McCave, J. J. O'Brien, and J. H. Steele, editors, *The Sea, volume 6*, chapter 8, pages 319 – 361. Wiley-Interscience, 1977.

[43] J. J. O'Brien, D. Adamec, and D. W. Moore. A simple model of upwelling in the Gulf of Guinea. *Geophys. Res. Lett.*, 5(9):641 – 644, 1978.

[44] S. A. Orszag. Transform method for the calculation of vector-coupled sums: Application to the spectral form of the vorticity equation. *J. Atmos. Sci.*, pages 890 – 895, 1970.

[45] A. Pares-Sierra and J. J. O'Brien. The seasonal and interannual variability of the California Current system: A numerical model. *J. Geophys. Res.*, 94(c3):3,159 – 3,180, 1989.

[46] C. Perigaud. Sea level oscillations observed with Geosat along the two shear fronts of the Pacific north equatorial countercurrent. *J. Geophys. Res.*, 95:7239 – 7248, 1990.

[47] S. G. H. Philander. Instabilities of zonal equatorial currents. *J. Geophys. Res.*, 81(21):3725 – 3735, 1976.

[48] S. G. H. Philander. Instabilities of zonal equatorial currents, 2. *J. Geophys. Res.*, 83(c7):3679 – 3682, 1978.

[49] S. G. H. Philander, W. J. Hurlin, and R. C. Pacanowski. Properties of long equatorial waves in models of the seasonal cycle in the tropical Atlantic and Pacific oceans. *J. Geophys. Res.*, 91(c12):14,207 – 14211, 1986.

[50] G. W. Platzman. The spectral form of the vorticity equation. *J. Meteor.*, 17:635 – 644, 1960.

[51] G. Reverdin and J. Luyten. Near-surface meanders in the equatorial Indian Ocean. *J. Phys. Oceanogr.*, 16:1088 – 1100, 1986.

[52] P. B. Rhines. Waves and turbulence on a β-plane. *J. Fluid Mech.*, 69:417 – 443, 1975.

[53] I. Silberman. Planetary waves in the atmosphere. *J. Meteor.*, 11:27 – 34, 1954.

[54] R. C. Simmons, M. E. Luther, J. J. O'Brien, and D. M. Legler. Verification of a numerical ocean model of the Arabian Sea. *J. Geophys. Res.*, 93(c12):15,437 – 15,453, 1988.

[55] A. Solomonoff and E. Turkel. Global properties of pseudospectral methods. *J. Comput. Phys.*, 81:239 – 276, 1989.

[56] I. Stakgold. *Geeen's functions and boundary value problems.* Wiley-Interscience, 1979. 638 pp.

[57] J. F. Thompson, Z. U. A. Warsi, and C. W. Mastin. *Numerical Grid Generation: Foundations and Applications.* North-Holland, New York, 1985. 438 pp.

[58] P. T. H. Tsai. The 26-day oscillation observed in the satellite SST measurements in the equatorial western Indian Ocean. Master's thesis, Florida State University, Tallahassee, Florida, 32306, 1990.

[59] R. H. Weisberg. Equatorial waves during GATE and their relation to the mean zonal circulation. *Deep-Sea Res.*, 26(Suppl. II):179 – 198, 1979.

[60] R. H. Weisberg and A. M. Horigan. Low frequency variability in the equatorial Atlantic. *J. Phys. Oceanogr.*, 11:913 – 920, 1981.

[61] R. H. Weisberg, A. M. Horigan, and C. Colin. Equatorially trapped Rossby-gravity wave propagation in the Gulf of Guinea. *J. Mar. Res.*, 37:67 – 86, 1979.

[62] R. H. Weisberg, L. Miller, A. Horigan, and J. A. Knauss. Velocity observations in the equatorial thermocline during GATE. *Deep-Sea Res.*, 26(Suppl. II):217 – 248, 1979.

[63] R. H. Weisberg and T. J. Weingartner. Instability waves in the equatorial Atlantic Ocean. *J. Phys. Oceanogr.*, 18:1641 – 1657, 1988.

[64] K. E. Woodberry, M. E. Luther, and J. J. O'Brien. The wind-driven seasonal circulation in the Southern Tropical Indian Ocean. *J. Geophys. Res.*, 94(c12):17,985 – 18,002, 1989.

Vita

Name:	Brian Gerard Joseph Kelly
Date of Birth:	5th of September, 1958
Place of Birth:	Limerick city, Ireland
Education:	B.Sc. in Mathematical Science, Autumn of 1979, University College, Cork, Ireland M.Sc in Applied Mathematics and Computer Science, Autumn of 1981, University College Cork, Ireland Ph.D. in Geophysical Fluid Dynamics, Fall semester 1992, Florida State University
Title of Dissertation:	On the generation and dispersion of Yanai waves with a spectral Chebyshev-collocation reduced-gravity ocean model
Major Professor:	Dr. James J. O'Brien
Previous Work Experience:	Teacher at the Regional Technical College, Cork, Ireland (1981 - 1982) and at the National Institute for Higher Education, Limerick, Ireland (1982 - 1986)